NOAA Technical Report ERL 264-WMPO 1

U.S. DEPARTMENT OF COMMERCE
NATIONAL OCEANIC AND ATMOSPHERIC ADMINISTRATION
Environmental Research Laboratories

Analysis of STORMFURY Data Using the Variational Optimization Approach

ROBERT C. SHEETS

BOULDER, COLO.
APRIL 1973

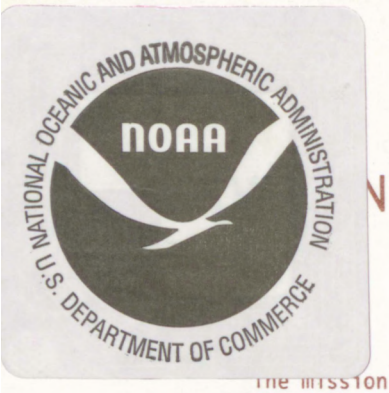

NMENTAL RESEARCH LABORATORIES

The mission of the Environmental Research Laboratories is to study the oceans, inland waters, the lower and upper atmosphere, the space environment, and the earth, in search of the understanding needed to provide more useful services in improving man's prospects for survival as influenced by the physical environment. Laboratories contributing to these studies are:

Earth Sciences Laboratories (ESL): Seismology, geomagnetism, geodesy, and related earth sciences; earthquake processes, internal structure and shape of the earth and distribution of the earth's mass.

Atlantic Oceanographic and Meteorological Laboratories (AOML): Geology and geophysics of ocean basins, oceanic processes, and sea-air interactions (Miami, Florida).

Pacific Oceanographic Laboratories (POL): Oceanography with emphasis on the oceanic processes and dynamics; tsunami generation, propagation, modification, detection, and monitoring (Seattle, Washington).

Atmospheric Physics and Chemistry Laboratory (APCL): Processes of cloud and precipitation physics; chemical composition and nucleating substances in the lower atmosphere; and laboratory and field experiments toward developing feasible methods of weather modification.

Air Resources Laboratories (ARL): Diffusion, transport, and dissipation of atmospheric contaminants; development of methods for prediction and control of atmospheric pollution; geophysical monitoring for climatic change (Silver Spring, Maryland).

Geophysical Fluid Dynamics Laboratory (GFDL): Dynamics and physics of geophysical fluid systems; development of a theoretical basis, through mathematical modeling and computer simulation, for the behavior and properties of the atmosphere and the oceans (Princeton, New Jersey).

National Severe Storms Laboratory (NSSL): Tornadoes, squall lines, thunderstorms, and other severe local convective phenomena directed toward improved methods of prediction and detection (Norman, Oklahoma).

Space Environment Laboratory (SEL): Solar-terrestrial physics, service and technique development in the areas of environmental monitoring and forecasting.

Aeronomy Laboratory (AL): Theoretical, laboratory, rocket, and satellite studies of the physical and chemical processes controlling the ionosphere and exosphere of the earth and other planets, and of the dynamics of their interactions with high altitude meteorology.

Wave Propagation Laboratory (WPL): Development of new methods for remote sensing of the geophysical environment with special emphasis on optical, microwave and acoustic sensing systems.

Weather Modification Program Office (WMPO): Plans and directs ERL weather modification activities, operates ERL aircraft fleet, and research on cumulus cloud modification, on hurricanes and other tropical problems, and on hurricane modification.

NATIONAL OCEANIC AND ATMOSPHERIC ADMINISTRATION

BOULDER, COLORADO 80302

U.S. DEPARTMENT OF COMMERCE
Frederick B. Dent, Secretary

NATIONAL OCEANIC AND ATMOSPHERIC ADMINISTRATION
Robert M. White, Administrator
ENVIRONMENTAL RESEARCH LABORATORIES
Wilmot N. Hess, Director

NOAA TECHNICAL REPORT ERL 264-WMPO 1

Analysis of STORMFURY Data Using the Variational Optimization Approach

ROBERT C. SHEETS

BOULDER, COLO.
APRIL 1973

For sale by the Superintendent of Documents, U. S. Government Printing Office, Washington, D. C. 20402

TABLE OF CONTENTS

TABLE OF CONTENTS (CONTINUED)

LIST OF ILLUSTRATIONS

LIST OF TABLES

ANALYSIS OF STORMFURY DATA USING THE VARIATIONAL OPTIMIZATION APPROACH

Robert C. Sheets

The variational optimization technique is used to develop a scheme to analyze the high energy portion of a hurricane. The derived analysis equations are used to filter the data in an attempt to obtain the signal for selected scales of motion. The particular filters were designed from empirical evidence. These filters are also used to develop variability factors for the standard meteorological parameters and selected scales of motion. A second set of analysis equations is derived which includes the first set as well as the gradient wind condition.

These analysis schemes are applied to data collected in Hurricane Debbie (1969) during two artificial modification attempts. The results of these analyses are then used to define a more explicit seeding hypothesis which can explain and evaluate future seeding experiments.

The validity of the technique is based on empirical evidence, since statistical evaluation is quite difficult to obtain. Although strong physical inferences can be drawn from this analysis, more such data analyses are required before strong statistical support can be claimed.

1. INTRODUCTION

Two basic questions must be answered in any attempt to determine possible effects of artificial modification attempts on hurricanes. What changes in structure or intensity actually occurred? What, if any, portion of these changes result from the modification experiments? The approach reported in this paper attempts to provide answers for the first question and presents strong evidence for answering the second.

There are many questions concerning general or climatic conditions that must also be considered before looking at details for particular case studies. For instance, what is the likelihood that a hurricane goes through a natural diurnal variation? The seeding cases studied for this paper were continuously monitored for nearly 24-hours, and the actual seeding occurred over a 10-hour period. Therefore, any natural diurnal variation must be considered in the analysis. Many other factors must also be considered; such as, are changes in intensity of the hurricanes related to the location of the storm? Is there any correlation between the size of the hurricane eye and its present or future natural changes in intensity? Do stronger or weaker storms or intensifying or decaying

storms exhibit characteristic fluctuations? There are many more similar questions that could be asked, and the author has attempted to answer many of them in previous papers (Sheets, 1969a, b, 1970, 1972a, b).

Theoretically, it would appear to be a simple matter to determine what changes occur. However, in practice, this becomes a very difficult problem. For the past few years, highly instrumented aircraft have been collecting invaluable information within the high energy portion of hurricanes. Many problems associated with the processing of this data have been encountered and solved. However, some significant sources of error continue to plague the researcher when analyzing these data. One such source is in positioning the data with respect to some fixed reference point, such as the center of the moving storm. This center is usually taken as the geometric center of the eye of the storm as determined by radar. Often the radar eye is not circular and sometimes is discontinuous. Even more detrimental is that continuous displays of the radar center are not always available. In addition, the Doppler radar system is affected by the moving surface water and heavy precipitation; these factors can further contribute to positioning errors. Other parameters also contain significant sources of errors, and the result is that considerable effort is needed to process these data. Much skill and knowledge in the art of processing these data have been attained over recent years and are directed at minimizing these errors. However, significant errors still remain.

Several case studies of the high energy portion of hurricanes show they have a variety of types, sizes, and strengths. For instance, Hurricanes Dora (1964) (Sheets, 1968) and Helene (1958) (Colon, 1964) were relatively strong storms that covered a large area; whereas, Hurricane Daisy (1958) (Colon, 1961) was a small, intense storm during the investigation. Hurricanes Hilda (1964) (Hawkins and Rubsam, 1968) and Cleo (1958) (LaSeur and Hawkins, 1963) were somewhere between these two extremes in size and structure, but Janice (1958) and Ella (1962) (Sheets, 1967a, b) were generally less organized than any of the above storms. However, all these storms had many common features.

Quite pertinent to this study is the presence of small areas of extremum (maximum and minimum) values of the various parameters, such as wind speed, temperature, and moisture. Often, these maximum centers are associated with major rainbands or strong cells within the rainbands. These features apparently circulate, propagate, or form and dissipate around the storm center and are quite prominent in the middle and lower troposphere. This natural condition results in large fluctuations of a given variable such as wind speed in both space and time. For instance, it is not unusual for wind speed changes of as much as 30 percent or more to occur within a few minutes at a position fixed with respect to the storm center. Fluctuations of this same magnitude are observed over short horizontal distances in space. Both of these features are readily apparent in

analyses of Hurricane Dora for September 7 and 8, 1964 (Sheets, 1968). These fluctuations can easily mask changes in the mesoscale intensity or structure of the storm.

A major portion of the large fluctuations apparently is contained in a few selected scales of motion. If this is true, then it seems necessary to determine what these scales are, their contributions to the total change, their conservativeness from hour to hour, day to day, and storm to storm. Also, it would be desirable to determine whether or not these features are affected by specified types of artificial modification attempts. To accomplish this task, some filtering techniques must be devised to effectively separate the contributions from the desired scales of motion. An indication of the probable success of this approach was attained in an earlier study (Sheets, unpublished report), which showed that simple filtering techniques considerably decrease the magnitude of the changes. For instance, some short space and time averages of the maximum wind speed bands reduced the fluctuation of the maximum wind speed to less than one-third of its original value in the four or five storms studied and the results still appeared sensitive to major changes.

Standard filtering techniques seem to be somewhat difficult to apply due to the overwhelming percentage of the variance being contained in the longer wavelength features. Data records of unequal length, large variations in end-point values, and mispositioned data present other significant problems. The removal of some mean profile would permit study of the smaller scale features in more detail. However, the construction of this profile is quite arbitrary, and mispositioned data, particularly in the eyewall region, could cause very large misleading values. Many of the more refined techniques become quite complicated and, even more damaging, require a considerable number of fixed end-point values. The variational optimization approach offers a method of obtaining nearly the same information with much less difficulty as well as providing a systematic method for filling in missing data.

A major portion of this study develops and applies the variational optimization technique to the data collected in Hurricane Debbie on August 18 and 20, 1969. Another portion of this study uses the variational optimization approach to determine the degree of the validity of the gradient wind model. These techniques are discussed in section 2.

The filtered data are stratified according to the scale of motion, and the variability of the various parameters within each scale is determined. We also attempt to determine if an organized sequence of changes exists, say from small scales to larger scales; hopefully this will lead to a more explicit seeding hypothesis. Particular emphasis is placed on determining a set of events that may occur with the seeded case and not with the nonseeded case. This approach seems necessary since it is improbable that enough seeded cases will be available in the near future for applying standard statistical tests. The desired result would be that the probability would be quite low that this set of events would occur naturally.

2. HURRICANE DEBBIE (1969) SEEDING EXPERIMENTS AND RELEVANT HYPOTHESES

Rosenthal (1971) has provided an excellent historical review and interpretation of the development and evolution of hurricane eyewall seeding hypotheses. Selected excerpts of the report are repeated below, but the reader should refer to sections 4 and 5 of that report to obtain a more complete understanding of the "seeding hypothesis evolution."

Many studies have shown that the hurricane eyewall cloud is generally located in the region of maximum low-level pressure gradient. Early investigators believed that these wall clouds contained significant quantities of supercooled water. This belief was substantiated by observations from flights at altitudes above the freezing level and was verified in recent investigations (Sheets, 1969b). These facts led Simpson and Malkus (1964) to propose an eyewall seeding hypothesis (called here Hypothesis I) and quoted from Rosenthal (1971) as follows:

> *"If this supercooled water were frozen through nucleation by silver iodide crystals, the released heat of fusion would produce temperature increases; and therefore, hydrostatically, pressure decreases near the region of the strongest pressure gradient. If the central pressure did not concomitantly decrease, a reduction in maximum pressure gradient, and in turn, a reduction in wind speed should be the net result."*

The increase in heat caused by the direct released heat of fusion is actually a relatively small part of the total process (~80 cal/gm). The major contributor, which results from the freezing of the supercooled water, is, of course, the enhancement of the natural processes of ice crystal growth and splintering. These processes provide many more freezing nuclei; this process results in a rapid multiplication of the *rate* of release of latent heat of sublimation and fusion (~680 cal/gm).

Rosenthal (1971) then offered several arguments indicating a necessary modification of the hypothesis and implied experiments to attain the desired results. The most significant of these arguments is "...the fact that the eyewall drives the storm's transverse circulation, and seeding this region alone would very likely accelerate this circulation, thus providing a more rapid inflow of both angular momentum and water vapor to the eyewall region."

Rosenthal performed several simulated seeding experiments with his numerical hurricane model. The results of these experiments and the physical arguments against Hypothesis I led him and others associated with Project STORMFURY to propose a different hypothesis as follows (Rosenthal, 1971):

"Hypothesis II differs from Hypothesis I in that the latter calls for seeding the eyewall alone whereas the former suggests seeding either from the eyewall outward or entirely outward from the eyewall. While the logistics of these hypotheses differ only slightly, the physical arguments are substantially different. In Hypothesis II, the basic idea is to stimulate convection and ascent at radii greater than that of the eyewall. The region of stimulated convection is intended to compete with the eyewall for the inflowing air at low levels. If significant portions of the inflow can be diverted upward at the seeded radii, the angular momentum and water vapor supplies to the original eyewall and wind maximum will be reduced. As a consequence, one would expect the original wind maximum to be reduced and the eyewall convection to be diminished."

Calculations by Sheets (1969c) indicated that it is difficult to get much more vertical growth of the hurricane eyewall cloud by seeding. This results from the very stable condition caused by the release of latent heat at the upper levels. However, outward from the eyewall, the potential for increased cloud growth extending above the freezing level and containing supercooled water increases markedly. This fact, along with the knowledge of the presence of the required supercooled water in the clouds outside the eyewall (Sheets, 1969b), offers further evidence supporting Hypothesis II.

The Hurricane Debbie experiments on August 18 and 20, 1969, were performed as suggested by Hypothesis II. These experiments are described in considerable detail by Gentry (1970). Only that portion directly related to this paper is discussed here. Figure 1 shows the track and geographical locations of the storm during the two experiments. Figure 2 shows the pattern of the seeding track. Five seeding runs were made at approximately 2-hour intervals during each of the two seeding experiments. Figure 3 shows the monitoring flight tracks of the NOAA Research Flight Facility's DC-6 aircraft, and figure 4 shows the monitoring patterns for the various levels. The analyses in this paper are based on the data obtained during these missions.

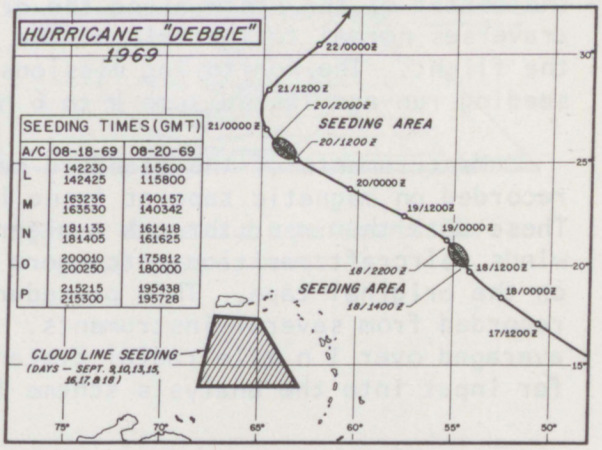

Figure 1. Hurricane Debbie (1969) storm track and modification experiments.

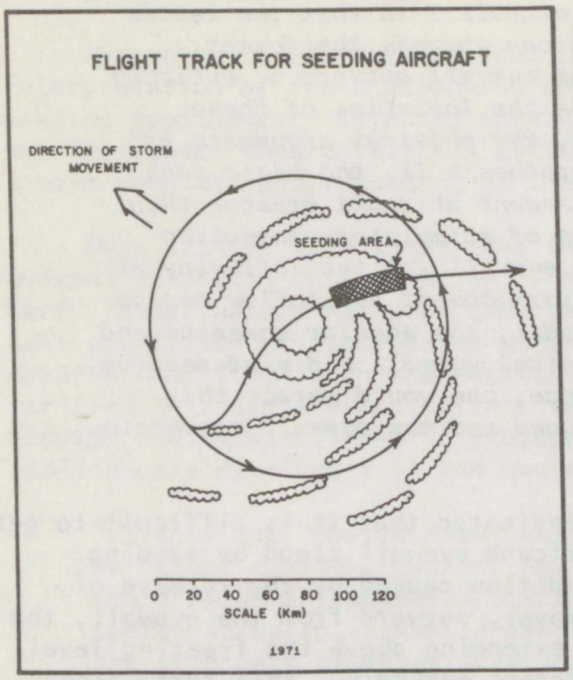

Figure 2. Seeding area and flight pattern.

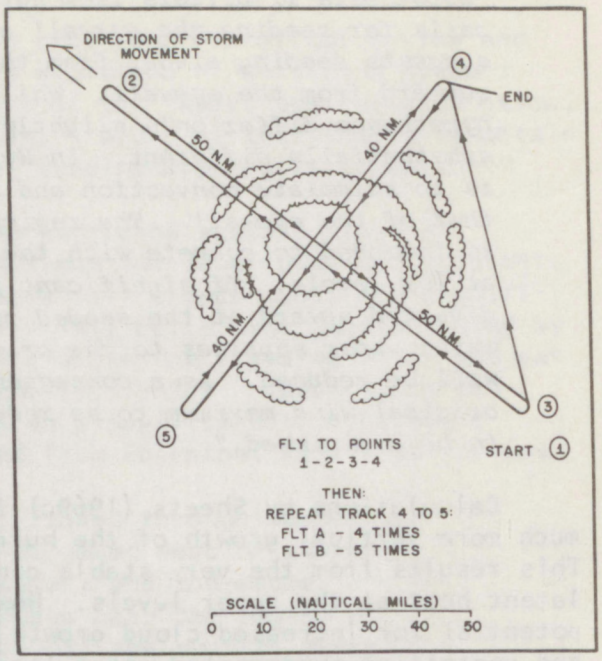

Figure 3. Flight pattern for monitoring missions.

There were three monitoring flights at 12,000 ft on each of the 2 seeding days. The pattern basically consisted of two traverses through the center of the storm along the direction of motion and then repetitive traverses normal to the axis of the storm movement for the remainder of the flight. The monitoring missions began some 2 hours before the first seeding run and lasted some 4 to 6 hours after the final seeding.

Measurements of the standard meteorological parameters were digitally recorded on magnetic tape at 1-sec intervals (Friedman et al., 1969a, b). These data then went through a rigorous processing procedure where the winds, aircraft position, etc. were recomputed from the raw data recorded on the original tape. This procedure included calibration of the signals recorded from several instruments. These processed data were then averaged over 1 n mile radial distance intervals from the storm center for input into the analysis scheme (see section 3).

3. DEVELOPMENT OF THE ANALYSIS EQUATIONS AND VARIABILITY FACTORS

The variational optimization technique (Sasaki, 1958, 1968, 1970a, b) was used to filter the data and develop a more explicit seeding hypothesis. The method is based on a functional that defines selected optimization constraints. Two different functionals were used in this study. The

first, J_1, consists of two low-pass filters with an "observational constraint." The second, J_2, contains the "gradient wind constraint" in addition to J_1.

The first functional is defined as follows:

$$J_1 = \int_r \{\beta(\frac{\partial^2\theta}{\partial r^2})^2 + \gamma(\frac{\partial\theta}{\partial r})^2 + \alpha(\theta - \tilde{\theta})^2\}dr, \qquad (1)$$

where θ is any variable, $\tilde{\theta}$ is the observed value of θ, and r is radial distance from the hurricane center. The first two terms act as low-pass filters, and the last term is similar to a "least-square fitting" of the derived field to the observations (Wagner, 1971). In the remainder of this paper, these three terms are referred to as the curvature, gradient, and observational constraints, respectively. The quantities α, γ, and β are the weights placed on their respective terms and, as shown later, determine the degree of filtering imposed on the analyses.

The nondimensional finite difference analog for (1) as derived in appendix A (symbols are defined in appendix A) become

$$J_1 = \sum_r \{\beta(\nabla_r{}^2\theta)^2 + \gamma(\nabla_r\theta)^2 + \alpha(\theta - \tilde{\theta})^2\}\Delta r. \qquad (2)$$

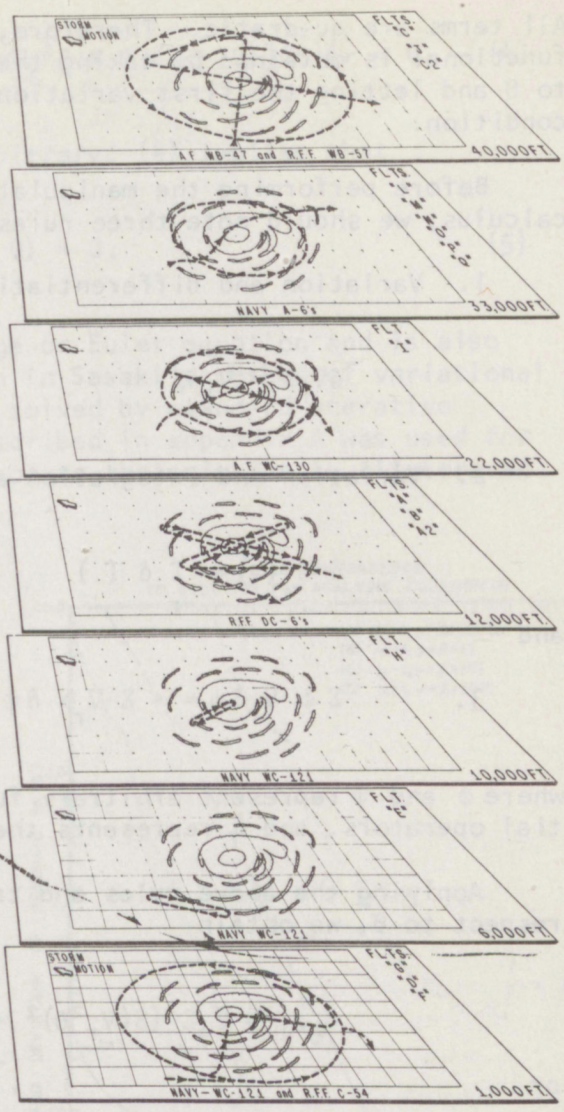

Figure 4. Flight patterns for eyewall experiment.

All terms are quadratic. Therefore, the minimum of the value of the functional is obtained by taking the first variation of (2) with respect to θ and letting the first variation vanish under the proper boundary condition.

Before performing the manipulations associated with variational calculus, we should note three rules:

1. Variation and differentiation are permutable processes; thus,

$$\delta \nabla_r \phi = \nabla_r \delta \phi .$$

2. Variation and integration are permutable processes; thus,

$$\delta \sum_r ( ) = \sum_r \delta ( )$$

and

3. $$\sum \phi \ \nabla_r \delta \psi = - \sum \nabla_r \phi \ \delta \psi$$

where ϕ and ψ represent arbitrary functions that can include differential operators, and δ represents the variational operator.

Applying the above rules and taking the first variation of (2) with respect to θ, we obtain

$$\delta_\theta J_1 = \delta_\theta \sum_r \{\beta(\nabla_r{}^2\theta)^2 + \gamma(\nabla_r\theta)^2 + \alpha(\theta - \tilde{\theta})^2\} \Delta r = 0$$

or

$$\delta_\theta J_1 = \sum_r \{2\beta(\nabla_r{}^2\theta)(\nabla_r{}^2(\delta\theta)) + 2\gamma(\nabla_r\theta)(\nabla_r(\delta\theta)) + 2\alpha(\theta - \tilde{\theta})\delta\theta\} \Delta r = 0. \qquad (3)$$

We now use summation by parts and assume natural boundary conditions (Sasaki, 1969). Therefore, (3) becomes

$$\delta_\theta J_1 = \sum_r \{2\beta\nabla_r{}^2\theta)\delta\theta - 2\gamma\nabla_r(\nabla_r\theta)\delta\theta + 2\alpha(\theta - \tilde{\theta})\delta\theta\} \Delta r = 0,$$

or

$$\delta_\theta J_1 = \sum_r \{[2\beta\nabla_r{}^4\theta - 2\gamma\nabla_r{}^2\theta + 2\alpha(\theta - \tilde{\theta})]\delta\theta\}\Delta r = 0. \quad (4)$$

Since the variation, $\delta\theta$, is arbitrary, (4) implies that

$$\beta\nabla_r{}^4\theta - \gamma\nabla_r{}^2\theta + \alpha(\theta - \tilde{\theta}) = 0, \quad (5)$$

which is the classical Euler-Lagrange or Euler equation and is also referred to as the analysis equation in Sasaki's method of variational analysis. This equation is readily solved by standard iterative techniques. The Liebmann method described in appendix A was used for this paper and the rate of convergence to the solution is illustrated in figure 5.

3.1 Response Function

The response function for the finite difference analog of the analysis equation (5) is derived in order to determine the desired values for the weights α, γ, and β. The components of the "true" ($\tilde{\theta}_n$) and analyzed (θ_n) fields, are assumed to be represented by

$$\begin{aligned}
\tilde{\theta}_n &= Ae^{ikn\Delta r} \text{ and } \theta_n = Be^{ikn\Delta r}, \\
\theta_{n+1} &= Be^{ik(n+1)\Delta r} = Be^{ikn\Delta r}e^{ik\Delta r}, \\
\theta_{n+2} &= Be^{ikn\Delta r}e^{2ikn\Delta r}, \\
\theta_{n-1} &= Be^{ikn\Delta r}e^{-ik\Delta r}, \\
\theta_{n-2} &= Be^{ikn\Delta r}e^{-2ik\Delta r}, \\
d &= \Delta r \text{ and } r = n\Delta r,
\end{aligned} \quad (6)$$

where k is the wave number and A and B are constants.

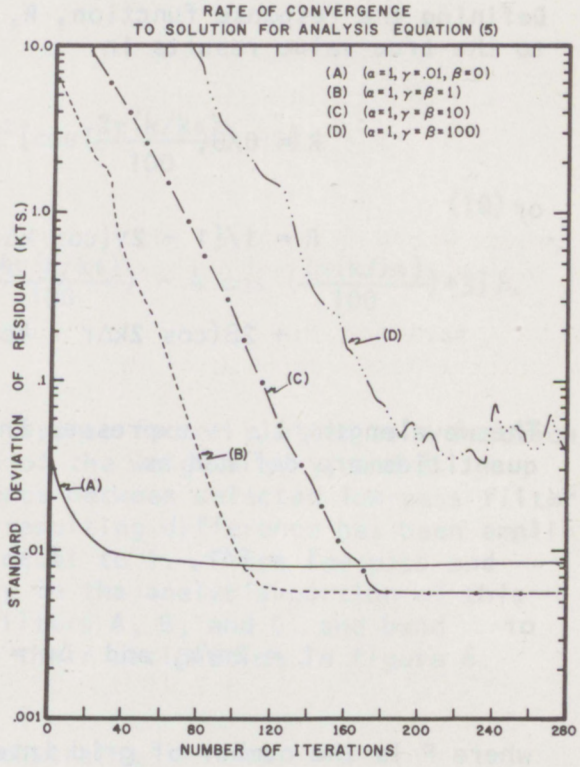

Figure 5. Rate of convergence to the solution of analysis equation (5).

Substituting (6) into (5) we obtain

$$Be^{ikn\Delta r}\{\beta[e^{2ik\Delta r} + e^{-2ik\Delta r} + 6 - 4e^{ik\Delta r} - 4e^{-ik\Delta r}]/\Delta r^4$$

$$- \gamma[e^{ik\Delta r} + e^{-ik\Delta r} - 2]/\Delta r^2 + \alpha\} = \alpha Ae^{ikn\Delta r},$$

or

$$\frac{Be^{ikn\Delta r}}{Ae^{ikn\Delta r}} = \alpha/\{\alpha - \gamma[2\cos k\Delta r - 2]/\Delta r^2$$

$$+ \beta[2\cos 2k\Delta r - 8\cos k\Delta r + 6]/\Delta r^4\}.$$

Defining the response function, R, to be the ratio of the analyzed value to the true value results in

$$R = \theta/\tilde{\theta},$$

or

$$R = 1/[1 - 2\gamma(\cos k\Delta r - 1)/\alpha\Delta r^2$$

$$+ 2\beta(\cos 2k\Delta r - 4\cos k\Delta r + 3)/\alpha\Delta r^4]. \qquad (7)$$

The wavelength, L, is expressed in multiples of the grid size. Desired quantities are defined as

$$L = P\Delta r, \qquad k = 2\pi/L,$$

or

$$L = 2\pi/k, \text{ and } \Delta r = L/P = 2\pi/kP, \qquad (8)$$

where P is the number of grid intervals per wavelength. Substituting from (8) into (7) for Δr in all locations, and for k in the argument of the cosine function, and introducing the factor k/k_0, where k_0 is some characteristic wave number taken as $2\pi/100$ n miles in this paper, we obtain

$$R = 1/\{1 - \frac{\alpha}{\gamma}\frac{\alpha k_0^{\,2} P^2}{2\pi^2}\left(\frac{k}{k_0}\right)^2\left[\cos\frac{2\pi}{P} - 1\right]$$

$$+ \frac{\beta}{\alpha}\frac{k_0^{\,2} P^4}{32\pi^4}\left(\frac{k}{k_0}\right)^4\left[\cos\left(\frac{4\pi}{P}\right) - 4\cos\left(\frac{2\pi}{P}\right) + 3\right]\}. \qquad (9)$$

Substituting for P in (9) where

$$P = L/\Delta r,\ k_0 = \frac{2\pi}{100 \text{ n mi}},\ k/k_0 = \frac{100}{L},\ \text{or } L = 100\left(\frac{k_0}{k}\right),$$

and

$$\Delta r = 1 \text{ n mi or finally, } P = 100/(k/k_0),$$

we obtain

$$R = 1/\{1 - \frac{\alpha}{\gamma}\frac{k_0^{\,2}}{2\pi^2}(100)^2\left[\cos\left(\frac{2\pi(k/k_0)}{100}\right) - 1\right]$$

$$\frac{\beta}{\gamma}\frac{k_0^{\,2}(100)^4}{32\pi^4}\left[\cos\left(\frac{4\pi(k/k_0)}{100}\right) - 4\cos\left(\frac{2\pi(k/k_0)}{100}\right) + 3\right]\}. \qquad (10)$$

Figure 6 illustrates the above response factor plotted as a function of the wavelength for selected values of the weights α, γ, and β. Figure 6 also illustrates the difference between selected low-pass filter response curves. In some cases, the resulting difference has been amplified to make the peak response value equal to 1. These low-pass and band-pass filters are used extensively in the analysis portion of this paper. They will be referred to as filters A, B, and C, and band filters D, E, and F, corresponding to their designation in figure 6.

3.2 Dynamic Constraint

A simple model that is sometimes applied to portions of the hurricane is the gradient wind model. The gradient wind equation represents a balance among the centrifugal, Coriolis, and pressure gradient forces. This condition results in circular motion parallel to the isobars and is believed to grossly describe the relationship between the wind and

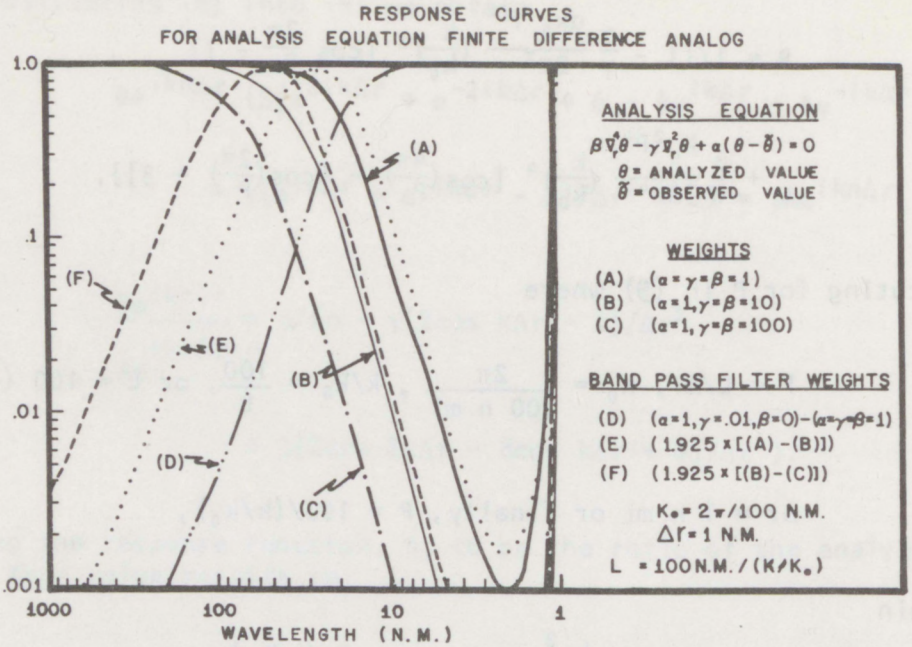

Figure 6. Response curves for the analysis equation for selected weights.

pressure in most of the high energy portion of the hurricane. This relationship per unit mass can be written mathematically as

$$\frac{c^2}{r} + fc - \frac{1}{\rho}\frac{\partial p}{\partial r} = 0, \qquad (11)$$

where

c is the gradient wind speed

r is the radial distance from the center of the circulation

p is pressure

ρ is the density, and

f is the Coriolis parameter. This parameter is assumed to be constant over the range of the storm in this paper, i.e., $f = 4.98802 \times 10^{-5}$ sec^{-1} at 20°N.

Equation (11) can be rewritten as

$$\frac{c^2}{r} + fc - g\frac{\partial z}{\partial r} = 0 \qquad (12)$$

where, by use of the hydrostatic approximation, the pressure gradient term is rewritten as

$$\frac{1}{\rho}\frac{\partial p}{\partial r} = g\frac{\partial z}{\partial r} .$$

A functional, containing the observational and gradient wind constraints and the two low-pass filters contained in J_1, can be written as

$$J_2 = \int_r \{\alpha(c - \tilde{v})^2 + \gamma(z - \tilde{z})^2 + \beta\left(\frac{c^2}{r} + fc - g\frac{\partial z}{\partial r}\right)^2 \tag{13}$$

$$+ \mu_1\left(\frac{\partial c}{\partial r}\right)^2 + \mu_2\left(\frac{\partial^2 c}{\partial r^2}\right) + \mu_3\left(\frac{\partial z}{\partial r}\right)^2 + \mu_4\left(\frac{\partial^2 z}{\partial r^2}\right)^2 \}dr.$$

The quantities μ_1, μ_2, μ_3, and μ_4 are the respective weights on the low-pass filters, and

α is the weight on the observed wind constraint,

γ is the weight on the observed height constraint,

β is the weight on the gradient wind constraint,

$\tilde{v}$ is the observed wind speed,

$\tilde{z}$ is the observed height of the designated pressure surface,

g is the acceleration due to gravity,

and the remaining variables are as previously defined.

The nondimensional finite difference analog for (13), as derived in appendix A, is

$$J_2 = \sum_r \{\alpha(c - \tilde{v})^2 + \gamma(z - \tilde{z})^2 + \beta\left(\frac{c^2}{r} + \frac{c}{R_0} - \frac{1}{F^2}\nabla_r z\right)^2 \tag{14}$$

$$+ \mu_1(\nabla_r c)^2 + \mu_2(\nabla_r{}^2 c)^2 + \mu_3(\nabla_r z)^2 + \mu_4(\nabla_r{}^2 z)^2\}\,\Delta r.$$

We wish to minimize the summation. Since all terms are quadratic, we take the first variation of the functional (14) with respect to c and z, and then set the result equal to zero. Using the rules of calculus of variations and integration by parts previously shown, we obtain

$$\delta_{c,z} J_2 = \delta_{c,z} \sum_r \{ \quad \} \Delta r$$

$$= \sum_r \{2\alpha(c - \tilde{v})\delta c + 2\gamma(z - \tilde{z})\delta z$$

$$+ 2\beta\left(\frac{c^2}{r} + \frac{c}{R_0} - \frac{1}{F^2}\nabla_r z\right)\left(-\frac{1}{F^2}\nabla_r(\delta z)\right)$$

$$+ 2\beta\left(\frac{c^2}{r} + \frac{c}{R_0} - \frac{1}{F^2}\nabla_r z\right)\left(\frac{2c}{r} + \frac{1}{R_0}\right)\delta c$$

$$- 2\mu_1 \nabla_r{}^2 c\delta c + 2\mu_2 \nabla_r{}^4 c\delta c - 2\mu_3 \nabla_r{}^2 z\delta z + 2\mu_4 \nabla_r{}^4 z\delta z\}\Delta r$$

$$= 0,$$

or

$$\delta_{c,z} J_2 = \Sigma\{[2\alpha(c - \tilde{v}) + 2\beta\left(\frac{c^2}{r} + \frac{c}{R_0} - \frac{1}{F^2}\nabla z\right)\left(\frac{2c}{r} + \frac{1}{R_0}\right)$$

$$- 2\mu_1 \nabla_r{}^2 c + 2\mu_2 \nabla_r{}^4 c]\delta c$$

$$+ [2\gamma(z - \tilde{z}) + 2\frac{\beta}{F^2}\left(\frac{1}{r}\nabla_r c^2 - \frac{c^2}{r^2} + \frac{1}{R_0}\nabla_r c - \frac{1}{F^2}\nabla_r{}^2 z\right)$$

$$- 2\mu_3 \nabla_r{}^2 z + 2\mu_4 \nabla_r{}^4 z]\delta z\}\Delta r = 0. \qquad (15)$$

Since δc and δz are arbitrary, we obtain

$$\beta\left[-\frac{1}{F^2}\left(\frac{2c}{r} + \frac{1}{R_0}\right)\nabla_r z + \frac{2c^3}{r^2} + \frac{3c^2}{rR_0} + \frac{c}{R_0{}^2}\right]$$

$$+ \mu_2 \nabla_r{}^4 c - \mu_1 \nabla_r{}^2 c + \alpha(c - \tilde{v}) = 0 \qquad (16)$$

and

$$\frac{\beta}{F^2}\left[-\frac{1}{F^2}\nabla_r{}^2 z + \frac{1}{R_0}\nabla_r c + \frac{1}{r}\nabla_r c^2 - \frac{c^2}{r^2}\right]$$

$$+ \mu_4 \nabla_r{}^4 z - \mu_3 \nabla_r{}^2 z + \alpha(z - \tilde{z}) = 0, \qquad (17)$$

where (16) and (17) are the resulting nondimensional finite difference analogs to the Euler-Lagrange or analysis equations for the functional (13). This set of analysis equations is solved by the Liebmann iterative technique as discussed in appendix A and the convergence to the solution is illustrated in figure 7.

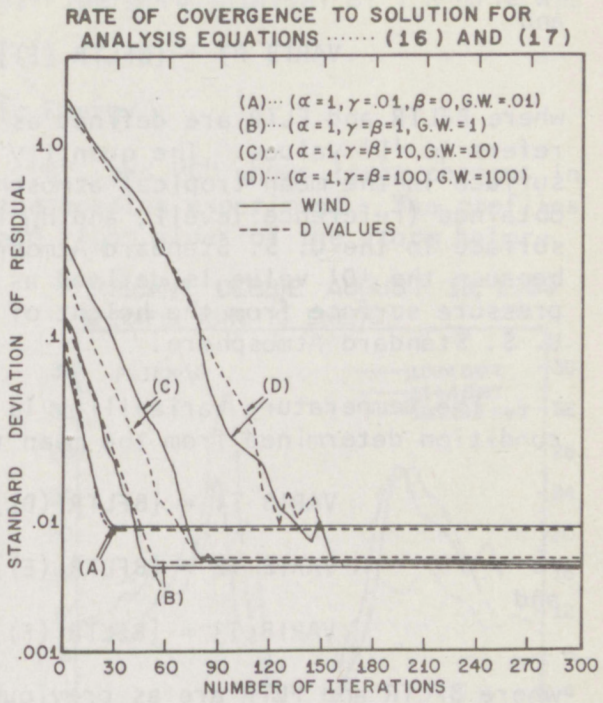

Figure 7. Rate of convergence to the solution of the analysis equations (16) and (17).

3.3 Variability Factors

The variability factors defined and used in this paper are similar to the typical gust factor used in wind analyses. However, the factors defined in this paper are for the selected scales of motion and are defined not only for the wind speed, but also for other standard meteorological parameters. This factor is determined from the filtered quantities and, except for the wind speed, uses Jordan's (1958) mean tropical conditions as a base. The mean tropical wind speed is assumed to be small in comparison with the hurricane wind speed and is therefore neglected.

The wind variability associated with scales of motion determined by band-pass filters D, E, and F are defined as

$$\text{VARIB W1} = [\text{BFLTR (D)}]/[\text{FLTR (A)}], \tag{18}$$

$$\text{VARIB W2} = [\text{BFLTR (E)}]/[\text{FLTR (B)}], \tag{19}$$

and

$$\text{VARIB W3} = [\text{BFLTR (F)}]/[\text{FLTR (C)}], \tag{20}$$

where BFLTR (D), (E), and (F) are the absolute values of the analyzed field obtained by applying band filters (D), (E), and (F) (fig. 2), respectively, to a set of observed wind data. Likewise, FLTR (A), (B), and (C) are the analyzed values obtained by applying filters (A), (B), and (C) to the same set of data.

The pressure variability is defined in the same manner as for the winds except that a base condition is applied using the mean tropical atmosphere. That is,

$$\text{VARIB P1} = [\text{BFLTR (D)}]/[\overline{H}_T - \overline{H}_U - \text{FLTR (A)}], \quad (21)$$

$$\text{VARIB P2} = [\text{BFLTR (E)}]/[\overline{H}_T - \overline{H}_U - \text{FLTR (B)}], \quad (22)$$

and

$$\text{VARIB P3} = [\text{BFLTR (F)}]/[\overline{H}_T - \overline{H}_U - \text{FLTR (C)}], \quad (23)$$

where BFLTR and FLTR are defined as above, except that the analysis now refers to 'D' values. The quantity $\overline{H}_T$ is the height of the pressure surface in the mean tropical atmosphere from which the 'D' value is obtained (reference level), and $\overline{H}_U$ is the height of that same pressure surface in the U. S. Standard Atmosphere. This factor is required because the 'D' value is defined as the height deviation of the given pressure surface from the height of that same pressure surface in the U. S. Standard Atmosphere.

The temperature variability is also defined, through use of a base condition determined from the mean tropical atmosphere, i.e.,

$$\text{VARIB T1} = [\text{BFLTR (D)}]/[\text{FLTR (A)} - 0.98\times\overline{T}], \quad (24)$$

$$\text{VARIB T2} = [\text{BFLTR (E)}]/[\text{FLTR (B)} - 0.98\times\overline{T}], \quad (25)$$

and

$$\text{VARIB T3} = [\text{BFLTR (F)}]/[\text{FLTR (C)} - 0.98\times\overline{T}], \quad (26)$$

where BFLTR and FLTR are as previously defined except that the analysis now refers to temperature, and $\overline{T}$ is the mean tropical temperature for the desired reference level. The arbitrary factor of 0.98 was used to avoid discontinuities that arise when the deviation approaches zero. In practice, the values for FLTR and $\overline{T}$ are used in degrees absolute.

The mixing ratio variability is defined as

$$\text{VARIB M1} = [\text{BFLTR (D)}]/[\text{FLTR (A)} - \overline{M}], \quad (27)$$

$$\text{VARIB M2} = [\text{BFLTR (E)}]/[\text{FLTR (B)} - \overline{M}], \quad (28)$$

and

$$\text{VARIB M3} = [\text{BFLTR (F)}]/[\text{FLTR (C)} - \overline{M}], \quad (29)$$

where all factors are as previously defined, but applied to the moisture field, and $\overline{M}$ is the mixing ratio value for the specified reference level in the mean tropical atmosphere.

4. ANALYSIS OF HURRICANE DEBBIE - AUGUST 18, 1969

The method of analysis described in section 2 is applied to the data collected in Hurricane Debbie on August 18, 1969. These data were recorded aboard the NOAA DC-6 aircraft and processed as described in section 2. The variables investigated are wind, temperature, moisture, and pressure. The data are assumed to be collected instantaneously on a

given pass. In actuality, the time required for the aircraft to make a single pass through the storm was approximately 20 to 30 min. These data are then averaged over small space and time intervals before being inserted into the analysis equations. The grid interval of 1 n mile was chosen for the analysis.

4.1 Kinetic Energy

The application of filters "A", "B", and "C" shows large changes in the kinetic energy occurred during the seeding experiment. The profiles shown in figure 8 are for the left and right sides of the storm before

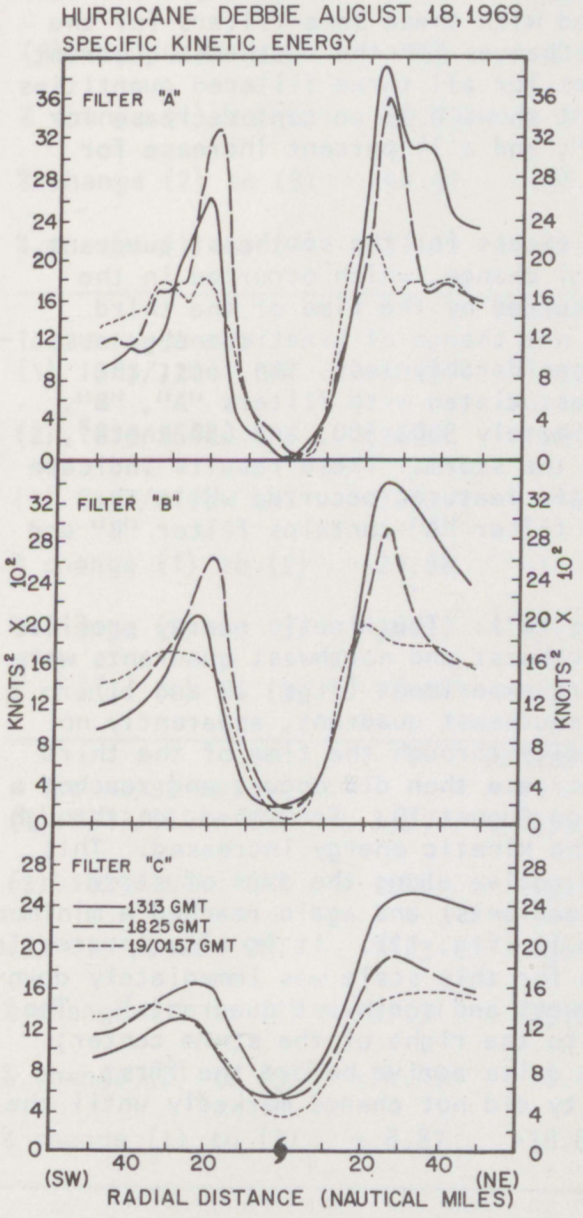

Figure 8. Kinetic energy profiles for the SW and NE quadrants of the storm.

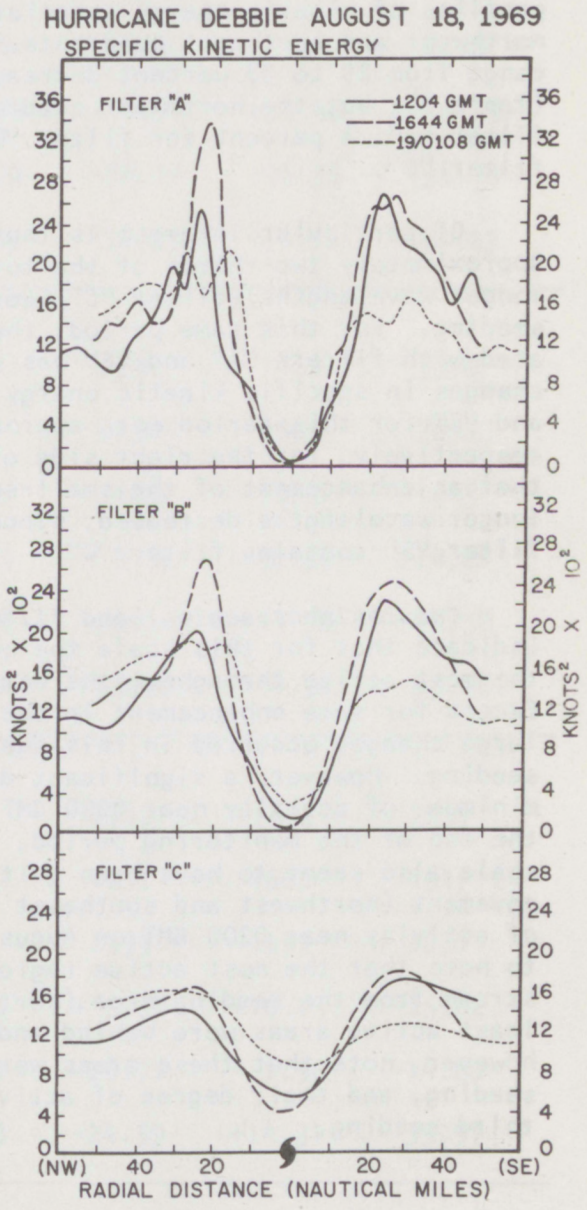

Figure 9. Kinetic energy profiles for the NW and SE quadrants of the storm.

seeding, immediately after the third seeding run, and finally some 4 hours after the final seeding event. These profiles exhibit a large decrease in the maximum value of the kinetic energy for the sum of all wavelengths represented. This total decrease amounted to approximately 40 percent for each filtered quantity for the northeast quadrant, or right side, of the storm. The left side shows a net decrease of 31 and 18 percent for the kinetic energy in the wavelengths represented by "A" and "B", respectively, but a net increase of 9 percent for those wavelengths associated with filter "C". The southwest quadrant, or left side, of the storm also had an increase in kinetic energy with time for larger radial distances from the storm center. Figure 9 shows the profiles of kinetic energy associated with these same filters for the northwest and southeast quadrants. Changes for the southeast quadrant range from 25 to 38 percent decreases for all three filtered quantities (table 1); but the northwest quadrant shows a 15 percent decrease for filter "A", 4 percent for filter "B", and a 14 percent increase for filter "C".

Of particular interest is that except for the southeast quadrant, approximately two-thirds of the total change, which occurred in the longer wavelengths (filter "C"), occurred by the time of the third seeding. For this same period, the net change of kinetic energy associated with filters "A" and "B" was considerably less. In fact, the changes in specific kinetic energy associated with filters "A", "B", and "C" for this period were approximately 300, 500, and 650 knots^2, respectively, for the right side of the storm. These results indicate that an enhancement of the small-scale features occurred while the longer wavelengths decreased, since filter "A" contains filter "B" and filter "B" contains filter "C".

Cumulonimbus scale (band filter "D"). The kinetic energy profiles indicate that for this scale the southwest and northwest quadrants were the most active throughout the entire experiment (figs. 10 and 11). Except for some enhancement in the southeast quadrant, apparently no large changes occurred in this quantity through the time of the third seeding. However, a significant decrease then did occur, and reached a minimum of activity near 0200 GMT on August 19. From then, on through the end of the monitoring period, the kinetic energy increased. This scale also seems to have been quite active along the axis of storm movement (northwest and southeast quadrants) and again reached a minimum of activity near 0200 GMT on August 19 (fig. 11). It is also interesting to note that the most active region for this scale was immediately downstream from the seeding area (northwest and southwest quadrants). The least active areas were behind and to the right of the storm center; however, note that these areas were quite active before the first seeding, and their degree of activity did not change markedly until the third seeding.

Table 1. Maximum Specific Kinetic Energy (kt^2) and Percent Changes for Hurricane Debbie on August 18, 1969.

OBS TIME	QUADRANT SW	NE	SE	NW	NET
		FILTER "A"			
(SW-NE/SE-NW)					
(1) 1313/1204 GMT	2604	3878	2625	2475	3878
(2) 1825/1644 GMT	3248	3537	2610	3328	3537
(3) 0157/0108 GMT	1789	2168	1613	2111	2168
% change (1) to (2)	+24.73	- 8.79	- 0.57	+34.46	- 8.79
% change (2) to (3)	-44.91	-38.70	-38.19	-36.56	-38.70
% change (1) to (3)	-31.29	-44.09	-38.55	-14.70	-44.09
		FILTER "B"			
(SW-NE/SE-NW)					
(1) 1313/1204 GMT	2049	3370	2251	1953	3370
(2) 1825/1644 GMT	2620	2891	2438	2661	2891
(3) 0157/0108 GMT	1667	1949	1486	1869	1949
% change (1) to (2)	+27.86	-14.21	+ 8.30	+36.25	-14.21
% change (2) to (3)	-36.37	-32.58	-39.04	-29.76	-32.58
% change (1) to (3)	-18.64	-42.16	-33.98	- 4.30	-42.16
		FILTER "C"			
(SW-NE/SE-NW)					
(1) 1313/1204 GMT	1307	2557	1712	1432	2557
(2) 1825/1644 GMT	1664	1917	1811	1663	1917
(3) 0157/0108 GMT	1423	1564	1291	1637	1637
% change (1) to (2)	+27.31	-25.02	+ 5.78	+16.13	-25.02
% change (2) to (3)	-14.48	-18.41	-28.71	- 1.56	-14.60
% change (1) to (3)	+ 8.87	-38.83	-24.59	+14.31	-35.97

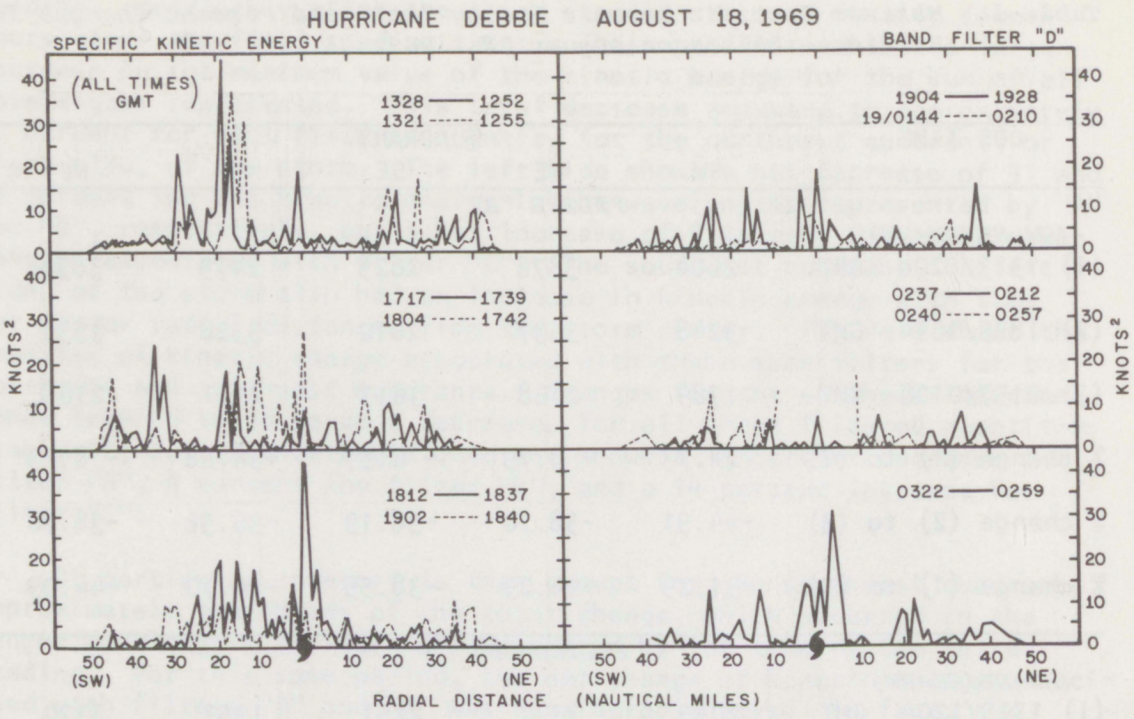

Figure 10. Kinetic energy profiles (~cumulonimbus scale) for the SW and NE quadrants of the storm.

The variability of the wind associated with the cumulonimbus scale (VARIB W1) is shown in figure 12. Before seeding, the maximum value of this variability outside the eyewall region was approximately 0.05. This value more than doubled through the early portion of the seeding runs on the southwest side of the storm center and remained nearly unchanged in the northeast quadrant. The horizontal variation of the wind in the southwest quadrant reached a minimum after the final seeding run, but appeared to be on the increase by the time of the final monitoring pass.

Rainband scale (band filter "E"). The response for the intermediate wavelengths (approximately rainband scale) indicates that the kinetic energy increased in the

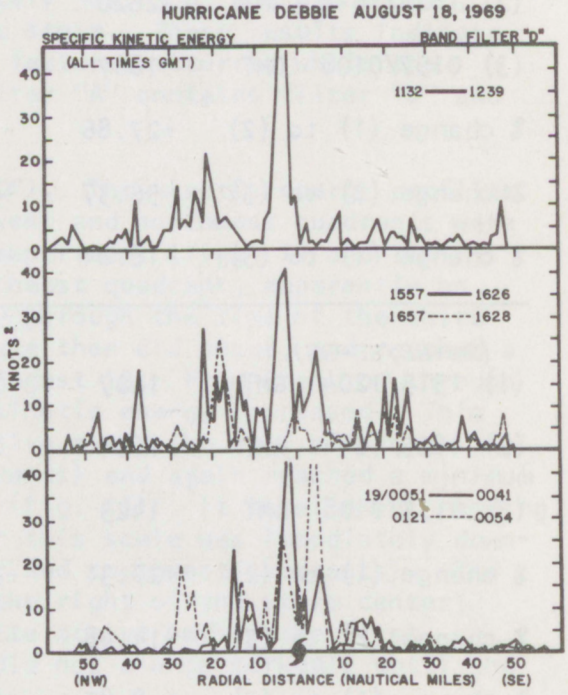

Figure 11. Kinetic energy profiles (~cumulonimbus scale) for the NW and SE quadrants of the storm.

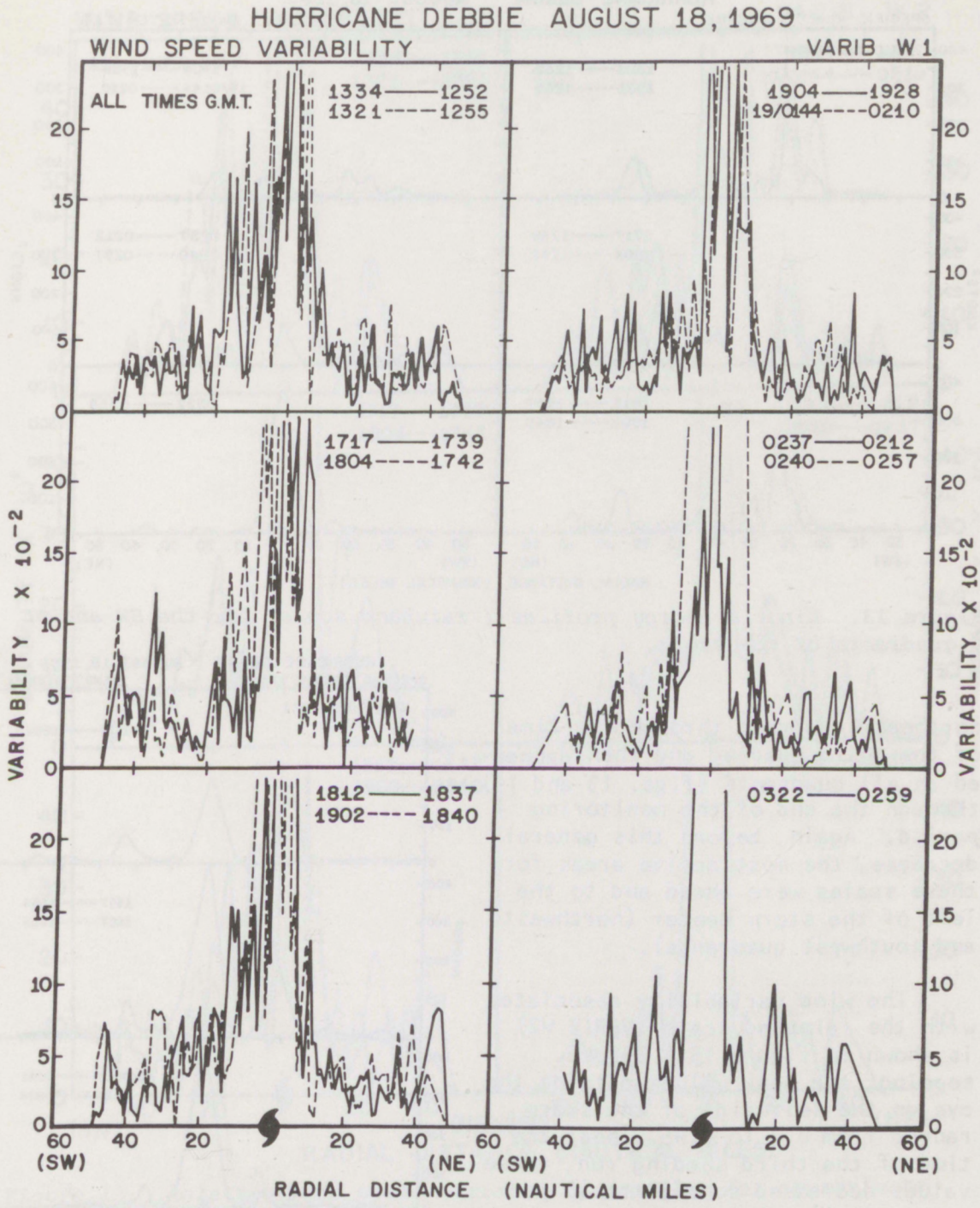

Figure 12. Relative wind speed variability profiles for approximate cumulonimbus scale (VARIB W1).

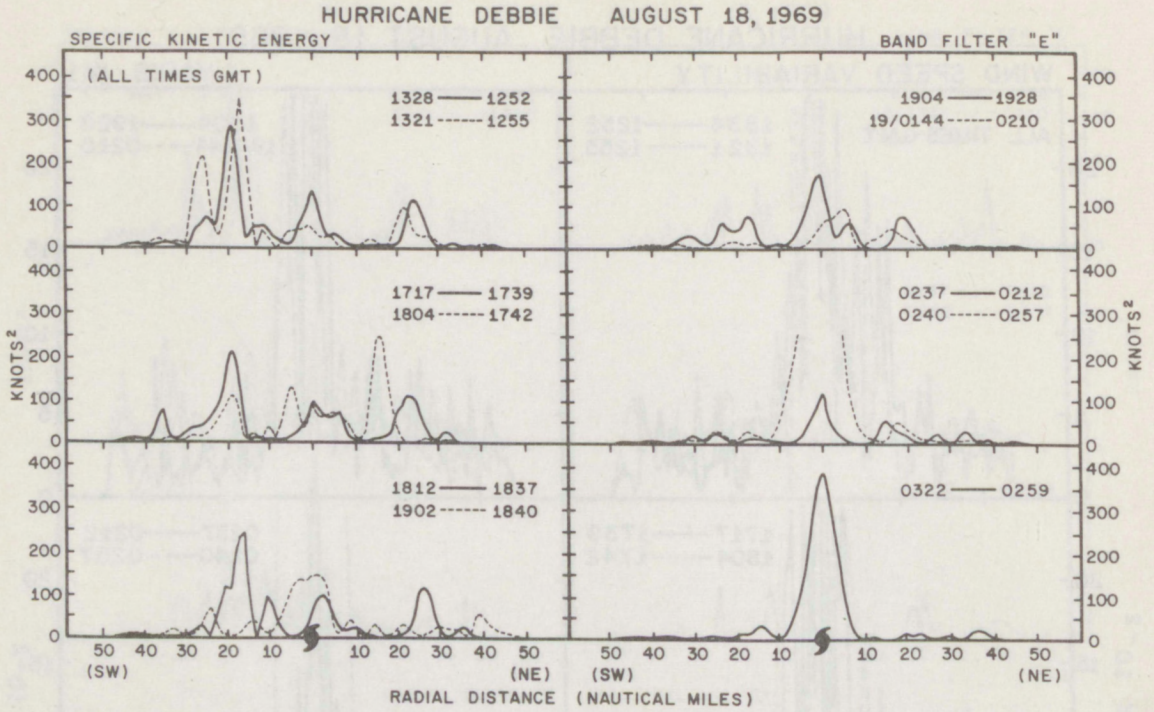

Figure 13. Kinetic energy profiles (~rainband scale) for the SW and NE quadrants of the storm.

northeast quadrant through the time of the third seeding and then dampened in all quadrants (figs. 13 and 14) through the end of the monitoring period. Again, before this general decrease, the most active areas for these scales were ahead and to the left of the storm center (northwest and southwest quadrants).

The wind variability associated with the rainband scale (VARIB W2) is shown in figure 15. Before seeding, the peak values outside the eye on the left side of the storm ranged from 0.3 to 0.45. Near the time of the third seeding run, these values decreased some 30 to 40 percent. During the same period, the values on the right side increased by 30 to 40 percent. The values became somewhat unsettled between the third and fourth seeding. This

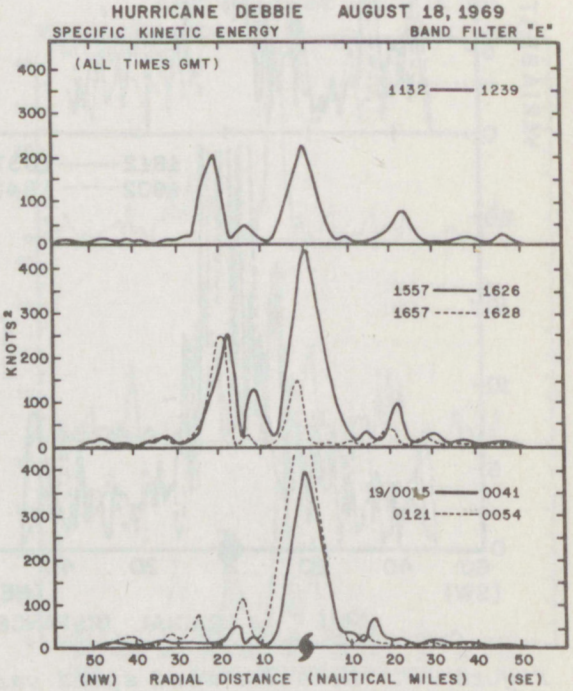

Figure 14. Kinetic energy profiles (~rainband scale) for the NW and SE quadrants of the storm.

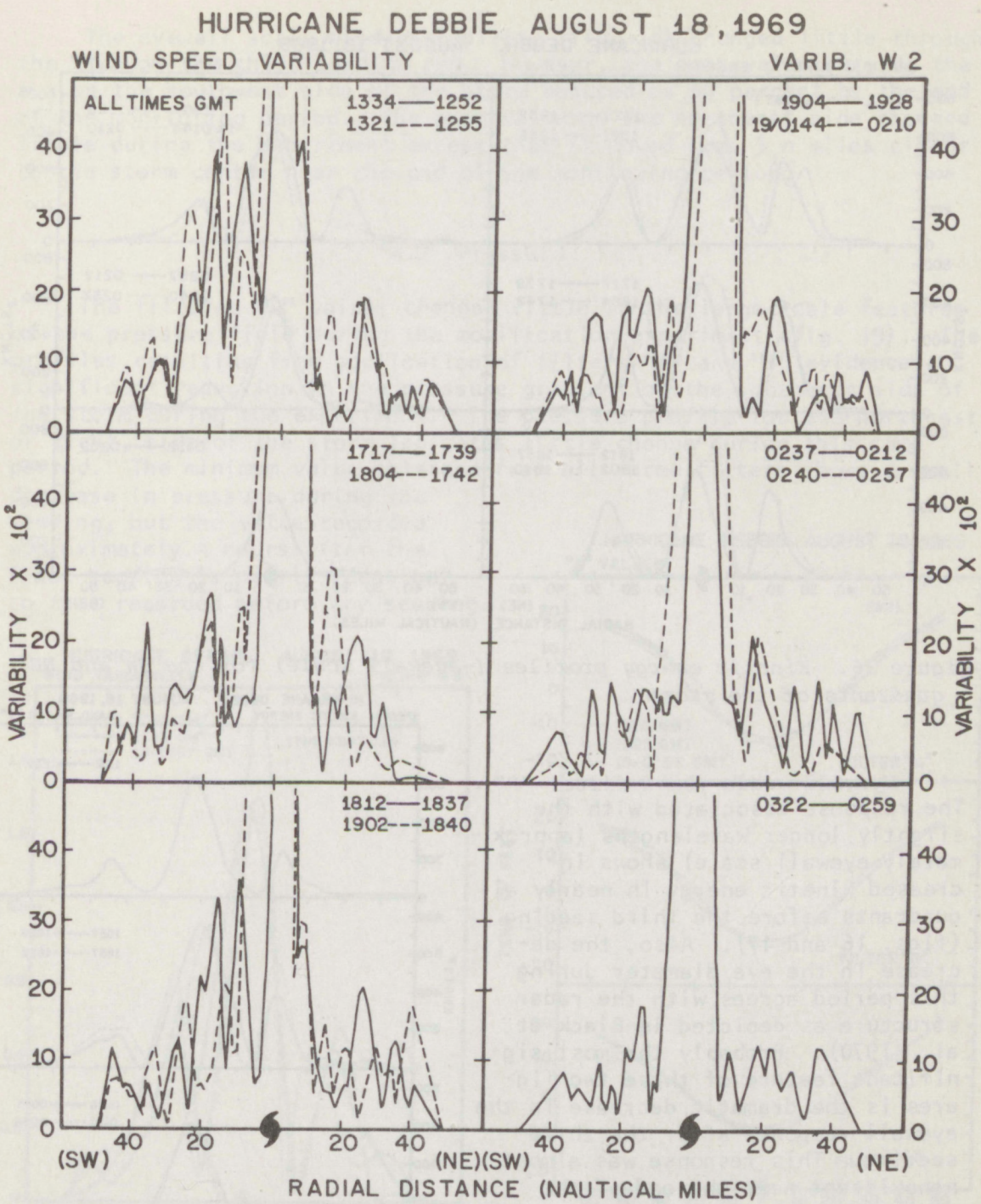

Figure 15. Relative wind speed variability profiles for approximate rainband scale motion (VARIB W2).

period was followed by a general reduction in the values for both sides of the storm. The peak values outside the eye for the final monitoring pass were approximately 0.1 as compared with the 0.3 to 0.4 values before the seeding events.

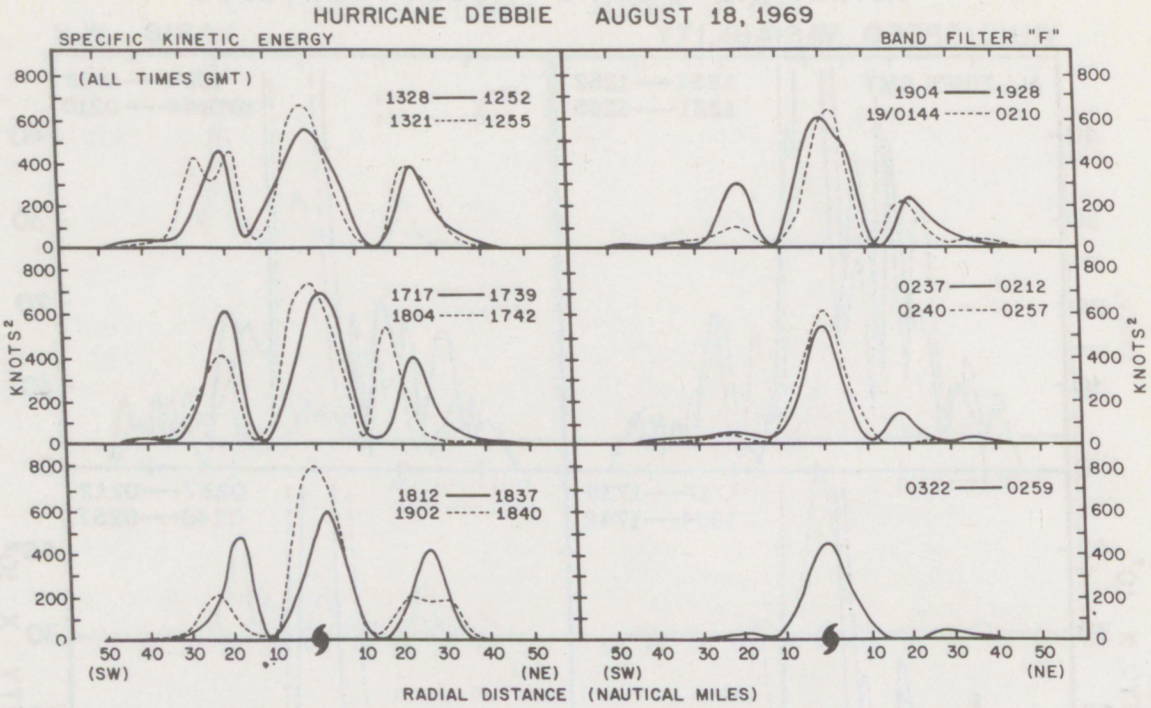

Figure 16. Kinetic energy profiles (~eyewall scale) for the SW and NE quadrants of the storm.

Eyewall scale (band filter "F"). The response associated with the slightly longer wavelengths (approximately eyewall scale) shows increased kinetic energy in nearly all quadrants before the third seeding (figs. 16 and 17). Also, the decrease in the eye diameter during this period agrees with the radar structure as depicted in Black et al. (1970). Probably the most significant feature of these two figures is the dramatic decrease in the eyewall response after the third seeding. This response was almost nonexistent near the end of the monitoring period. Note that the kinetic energy associated with this scale was generally twice as large as for the intermediate (rainband) scale and more than an order of magnitude larger than for the cumulonimbus scale.

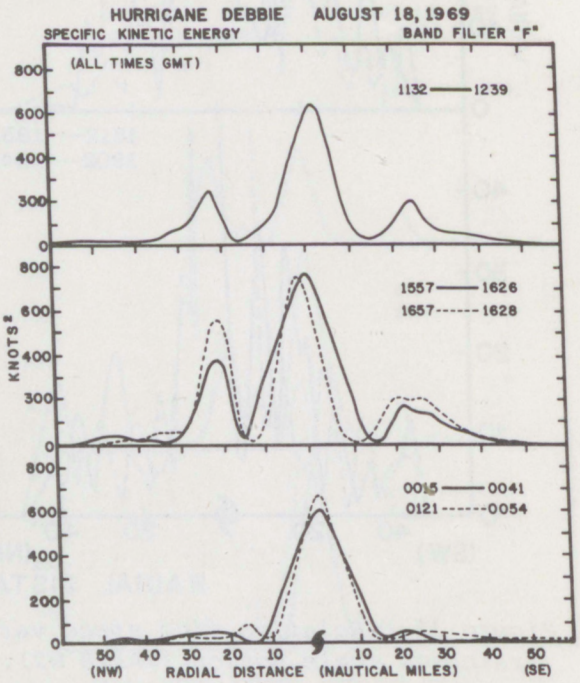

Figure 17. Kinetic energy profiles (~eyewall scale) for the NW and SE quadrants of the storm.

The eyewall scale wind variability (fig. 18) changed little through the time of the third seeding run. However, the peak value outside the eye on the southwest side of the storm reduced by 50 percent by the end of the monitoring period. The peak value on the northeast side changed little during the experiment except that it moved some 5 n miles closer to the storm center near the end of the monitoring period.

4.2 Pressure

The filtered "D" values changed little in the large-scale features of the pressure field during the modification experiment (fig. 19). The profiles resulting from application of filters "A" and "B" evidence a significant reduction in the pressure gradient on the southwest side of the storm during the experiment. The pressure profile for the northeast, or right, side of the storm indicates little change during this same period. The minimum value obtained from all three filters shows a small decrease in pressure during the seeding, but the value recorded approximately 4 hours after the final seeding is nearly identical to that recorded before any seeding.

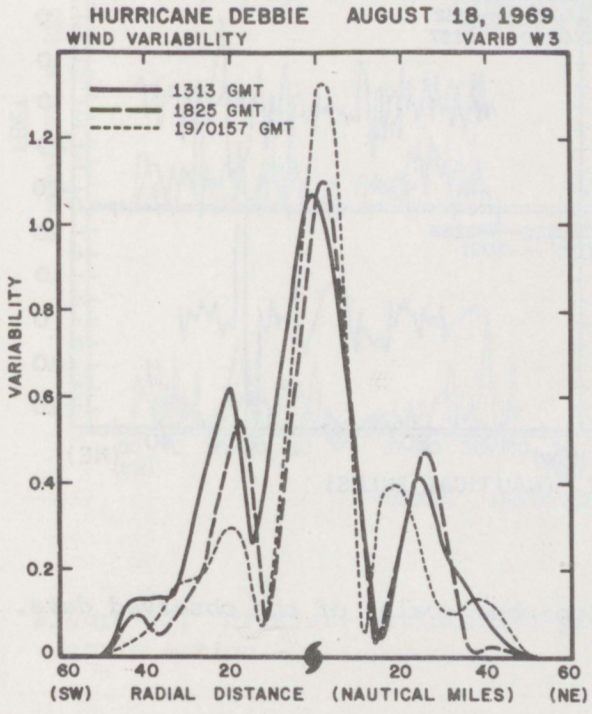

Figure 18. Relative wind speed variability profiles for approximate eyewall scale motion (VARIB W3).

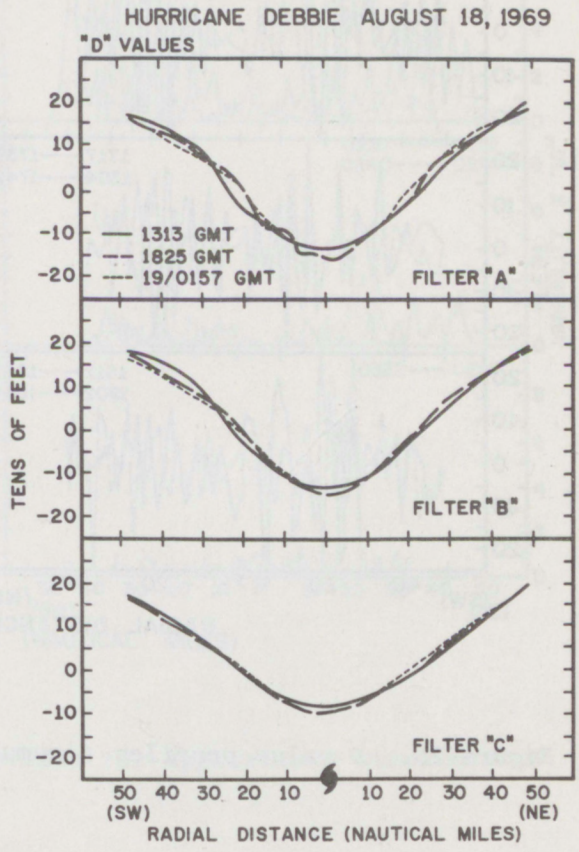

Figure 19. D value profiles from application of filters "A", "B", and "C" for before, during, and after the seeding events.

Cumulonimbus scale (band filter "D"). Many of the small-scale features, which were almost totally masked by the large-scale features shown in the previous figure, are readily observed in figure 20. These cumulonimbus scale features exhibit a large horizontal variability in time and space. However, the dominant feature in this time sequence of profiles appears to be the decrease in the magnitude of these band-filtered "D" values by the end of the seeding period. This reduction averages more than 50 percent over the horizontal distance depicted in these profiles.

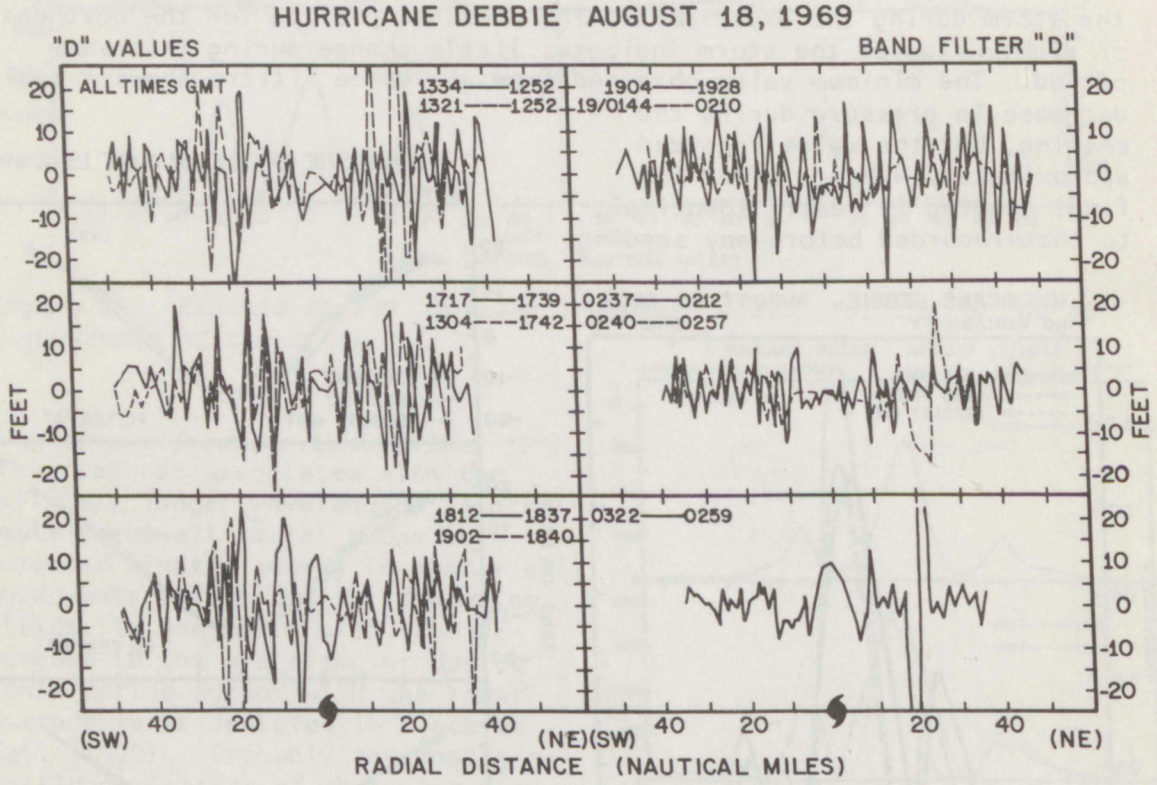

Figure 20. D value profiles (~cumulonimbus scale) of the observed data.

The pressure variability associated with the cumulonimbus scale (VARIB P1) was largest before the first seeding run (fig. 21). However, the most apparent change did not occur until after the third seeding. The variability then remained small for the remainder of the monitoring period, averaging about one-quarter of the value determined for the monitored period before the first seeding event.

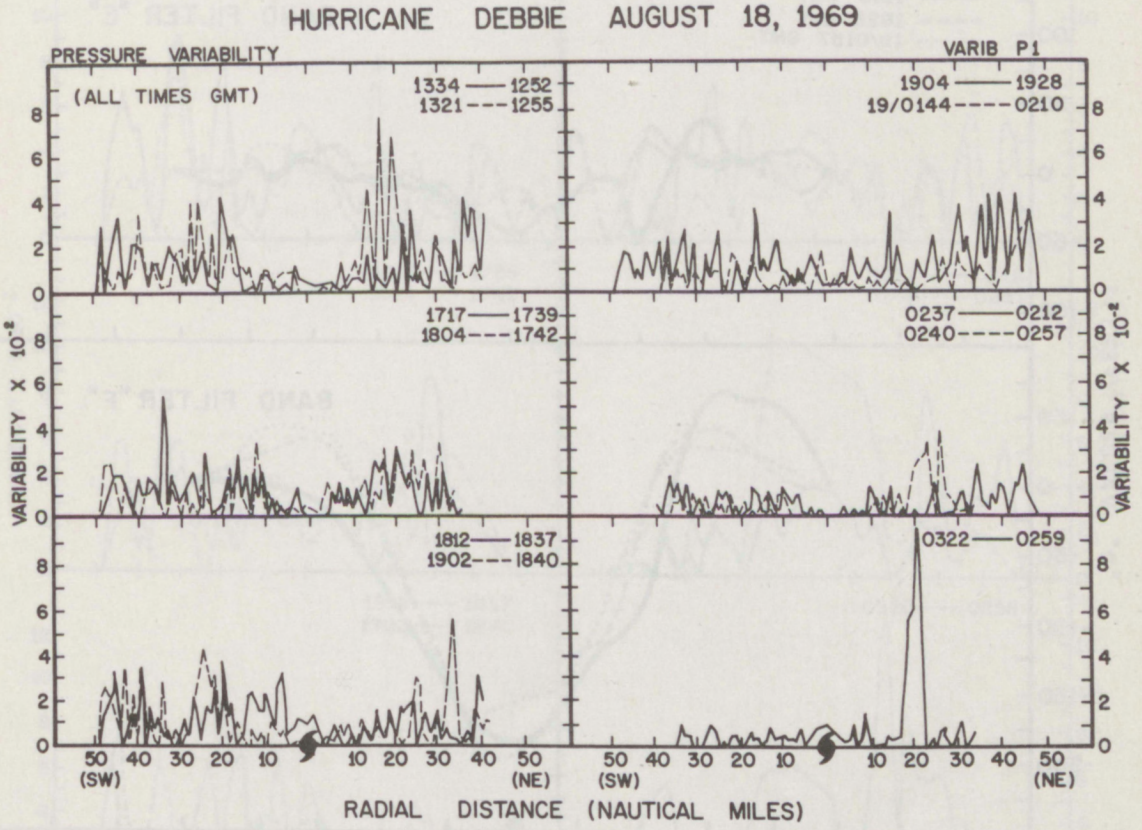

Figure 21. Pressure variability profiles for approximate cumulonimbus scale motion.

Rainband scale (band filter "E"). The band-filtered 'D' value profiles for the rainband scale also exhibited a reduction in pressure gradient, especially on the left, or southwest, side of the storm (fig. 22). Again, the magnitude of these values decreased by as much as 50 percent, with almost none of the change occurring before the third seeding.

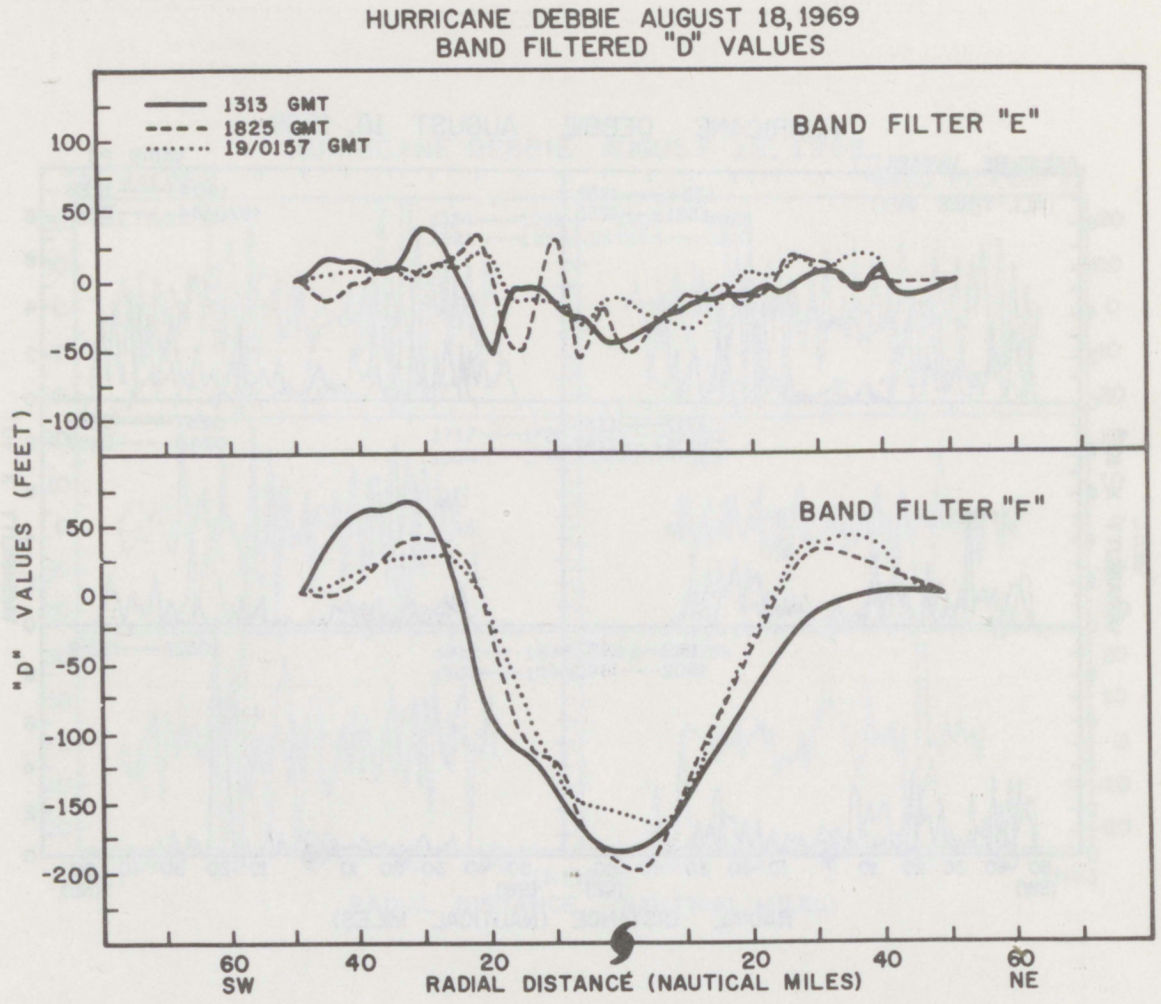

Figure 22. D value profiles (~rainband and eyewall scales) of the observed data.

The pressure variability for the rainband scale (VARIB P2) (fig. 23) exhibited nearly the same characteristics observed for the cumulonimbus scale. However, the final monitoring run revealed less horizontal variation, but the magnitude of this variability, exclusive of the eye region, increased markedly over that shown 1 hour earlier.

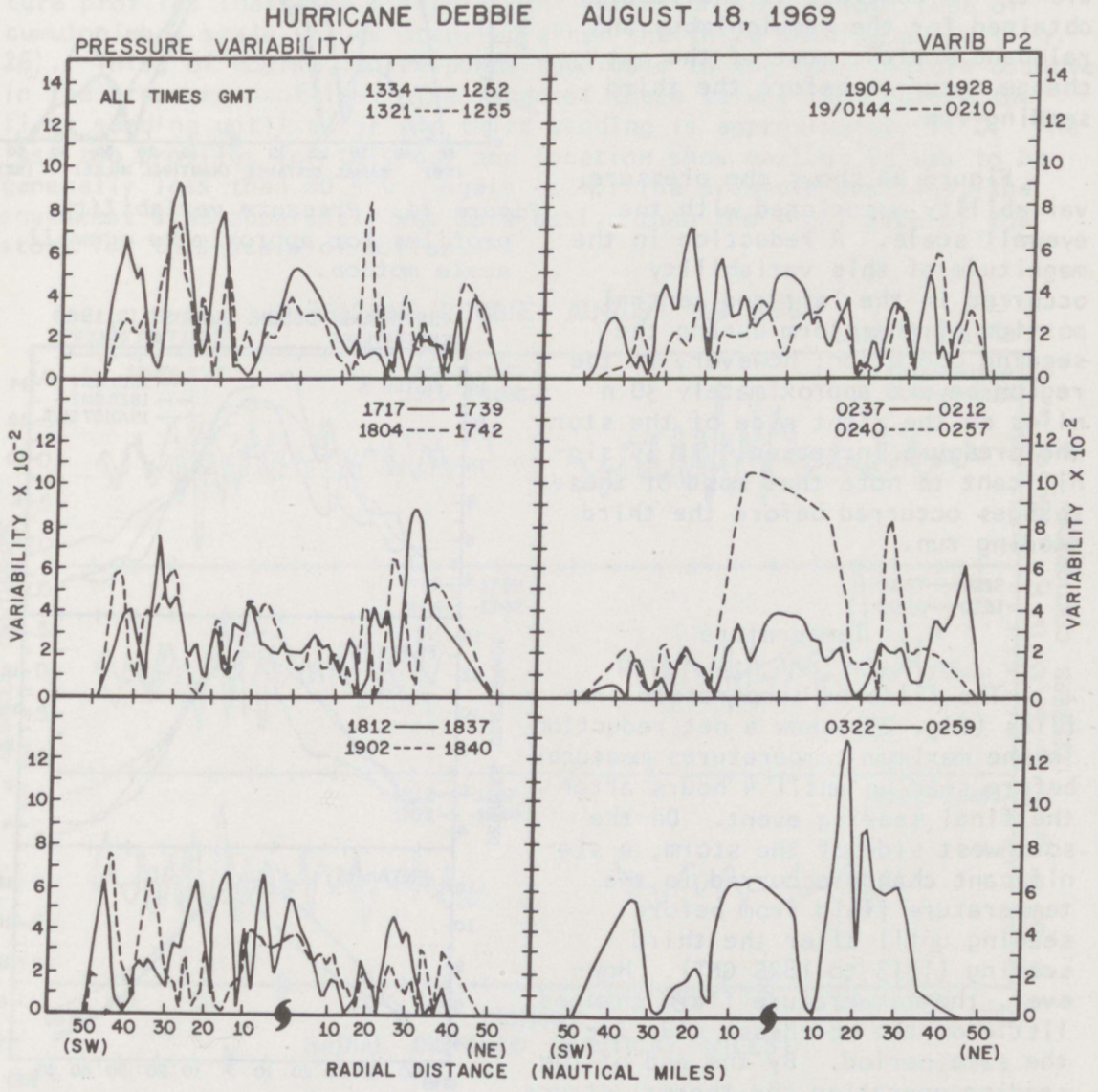

Figure 23. Pressure variability profiles for approximate rainband scale motion.

Eyewall scale (band filter "E"). The band-filtered 'D' value for the eyewall scale (~50 n miles) shows a net reduction in the minimum value and the maximum value on the left side of the storm (fig. 22). However, the right side shows an increase in maximum value and gradient. In contrast to the results obtained for the cumulonimbus and rainband scales, most of the net change occurred before the third seeding run.

Figure 24 shows the pressure variability associated with the eyewall scale. A reduction in the magnitude of this variability occurred in the left and central portion of the storm during the seeding operation; however, in the region beyond approximately 30 n miles on the right side of the storm the pressure increased. It is significant to note that most of these changes occurred before the third seeding run.

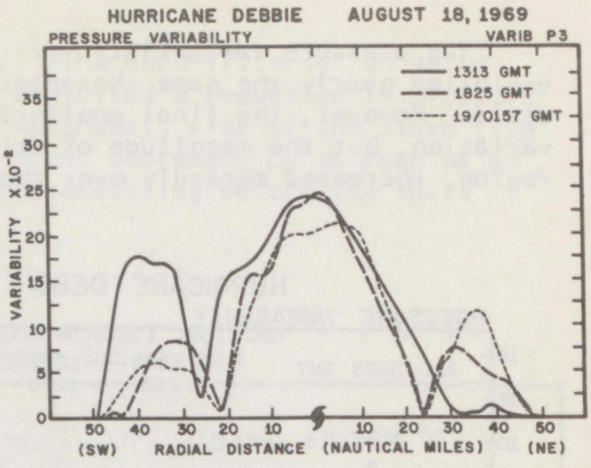

Figure 24. Pressure variability profiles for approximate eyewall scale motion.

4.3 Temperature

The filtered temperature profiles (fig. 25) show a net reduction in the maximum temperatures measured before seeding until 4 hours after the final seeding event. On the southwest side of the storm, a significant change occurred in the temperature field from before seeding until after the third seeding (1313 to 1825 GMT). However, the temperature field changed little on the northeast side for the same period. By the end of the seeding operation, the thermal structure on the southwest side of the storm returned to a state similar to that observed before the first seeding event (except for the eye and eyewall region). However, a significant change took place on the northeast side of the storm

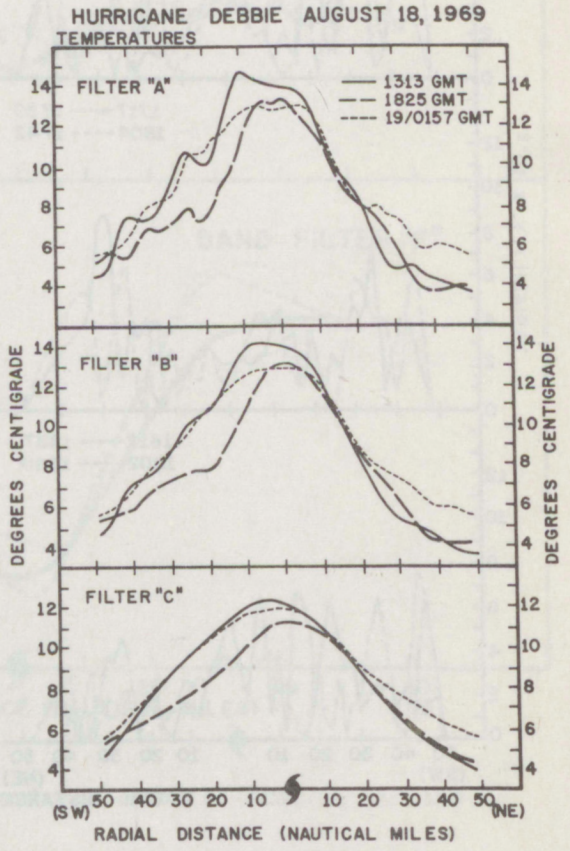

Figure 25. Temperature profiles obtained by application of filters "A", "B", and "C" for the periods of before, during, and after the seeding events.

where, in the outer regions, the temperature increased by approximately 2°C after the third seeding. This change occurred in the longer wavelengths, as evidenced by nearly the same change occurring for the value obtained from applying filter "C" as compared with that obtained by filter "A". Most of the temperature reduction taking place over the central region occurred in the shorter wavelengths.

Cumulonimbus scale (band filter "D"). The time sequence of temperature profiles indicates a significant reduction in the magnitude of cumulonimbus scale values occurred after the third seeding event (fig. 26). This, of course, corresponds favorably to the same feature observed in the pressure profiles. The range of these values from before the first seeding until after the third seeding is approximately ±1°C. The last two profiles for this day and location show maximum values to be generally less than ±0.5°C. Again as for the pressure profiles, the southwest side apparently was more active than the right side of the storm for this scale of motion.

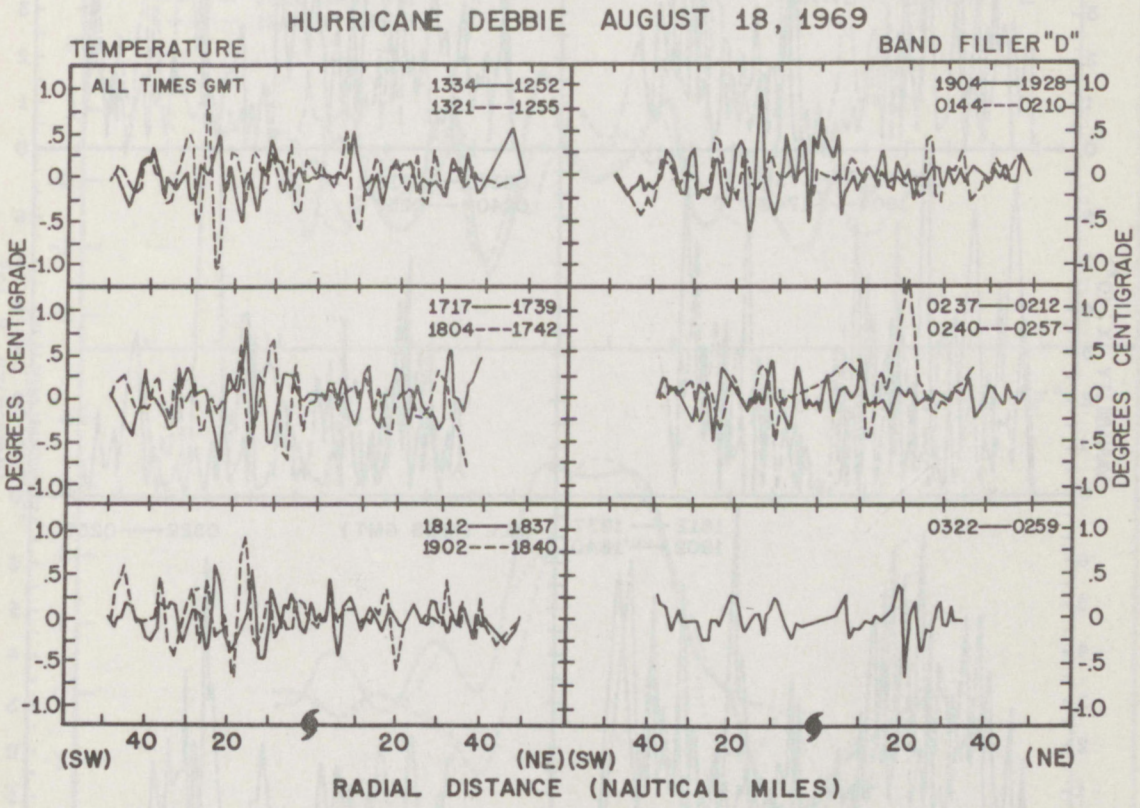

Figure 26. Temperature profiles for approximate cumulonimbus scale.

The cumulonimbus scale temperature variability (VARIB T1) increased slightly up through the time of the third seeding and then decreased markedly, as noted for the pressure profiles (fig. 27). This reduction generally exceeded 50 percent. Again, the southwest side in general appears to have been more active than the northeast side. However, the northeast side was quite active at times and near the end of the monitoring period even surpassed the southwest side. The sensitivity of this parameter is readily observed in the large variations over short time and space intervals.

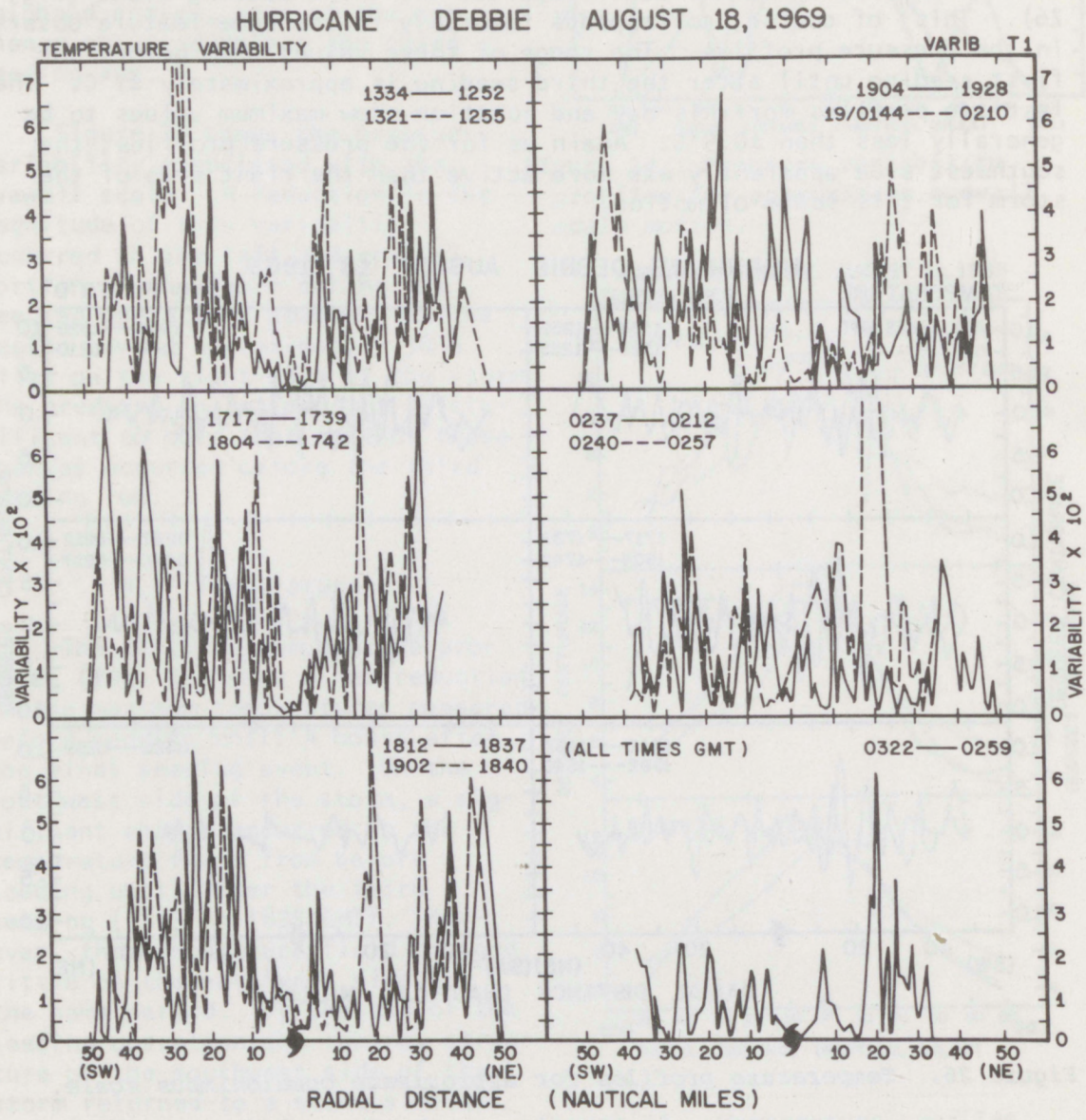

Figure 27. Temperature variability profiles for approximate cumulonimbus scale motion.

Rainband scale (band filter "E"). The rainband scale temperature profiles show maximum values to be about 1.5 times greater than those associated with the cumulonimbus scale (fig. 28). Again, of particular significance is the reduction in the amplitude of the temperature profile that occurred during the modification experiment.

As expected, the temperature variability for the rainband scale (VARIB T2) appears to be more conservative (fig. 29) than for the cumulonimbus scale. This same trend is noted for the rainband scale as for the cumulonimbus scale. That is, the magnitude of the parameter apparently increased during the early seeding periods and then decreased markedly after the third seeding event, when the average value decreased by 30 to 40 percent.

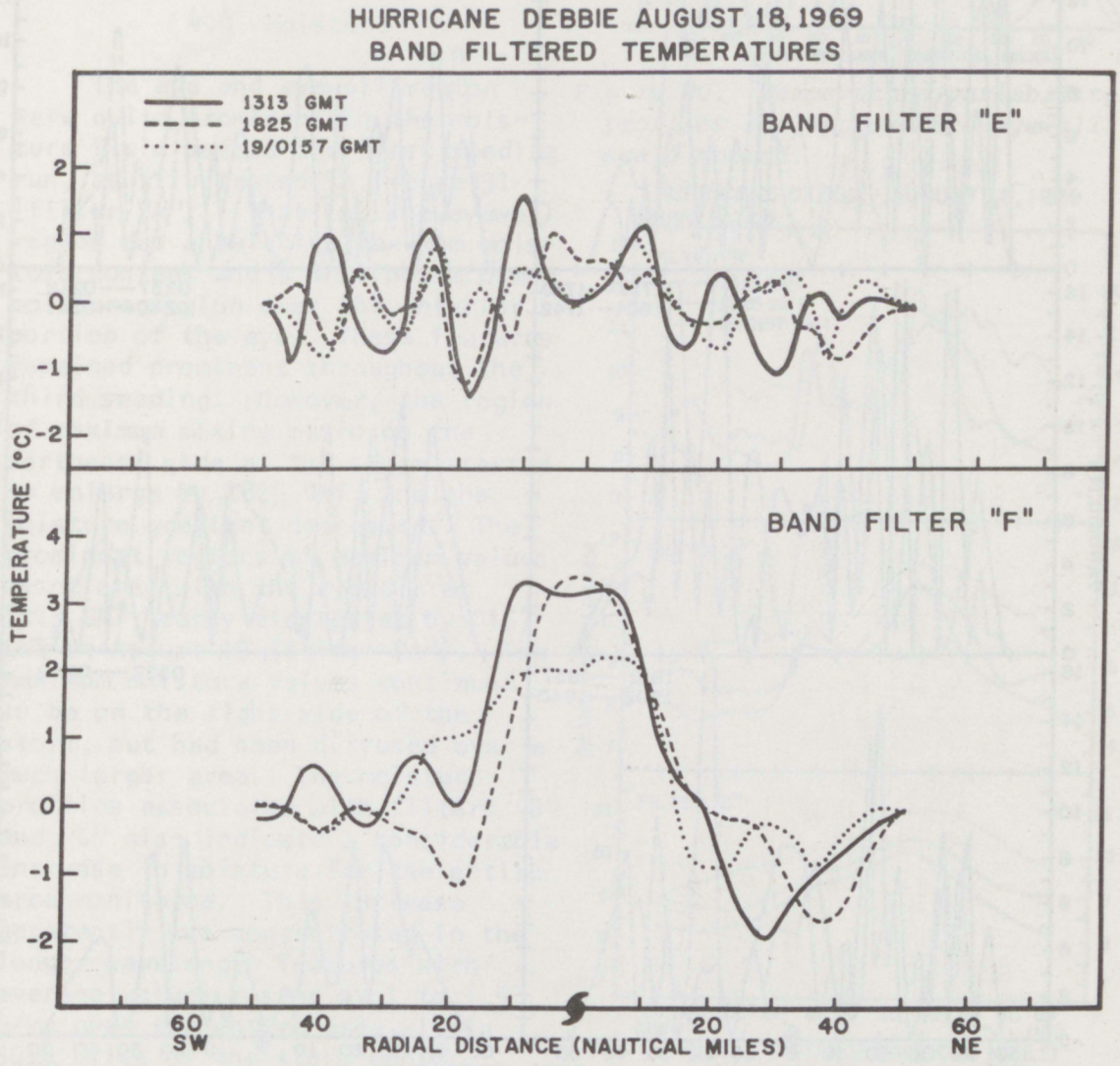

Figure 28. Temperature profiles for approximate rainband and eyewall scales.

Eyewall scale (band filter "F"). The eyewall scale temperature profiles (fig. 28) also indicate that a reduction in amplitude occurred with the passage of time. Of particular interest is the reduction in the temperature gradient in the eyewall region (approximately 15 to 30 n miles from the storm center) for this scale of motion. Furthermore, the temperature reduction over the central region exceeded 1°C for this scale, indicating that the reduction of temperature noted over the central regions in figure 25 was primarily concentrated in the eyewall scale.

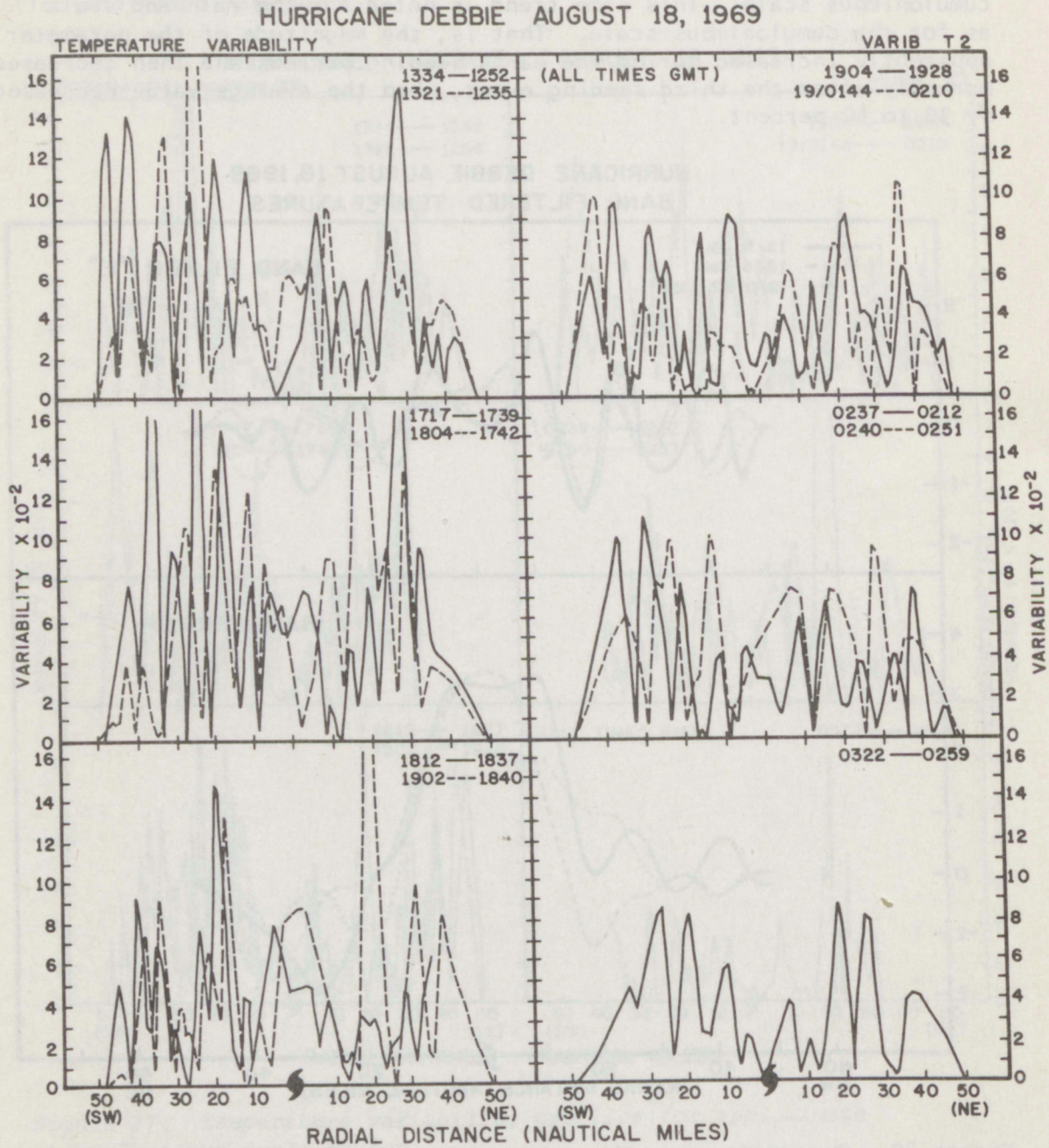

Figure 29. Temperature variability profiles for approximate rainband scale motion.

The eyewall scale temperature variability (VARIB T3) exhibits the most dramatic change of these three temperature variability parameters (fig. 30). Reductions of 57, 37, and 52 percent in the maximum value of this parameter for the southwest, central, and northeast portions of the storm, respectively, occurred during the monitoring period. As we noted for the previous parameters, most of this change took place after the third seeding event.

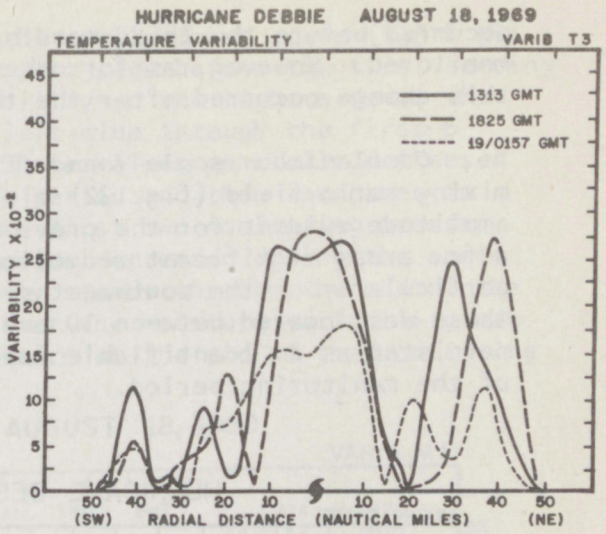

Figure 30. Temperature variability profiles for approximate eyewall scale motion.

4.4 Moisture

The eye and eyewall region were quite prominent in the moisture field before the first seeding run, as illustrated in figure 31 (filter "A"). That is, the eyewall region had a relative maximum moisture content and a distinct minimum moisture region over the interior portion of the eye. These features remained prominent throughout the third seeding. However, the region of maximum mixing ratio on the northeast side of the storm started to enlarge by 1825 GMT, and the moisture gradient decreased. The prominent regions of maximum values associated with the eyewall at 1313 GMT nearly dissipated by 0157 GMT on August 19 (filter "A"). The maximum moisture values continued to be on the right side of the storm, but had been diffused over a much larger area. The moisture profiles associated with filters "B" and "C" also indicate a considerable increase in moisture for the entire area monitored. This increase apparently was concentrated in the longer wavelength features with average values rising by 1 to 1.5 g/kg over the entire area within 50 n miles of the storm center. Also of interest is that a significant portion of this increase

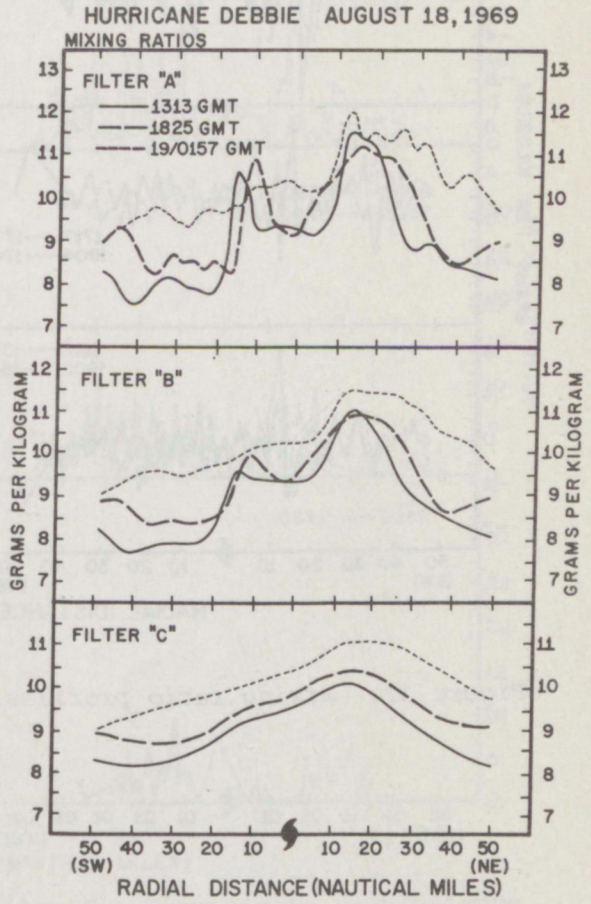

Figure 31. Mixing ratio profiles before, during, and after the seeding events.

occurred before the third seeding, especially in the outer regions monitored. However, as for other parameters, the greatest portion of this change occurred after the third seeding event.

Cumulonimbus scale (band filter "D"). The cumulonimbus scale mixing ratio field (fig. 32) did not exhibit the major reduction in amplitude evident for the previously discussed parameters. However, in a few areas significant reductions in the extreme values did occur particularly on the southwest side of the storm. The most prominent of these was located between 10 and 20 n miles left of the storm center and persisted as an identifiable feature through more than the first 6 hours of the monitoring period.

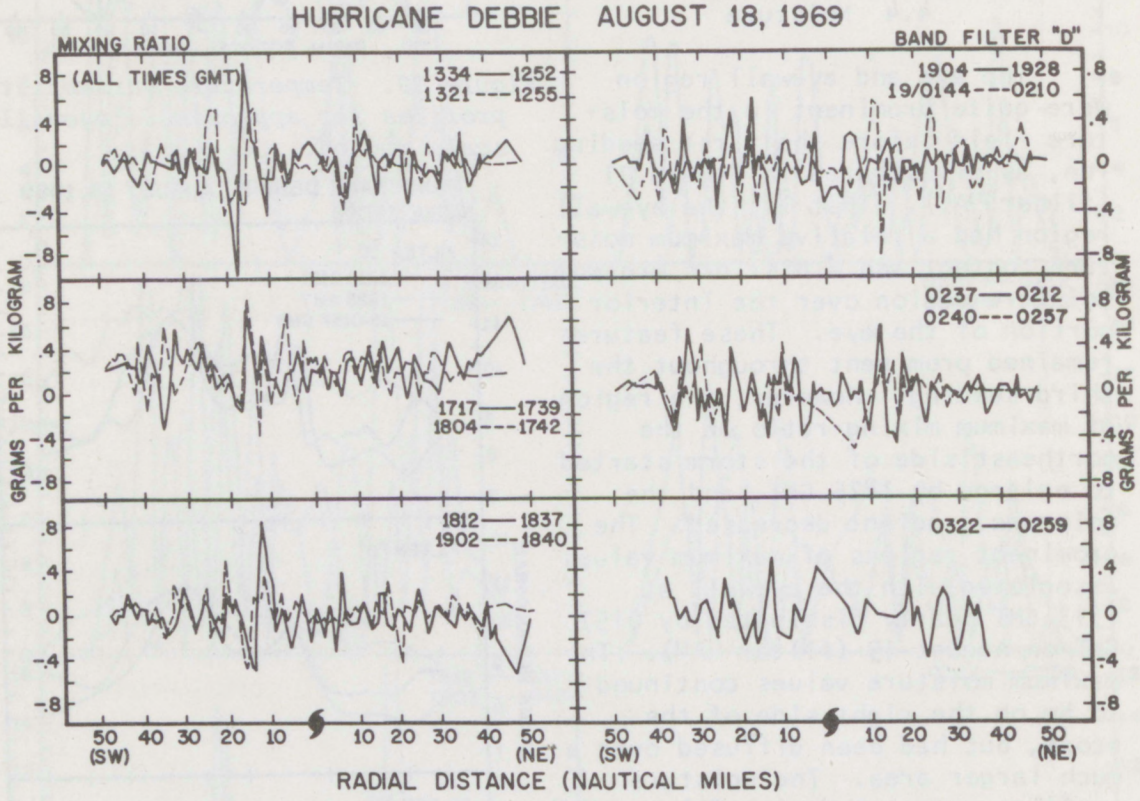

Figure 32. Mixing ratio profiles for approximate cumulonimbus scale.

The mixing ratio variability for the cumulonimbus scale (VARIB M1) had maximum values located on the southwest side before the first seeding (fig. 33). The magnitude of the variability on the right side of the storm was about one-half that for the left side through the first 6 or 7 hours of the monitoring period. These values generally decreased by about 40 percent through the seeding period and then increased to values as large as those observed on the first two monitoring passes. Simultaneously, the values on the east side decreased during the early seeding runs and then remained relatively steady through the end of the monitoring period. The net result is that the moisture variability was nearly the same for both sides of the storm at the end of the monitoring period.

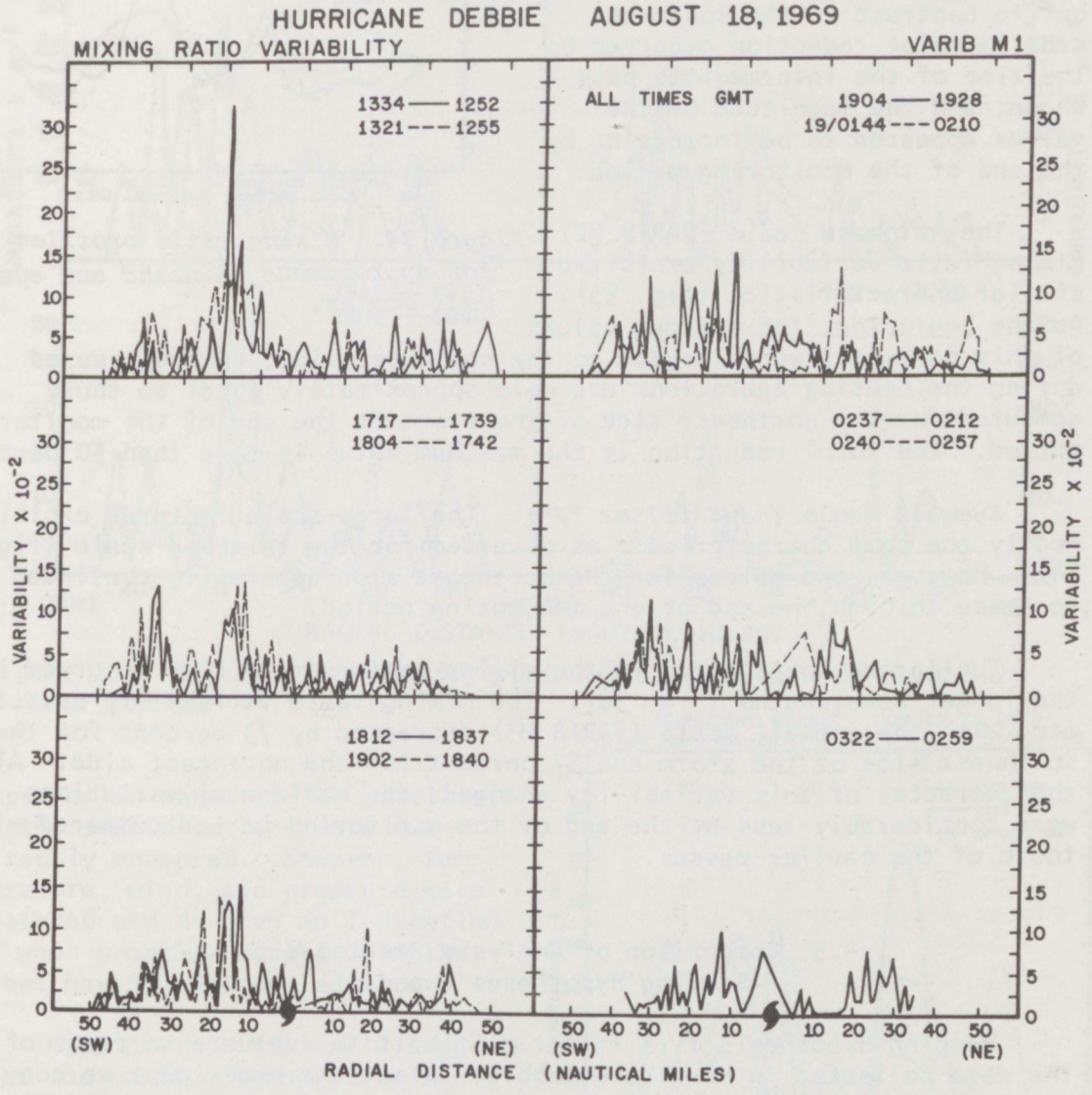

Figure 33. Moisture variability profiles for approximate cumulonimbus scale motion.

Rainband scale (band filter "E"). The magnitude of the values of the rainband scale mixing ratio profiles (fig. 34) decreased during the monitoring period, particularly on the southwest side of the storm. By the end of the monitoring period, the resulting values were less than 0.5 g/kg for this area. Most of this change occurred after the third seeding run. The northeast section did not show as large a net change, but in contrast to the southwest side, a major reduction occurred by the time of the intermediate pass shown, and the magnitude of the values appeared to be increasing by the end of the monitoring period.

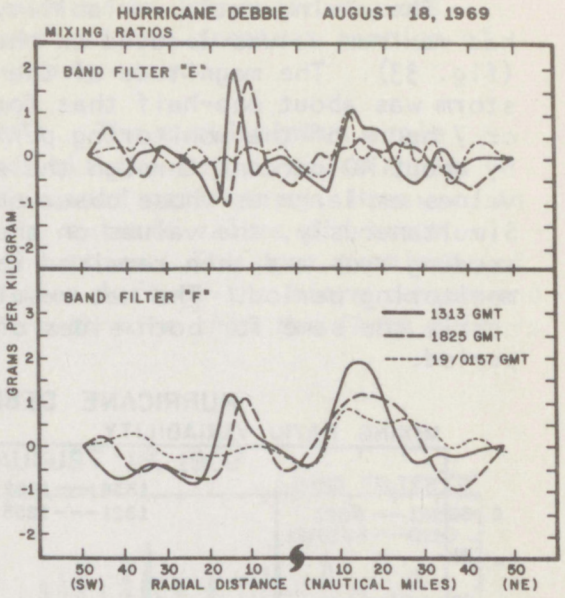

Figure 34. Mixing ratio profiles for approximate rainband and eyewall scales.

The rainband scale (VARIB M2) mixing ratio variability exhibited similar characteristics (fig. 35). At the beginning, the maximum values of this parameter were largest on the southwest side; they decreased during the seeding operations and were approximately equal to those computed for the northeast side of the storm at the end of the monitoring period. The total reduction in the maximum value is more than 50 percent.

Eyewall scale (band filter "F"). The large-scale features exhibited nearly the same characteristic as observed for the rainband scale (fig. 34). However, the values for the northeast side apparently continued to decrease through the end of the monitoring period.

The largest net change in the mixing ratio variability occurred in the longer wavelengths (fig. 36). The mixing ratio variability associated with the eyewall scale (VARIB M3) decreased by 73 percent for the southwest side of the storm and 57 percent for the northeast side. Also, the character of this variability changed; the horizontal variations were considerably less by the end of the monitoring period compared with those of the earlier passes.

4.5 Comparison of Analysis Results With Seeding Hypotheses I and II

Seeding Hypothesis I is rather difficult to evaluate in terms of the data collected in Hurricane Debbie. Also, the experiment as conducted was not exactly as that proposed in seeding Hypothesis I. That is, the seeding was not confined to the eyewall region, but extended some distance outward from the eyewall. The change in the ratio of the

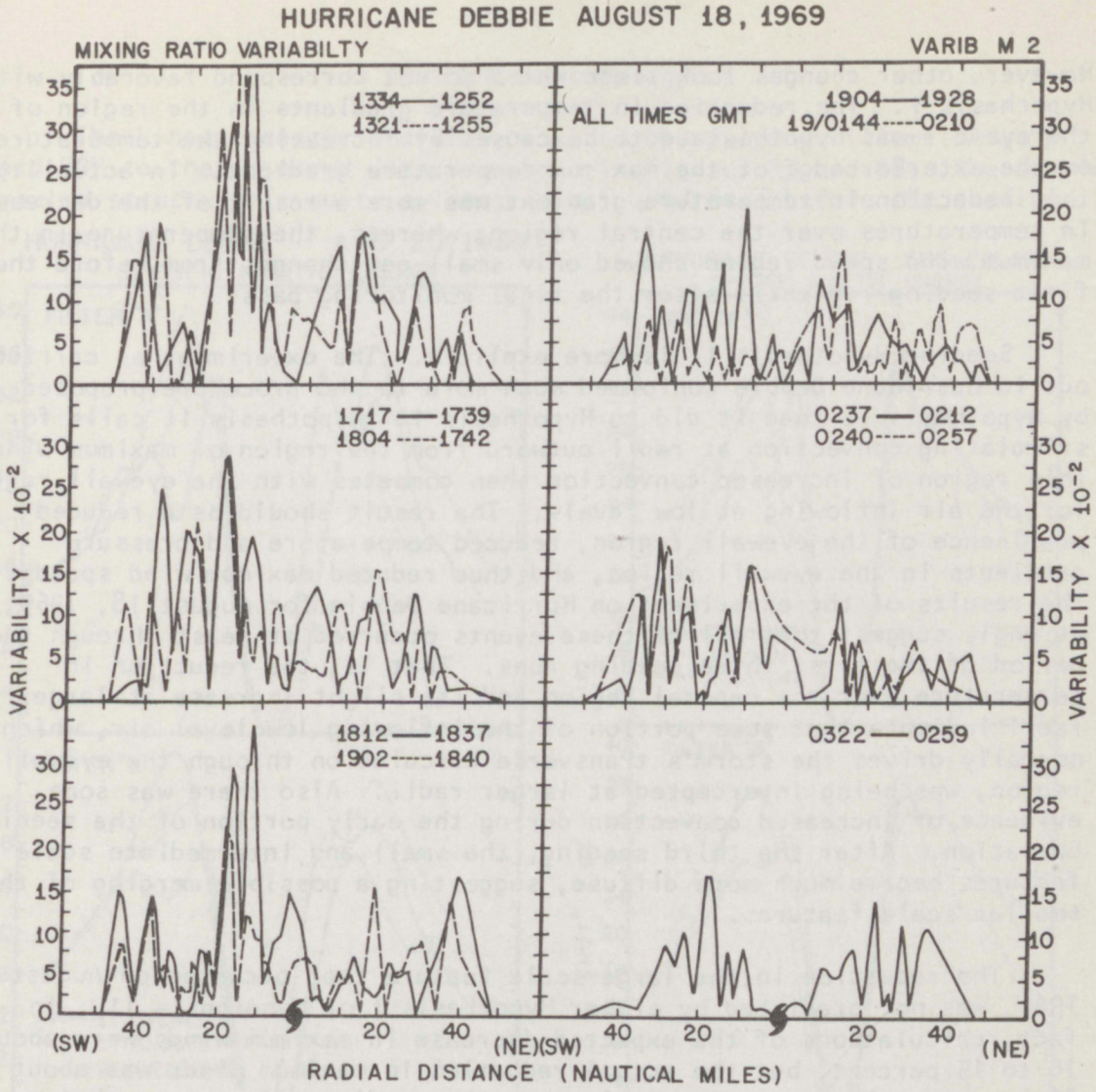

Figure 35. Moisture variability profiles for approximate rainband scale motion.

supercooled water-to-ice particles in the seeded regions were not directly measured. However, temperature, wind, and pressure were measured and do give an indication of what probably occurred in the areas having supercooled water.

Hypothesis I basically suggests that the maximum temperature and pressure gradients should reduce along with the maximum wind speeds. These conditions all occurred, as discussed in the previous analysis.

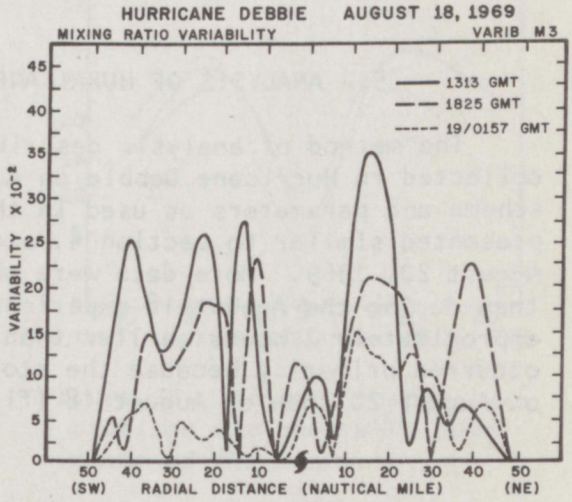

Figure 36. Moisture variability profiles for approximate eyewall scale motion.

However, other changes took place which do not correspond favorably with Hypothesis I. The reduction in temperature gradients in the region of the eyewall was hypothesized to be caused by increasing the temperature on the exterior edge of the maximum temperature gradient. In actuality, this reduction in temperature gradient was more a result of the decrease in temperatures over the central region; whereas, the temperature in the maximum wind speed region showed only small net changes from before the first seeding run until after the final monitoring pass.

Seeding Hypothesis II is more explicit. The experiment as carried out in Hurricane Debbie conformed much more to the procedure proposed by Hypothesis II than it did to Hypothesis I. Hypothesis II calls for stimulating convection at radii outward from the region of maximum winds. This region of increased convection then competes with the eyewall region for the air inflowing at low levels. The result should be a reduced prominence of the eyewall region, reduced temperature and pressure gradients in the eyewall region, and thus reduced maximum wind speeds. The results of the experiment on Hurricane Debbie for August 18, 1969, strongly suggest that all of these events occurred at least through the period of the first three seeding runs. That is, the reduction in temperature over the central region and its slight increase at larger radii indicate that some portion of the inflowing low-level air, which normally drives the storm's transverse circulation through the eyewall region, was being intercepted at larger radii. Also there was some evidence of increased convection during the early portion of the seeding operation. After the third seeding, the small and intermediate scale features became much more diffuse, suggesting a possible merging of the smaller scale features.

The reduction in the large-scale feature that occurred on August 18, 1969, was not predicted by either Hypothesis I or Hypothesis II. In fact, calculations of the expected decrease in maximum winds were about 10 to 15 percent, but the actual reduction in maximum winds was about 30 percent. These results imply that the seeding effects were being superimposed on a large-scale change that was occurring naturally.

5. ANALYSIS OF HURRICANE DEBBIE - AUGUST 20, 1969

The method of analysis described in section 2 is applied to data collected in Hurricane Debbie on August 20, 1969. This is the same scheme and parameters as used in the previous section. They are presented similar to section 4, except that these data were collected on August 20, 1969. More data were obtained during the August 20 operation than during the August 18 experiment, and the seeding operation began approximately 2 hours earlier than on the 18th. These differences occurred primarily because the storm was nearer the base of operations on August 20 than on August 18 (fig. 1).

5.1 Kinetic Energy

The kinetic energy profiles obtained by applying filters "A", "B", and "C" to the observed data are shown in figures 37 and 38. The double maxima structure is quite evident in all quadrants before the seeding

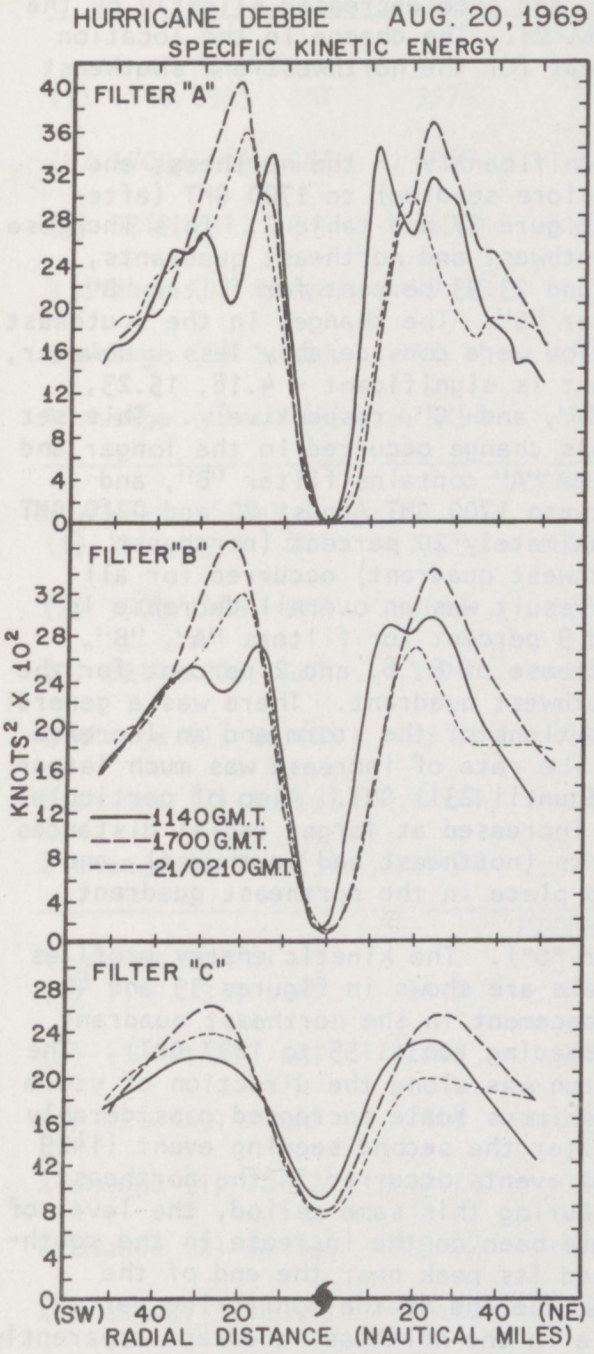

Figure 37. Kinetic energy profiles for the SW-NE quadrants of the storm.

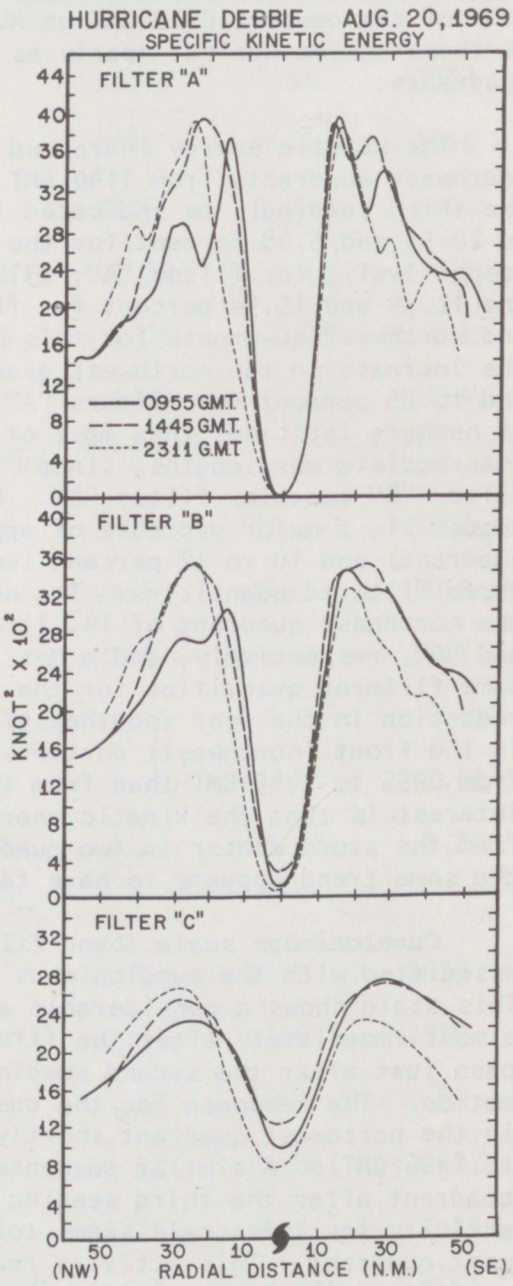

Figure 38. Kinetic energy profiles for the NW-SW quadrants of the storm.

runs, as shown in the profiles obtained by application of filter "A". The prominence of this double structure reduced considerably by the time of the intermediate pass and disappeared by the time of the final profile for each quadrant. Also quite evident is that in the northeast and southwest quadrants the radius of these maxima increased by more than 10 n miles between 1140 and 1700 GMT, and then decreased slightly by the time of the pass at 0210 GMT on August 21. The change in the location of these maxima was not nearly as great for the northwest and southeast quadrants.

The kinetic energy increased significantly in the northeast and southwest quadrants from 1140 GMT (before seeding) to 1700 GMT (after the third seeding), as indicated in figure 37 and table 2. This increase is 20.59 and 5.48 percent for the southwest and northeast quadrants, respectively, for filter "A"; 23.28 and 23.93 percent for filter "B"; and 12.34 and 15.54 percent for filter "C". The changes in the southeast and northwest quadrants for this period were considerably less. However, the increase in the northwest quadrant is significant - 4.18, 15.23, and 10.86 percent for filters "A", "B", and "C", respectively. This set of numbers indicates that most of this change occurred in the longer and intermediate wavelengths, since filter "A" contains filter "B", and filter "B" contains filter "C". Between 1700 GMT August 20 and 0210 GMT August 21, a major decrease of approximately 20 percent (northeast quadrant) and 10 to 12 percent (southwest quadrant) occurred for all three filtered quantities. The net result was an overall decrease in the northeast quadrant of 14, 1, and 9 percent for filters "A", "B", and "C", respectively, and a net increase of 6, 8, and 2 percent for the same filtered quantities for the southwest quadrant. There was a general reduction in the rear (southeast) portions of the storm and an increase in the front (northwest) portions. The rate of increase was much larger from 0955 to 1445 GMT than from 1445 until 2311 GMT. Also of particular interest is that the kinetic energy increased at larger radial distances from the storm center in two quadrants (northwest and southwest), and the same trend appears to have taken place in the northeast quadrant.

Cumulonimbus scale (band filter "D"). The kinetic energy profiles associated with the cumulonimbus scale are shown in figures 39 and 40. This scale shows a considerable enhancement in the northeast quadrant almost immediately after the first seeding run (1155 to 1237 GMT). The pass just after the second seeding run was along the direction of storm motion. The response for the cumulonimbus scale increased considerably in the northwest quadrant shortly after the second seeding event (1429 to 1456 GMT). A similar sequence of events occurred in the northeast quadrant after the third seeding. During this same period, the level of activity for this scale seems to have been on the increase in the southwest quadrant. This activity reached its peak near the end of the seeding period, and subsided through the end of the monitoring period. The level of activity for this scale in the northeast quadrant apparently reached its peak earlier and then decreased nearly through the end of the monitoring period. However, the final two passes through this area, which occurred some 5 to 6 hours after the final seeding run, indicate that the level of activity was increasing. These same profiles for the

Table 2. Maximum Specific Kinetic Energy (kt^2) and Percent Changes for Hurricane Debbie on August 20, 1969

OBS TIME	QUADRANT SW	NE	SE	NW	NET
		FILTER "A"			
(SW-NE/SE-NW)					
(1) 1140/0955 GMT	3374	3448	3931	3755	3931
(2) 1700/1445 GMT	4069	3637	3863	3912	4069
(3) 0210/2311 GMT	3576	2959	3822	3902	3902
% change (1) to (2)	+20.59	+ 5.48	- 1.72	+ 4.18	+ 3.51
% change (2) to (3)	-12.11	-18.64	- 1.06	- 0.25	- 4.10
% change (1) to (3)	+ 5.98	-14.18	- 2.77	+ 3.91	- 0.73
		FILTER "B"			
(SW-NE/SE-NW)					
(1) 1140/0955 GMT	2929	2691	3378	3033	3378
(2) 1700/1445 GMT	3611	3335	3452	3495	3611
(3) 0210/2311 GMT	3170	2666	3268	3521	3521
% change (1) to (2)	+23.28	+23.93	+ 2.19	+15.23	+ 6.89
% change (2) to (3)	-12.21	-20.05	- 5.33	+ 0.74	- 2.49
% change (1) to (3)	+ 8.22	- 0.92	- 3.25	+16.08	+ 4.23
		FILTER "C"			
(SW-NE/SE-NW)					
(1) 1140/0955 GMT	2317	2162	2699	2300	2699
(2) 1700/1445 GMT	2603	2498	2720	2550	2720
(3) 0210/2311 GMT	2368	1973	2306	2660	2660
% change (1) to (2)	+12.34	+15.54	+ 0.77	+10.86	+ 0.77
% change (2) to (3)	- 9.02	-21.01	-15.22	+ 4.31	- 2.20
% change (1) to (3)	+ 2.20	- 8.74	-14.56	+15.65	- 1.44

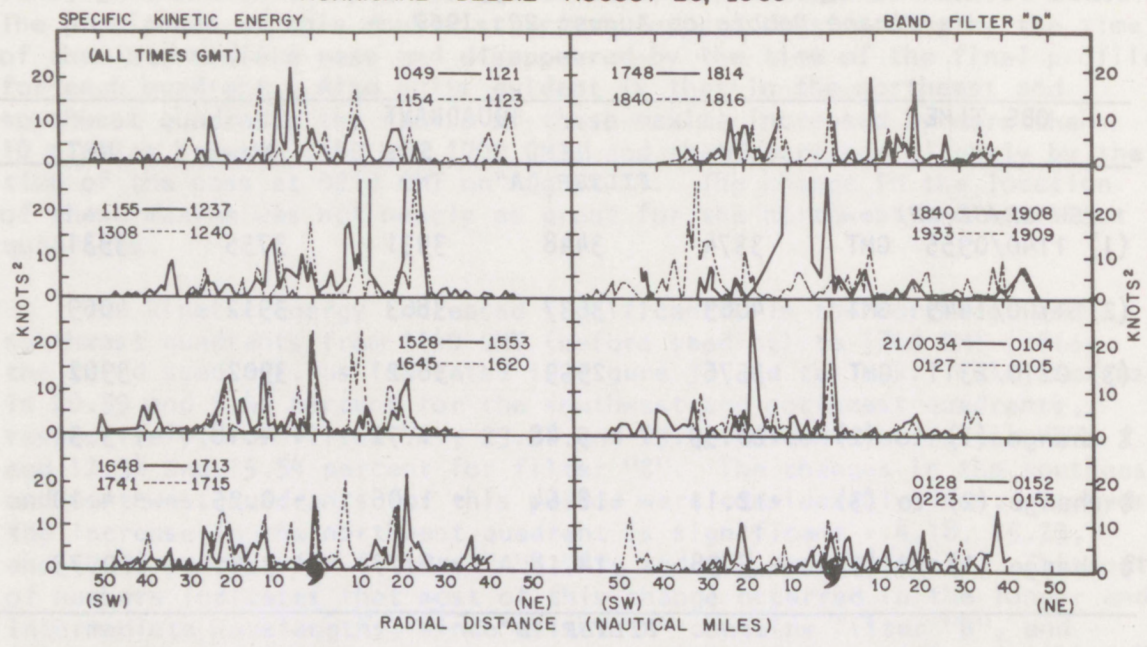

Figure 39. Kinetic energy profiles for the SW-NE quadrants of the storm (~cumulonimbus scale).

northwest and southeast quadrants covering some 3 to 4 hours after the final seeding period indicate a high level of activity in the southeast quadrant for this scale, but with almost no response in the northwest quadrant.

The wind speed variability profiles for approximate cumulonimbus scale motion (VARIB W1) show a considerable increase in the northeast quadrant just after the first seeding run (fig. 41). This response level then decreased after the seeding. (Compare the profile for 1155 to 1235 GMT with that for 1240 to 1308 GMT.) The next two monitoring passes through this region occurred just before and shortly after the third seeding period. Again, in the northeast quadrant a significant increase took place after the seeding. A similar sequence occurred for the period surrounding the fourth seeding event (~1800 GMT). The peak response in

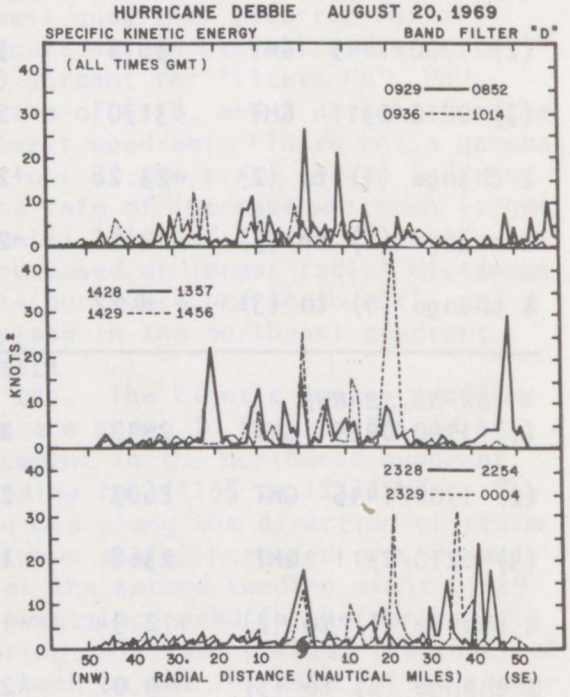

Figure 40. Kinetic energy profiles for the NW-SW quadrants of the storm (~cumulonimbus scale).

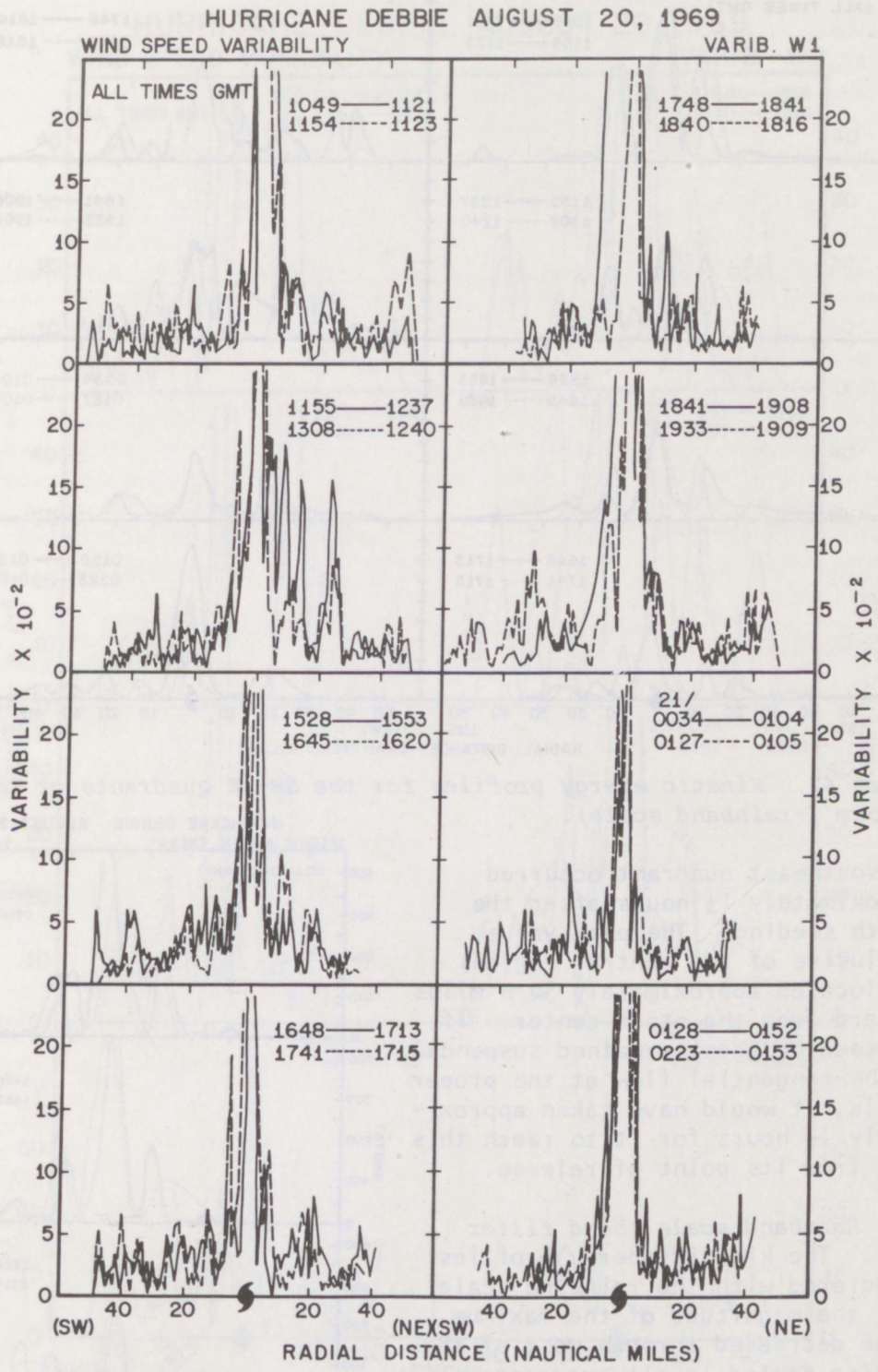

Figure 41. Relative wind speed variability profiles for approximate cumulus scale motion (VARIB W1).

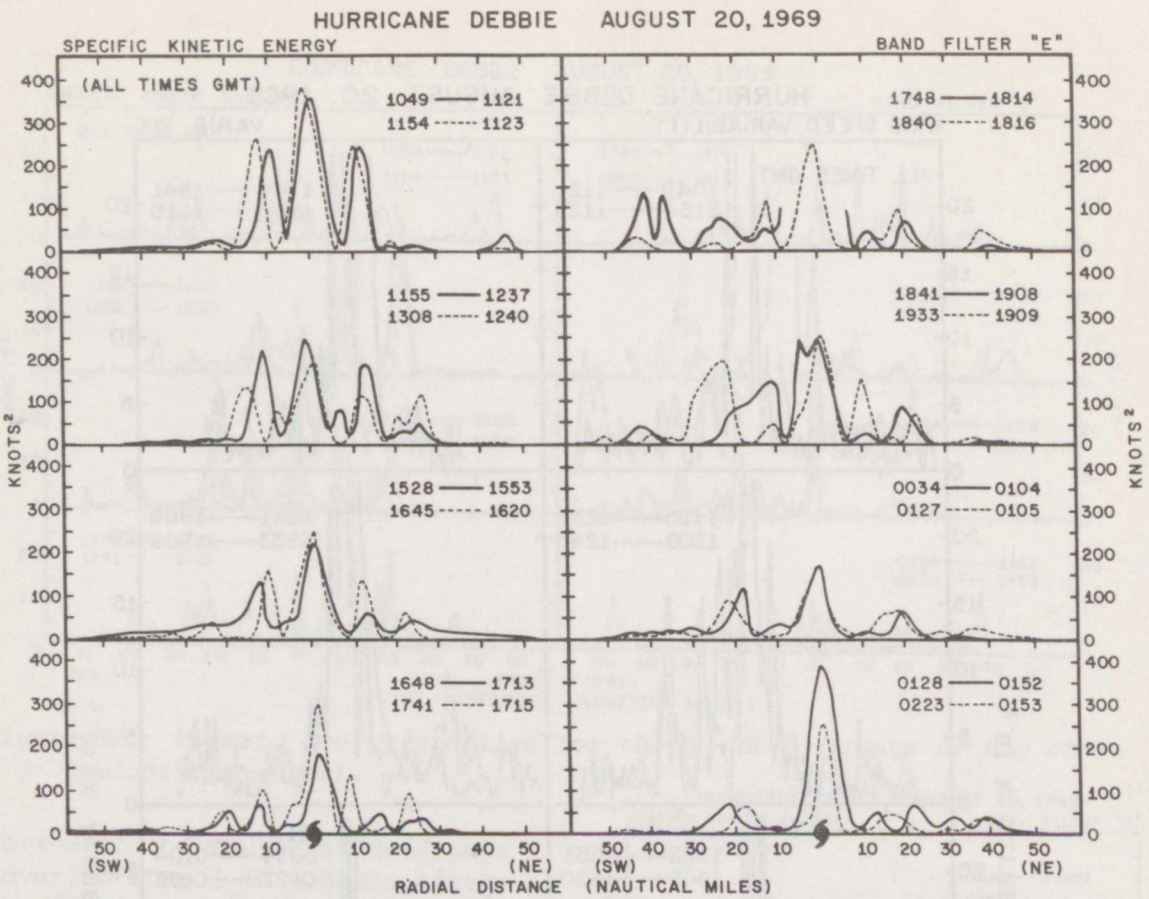

Figure 42. Kinetic energy profiles for the SW-NE quadrants of the storm (~rainband scale).

the southeast quadrant occurred approximately 1½ hours after the fourth seeding. The peak value (exclusive of the central region) was located approximately 30 n miles outward from the storm center. If the seeding agent remained suspended in the tangential flow at the proper levels, it would have taken approximately 1½ hours for it to reach this area from its point of release.

Rainband scale (band filter "E"). The kinetic energy profiles associated with the rainband scale show the magnitude of the maximum value decreased through most of the seeding period in all quadrants (figs. 42 and 43). This decline seemed to be quite steady through the first 6 hours of the operation,

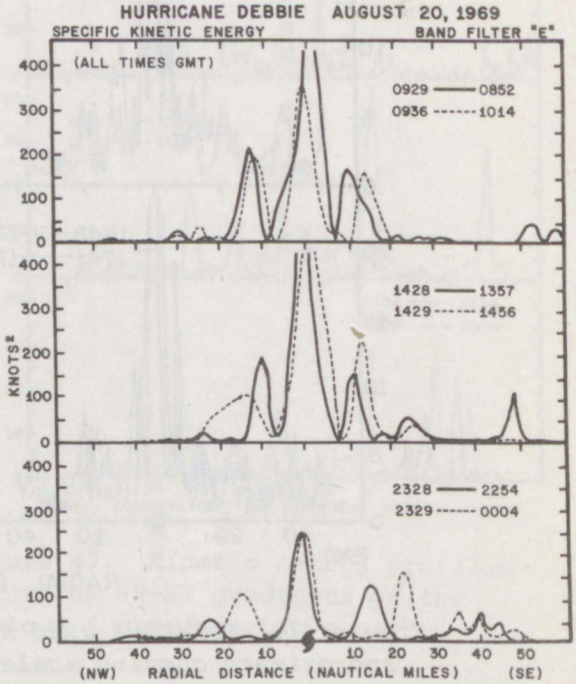

Figure 43. Kinetic energy profiles for the NW-SE quadrants of the storm (~eyewall scale).

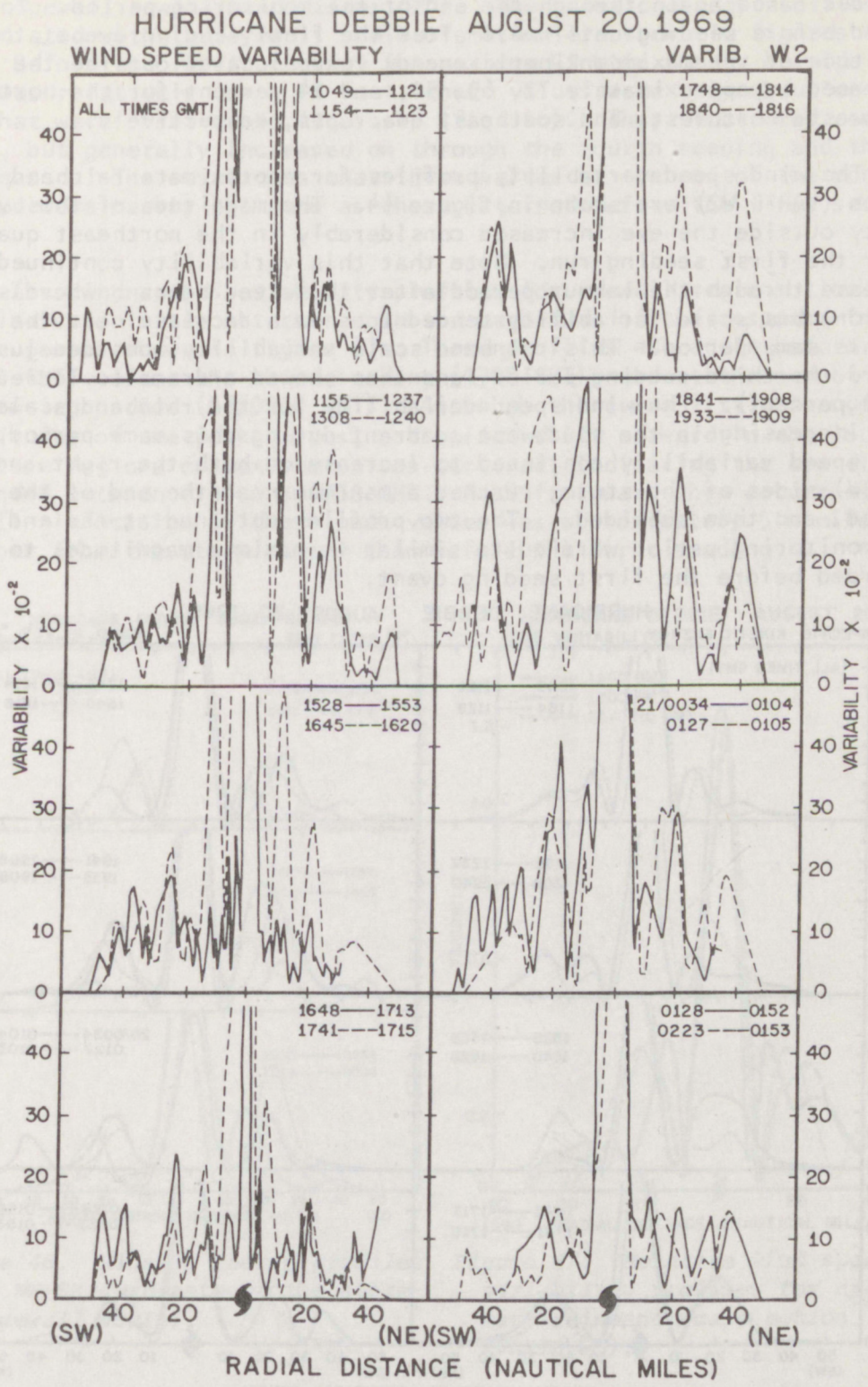

Figure 44. Relative wind speed variability profiles for approximate rainband scale motion (VARIB W2).

fluctuated somewhat between the fourth and fifth seeding events, and then decreased again through the end of the monitoring period. For the period before seeding until well after the final seeding event, the magnitude of the maximum kinetic energy value located outside the eye decreased by approximately 72, 69, 50, and 14 percent for the northeast, southwest, northwest, and southeast quadrants, respectively.

The wind speed variability profiles for approximate rainband scale motion (VARIB W2) are shown in figure 44. The magnitude of this variability outside the eye increased considerably in the northeast quadrant after the first seeding run. Note that this variability continued to increase through the 1 hour period after this seeding run, whereas the cumulonimbus scale variability tended to show a decrease near the end of this same period. This rainband scale variability subsided just before the third seeding period, and then showed a dramatic increase (~300 percent). The wind speed variability for the rainband scale was also increasing in the southwest quadrant during this same period. The wind speed variability continued to increase on both the right and left (NE-SW) sides of the storm, reached a maximum near the end of the seeding period, and then subsided. The two profiles obtained at the end of the monitoring period were quite similar in maximum magnitudes to those recorded before the first seeding event.

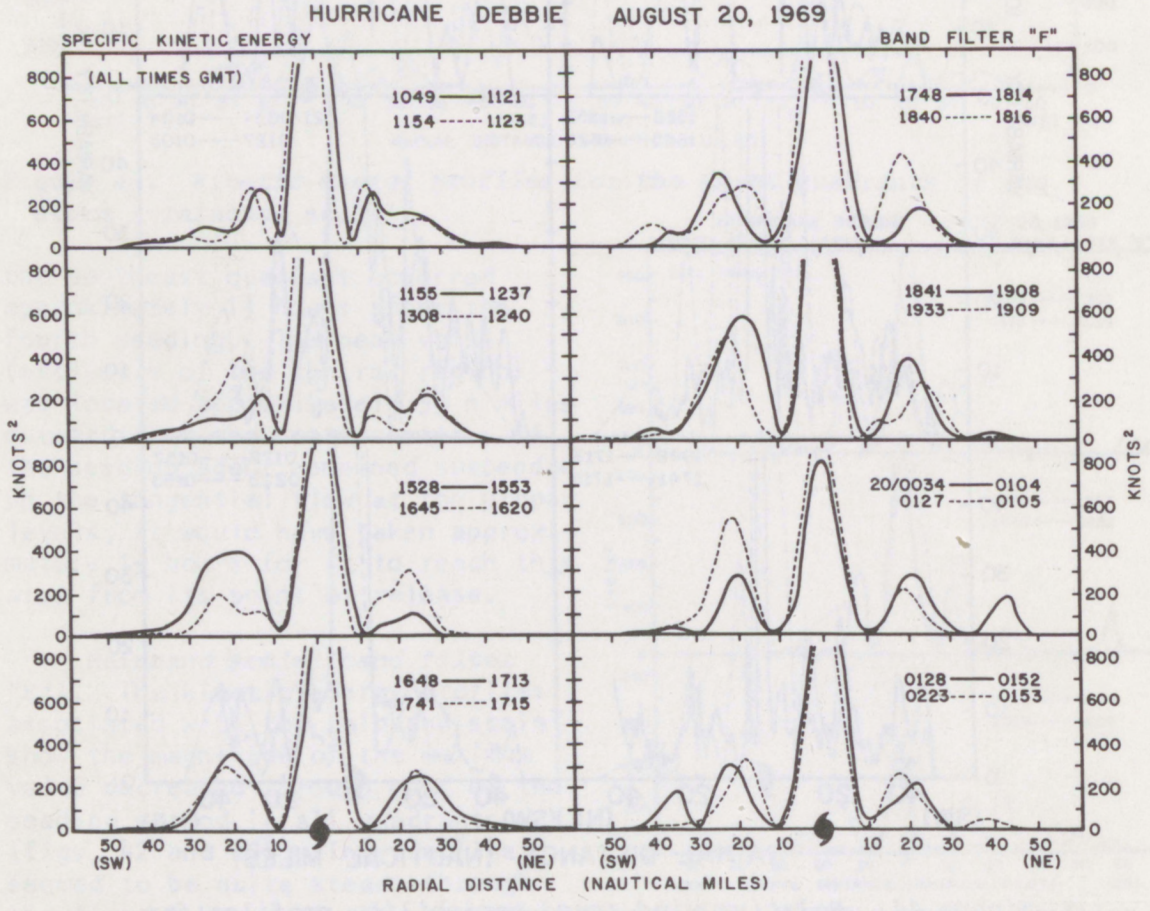

Figure 45. Kinetic energy profiles for SW-NE quadrants of the storm (~eyewall scale).

Eyewall scale (band filter "F"). The kinetic energy profiles associated with the eyewall scale of motion are shown in figures 45 and 46. Before the first seeding, the maximum kinetic energy outside the eye was relatively low. In fact, these values were only about one-half of what were observed on August 18 (fig. 16). They fluctuated considerably, but generally increased on through the fourth seeding and then decreased. The result was that these values at the end of the monitoring period were nearly the same as those obtained before the first seeding run.

The wind speed variability profiles for eyewall scale motion (VARIB W3) indicate little net change in the magnitude of the response for the three passes shown in figure 47. These profiles are again before seeding (1140 GMT), after the third seeding (1700 GMT), and at the end of the monitoring period (21/0210 GMT). Although there was little change in the magnitudes of the peak values, a distinct shift outward in the location of these regions of maximum values occurred, indicating the eye diameter expanded between 1140 and 1700 GMT. A shift inward then occurred, but the final location of these peak values was approximately 5 n miles farther from the storm center than before the first seeding.

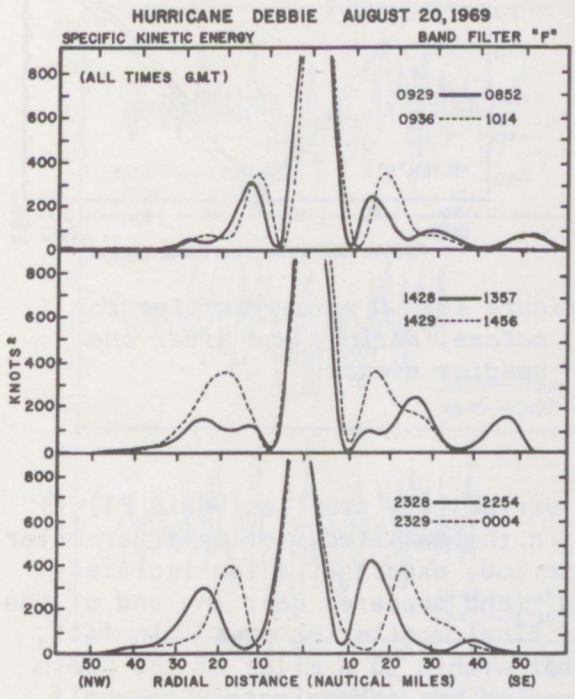

Figure 46. Kinetic energy profiles for NW-SE quadrants of the storm (~eyewall scale).

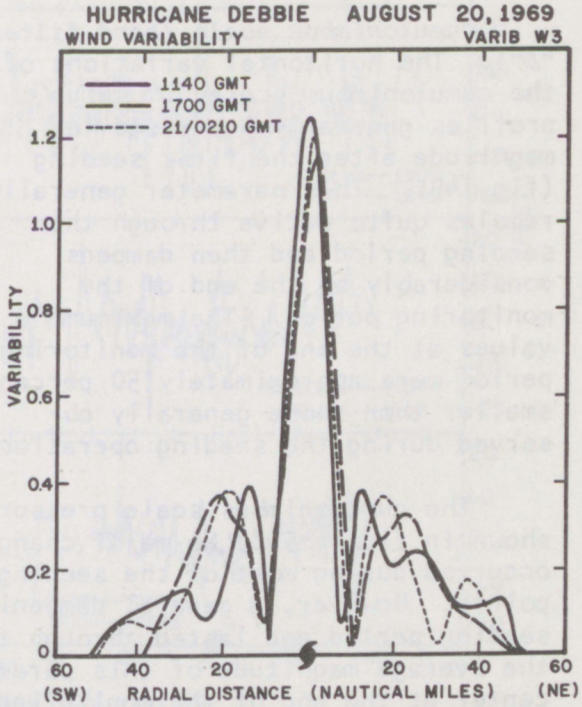

Figure 47. Relative wind speed variability profiles for approximate rainband scale motion (VARIB W3).

5.2 Pressure

The minimum value of the filtered "D" values increased between the third seeding and the final monitoring pass of the day (fig. 48). Approximately one-half of this increase took place in the long wavelengths with most of the remainder occurring in the rainband to eyewall scale of motion. Although the central pressure was steady through the first 6 hours of the experiment for the sum of the long and intermediate wavelengths (filters "A" and "B"), the long wavelength features (filter "C") decreased. This, of course, implies that an increase in pressure must have been occurring in the intermediate wavelengths.

Cumulonimbus scale (band filter "D"). The horizontal variations of the cumulonimbus scale "D" value profiles generally increased in magnitude after the first seeding (fig. 49). This parameter generally remains quite active through the seeding period and then dampens considerably by the end of the monitoring period. The maximum values at the end of the monitoring period were approximately 50 percent smaller than those generally observed during the seeding operation.

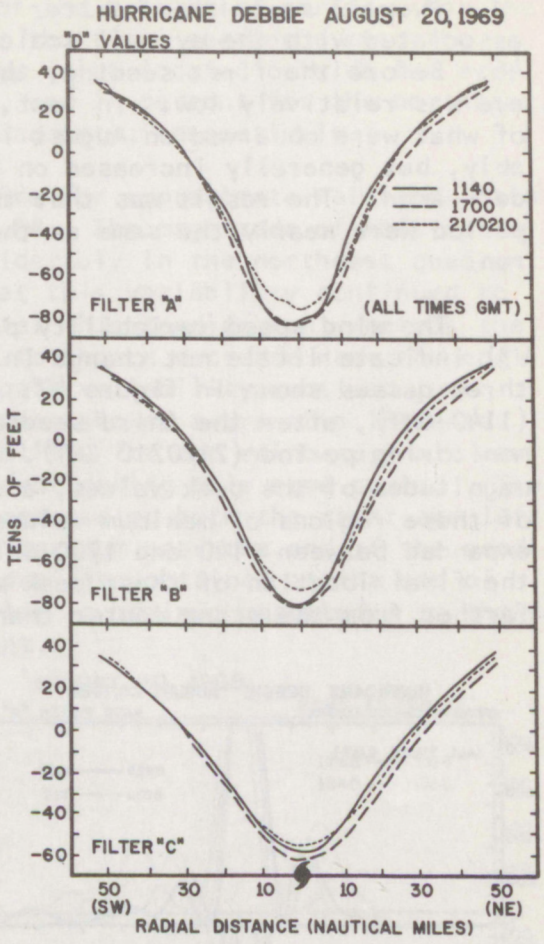

Figure 48. D value profiles for before, during, and after the seeding events.

The cumulonimbus scale pressure variability profile (VARIB P1) is shown in figure 50. No major change in the magnitudes of this parameter occurred during most of the seeding period, except at a few isolated points. However, a general dampening trend appeared near the end of the seeding period and lasted through the final monitoring pass. In fact, the average magnitude of this parameter within 30 n miles of the storm center at the end of the monitoring period was approximately one-half of that recorded before the first seeding period.

Rainband scale (band filter "E"). The rainband scale "D" value profiles show a distinct decrease in the pressure gradients, particularly in the eyewall region (fig. 51). Most of this pressure change occurred before the fourth seeding period; however, the final profile is much smoother than either of the two recorded earlier. Also, the maximum amplitude of the curve obtained on the last monitoring pass is 40 percent smaller than that recorded before seeding.

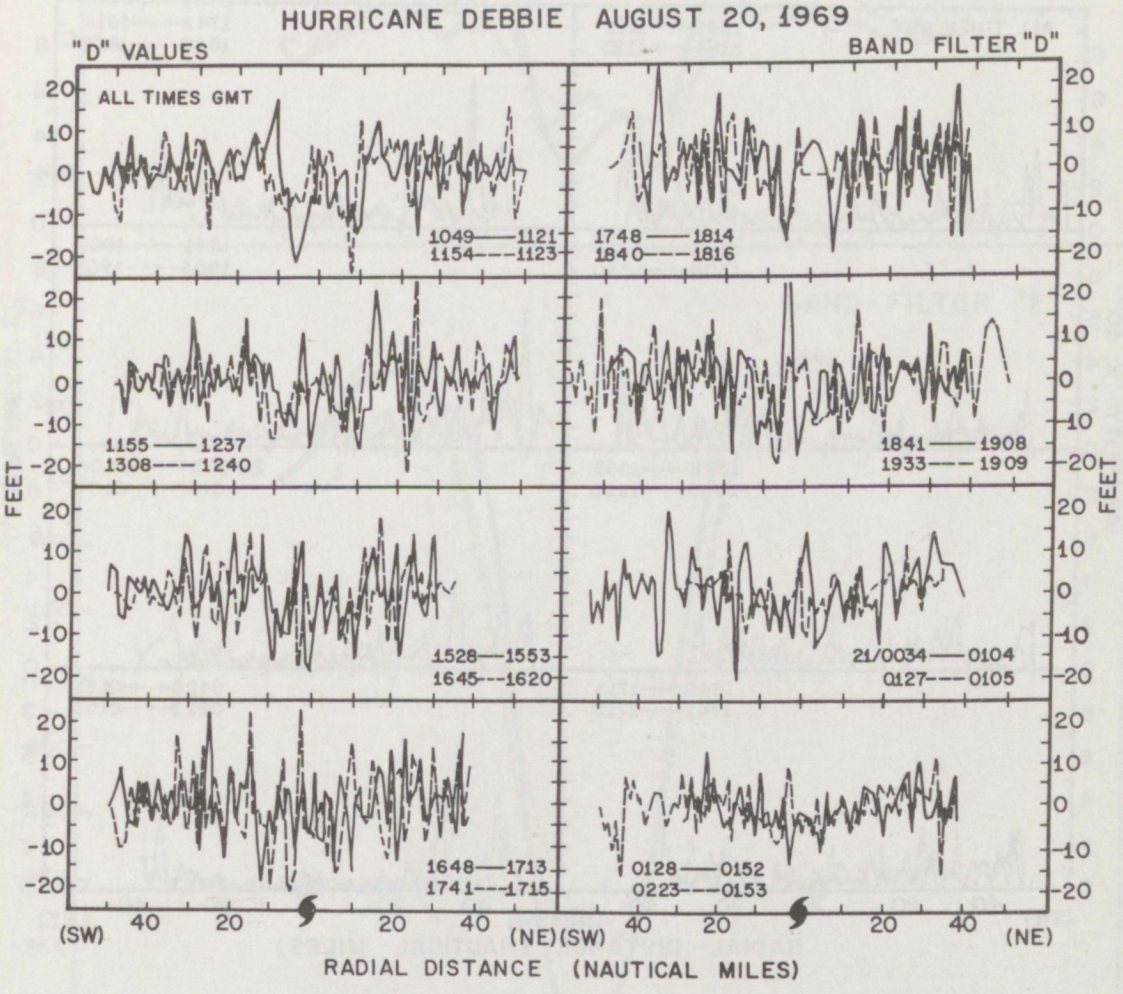

Figure 49. D value profiles (~cumulonimbus scale) of the observed data.

The rainband scale pressure variability profiles (VARIB P2) are shown in figure 52. Although considerable horizontal and time variations existed in this parameter, it is difficult to determine any significant trend. The average amplitude of the profiles, except for a few select points, remained nearly the same through most of the monitoring period.

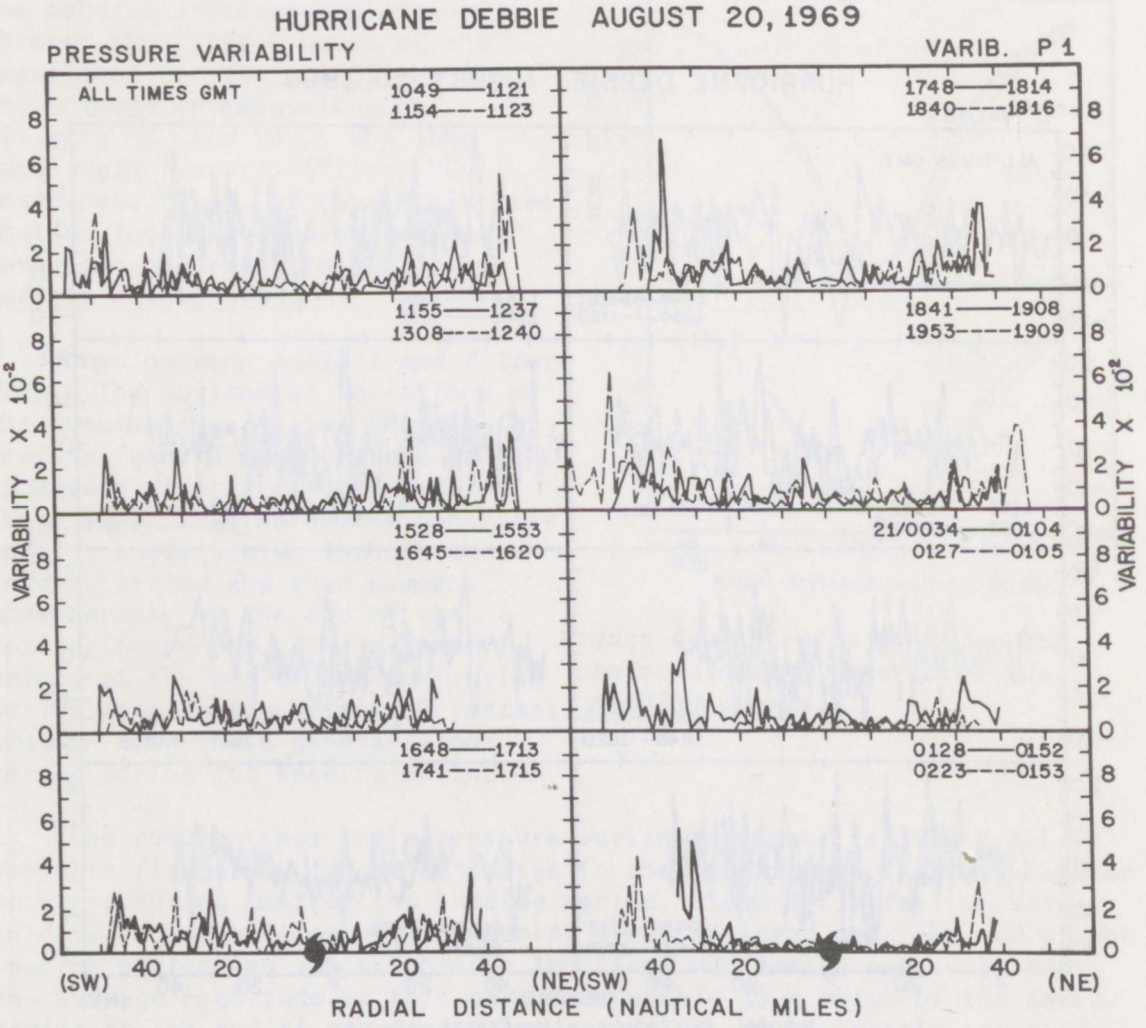

Figure 50. Pressure variability profiles for approximate cumulonimbus scale.

Eyewall scale (band filter "F"). During the seeding operation, the eyewall scale "D" value profiles also decreased in amplitude and pressure gradient in the eyewall region (fig. 51). Again, a major portion of this change took place before the fourth seeding, but a significant amount occurred between the fourth seeding and the final monitoring pass.

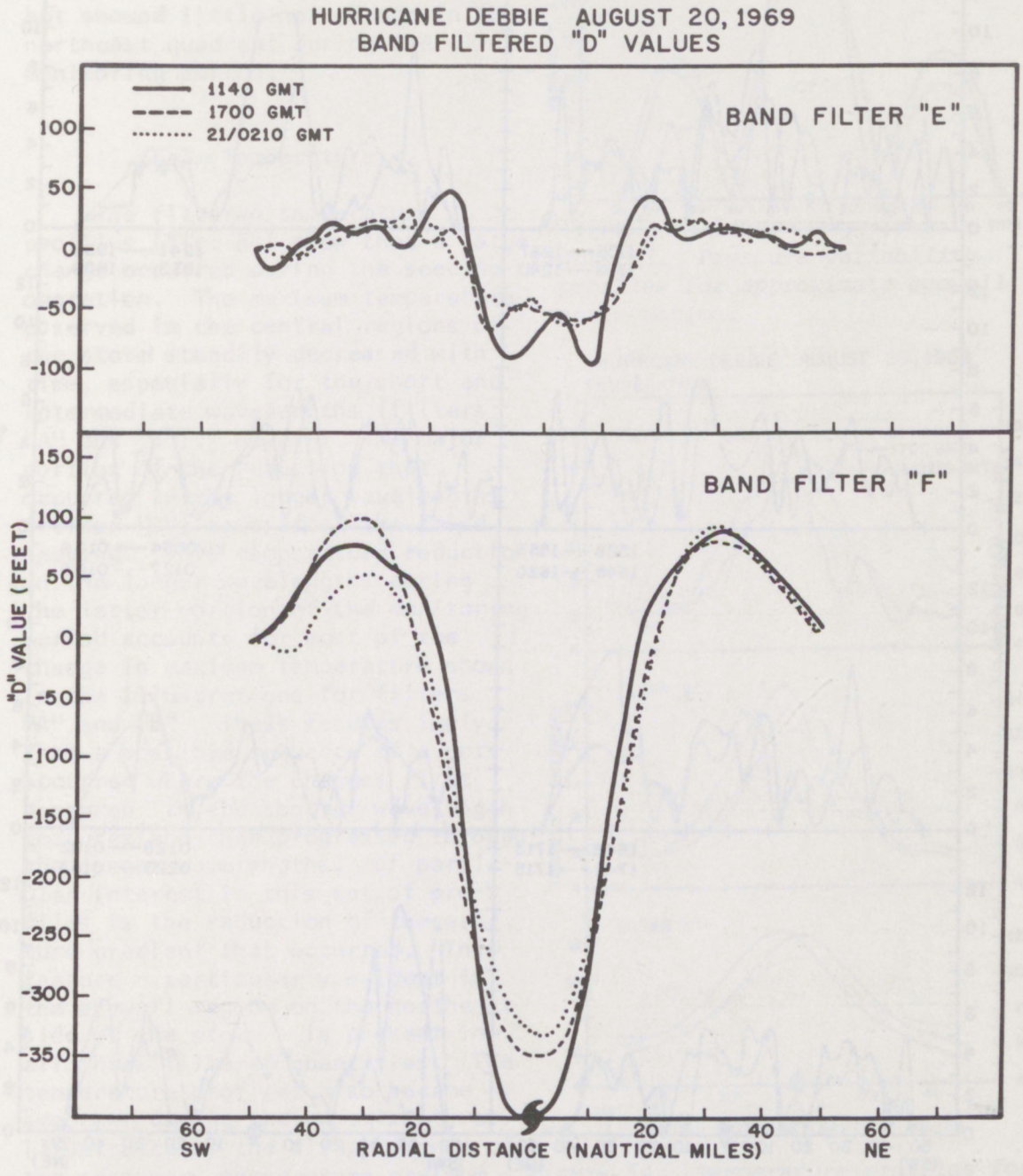

Figure 51. D value profiles (~rainband and eyewall scales) of the observed data.

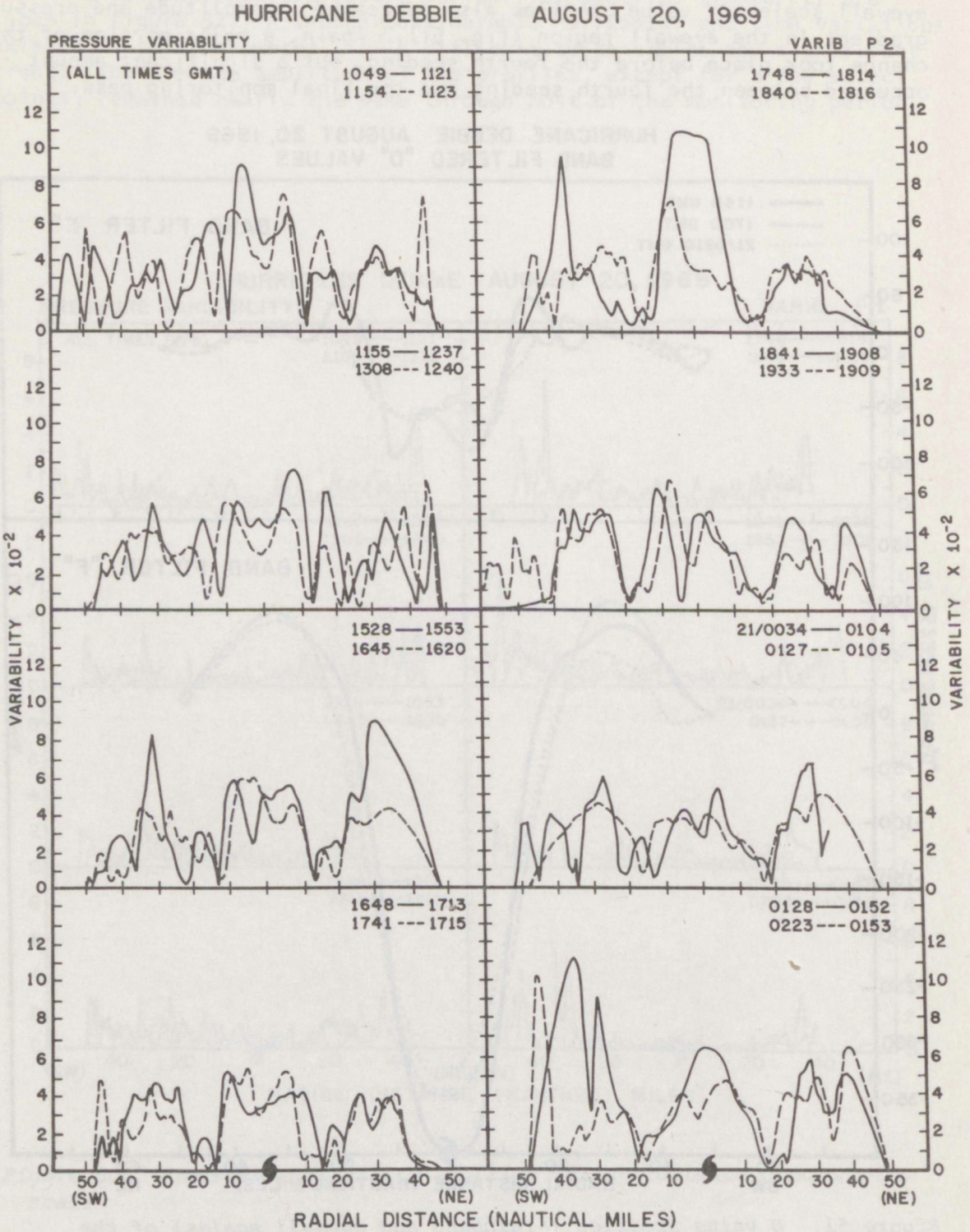

Figure 52. Pressure variability profiles for approximate rainband scale motion.

The eyewall scale pressure variability profiles (VARIB P3), however, exhibited distinct changes (fig. 53). The magnitude of this parameter decreased by about 50 percent in the southwest quadrant, but showed little net change in the northeast quadrant during the monitoring period.

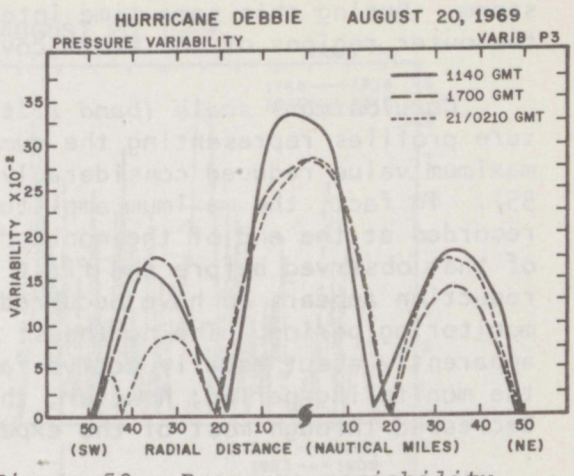

Figure 53. Pressure variability profiles for approximate eyewall scale motion.

5.3 Temperature

The filtered temperature profiles (fig. 54) show that a large change occurred during the seeding operation. The maximum temperature observed in the central regions of the storm steadily decreased with time, especially for the short and intermediate wavelengths (filters "A" and "B"). However, the major portion of the reduction that occurred in the longer wavelengths (filter "C") came after the third seeding. This temperature reduction in the longer wavelengths during the latter portion of the monitoring period accounts for most of the change in maximum temperature shown in the illustrations for filters "A" and "B". These results imply that a possible sequence of events occurred where the changes first appeared in the shorter wavelength features and then progressed through the longer wavelengths. Of particular interest in this set of profiles is the reduction of temperature gradient that occurred. This feature - particularly evident in the eyewall region on the northeast side of the storm - is present in all three filtered quantities. The temperature profiles also became smoother during the experiment, as illustrated by the disappearance of the secondary temperature maximum located on the northeast side of the

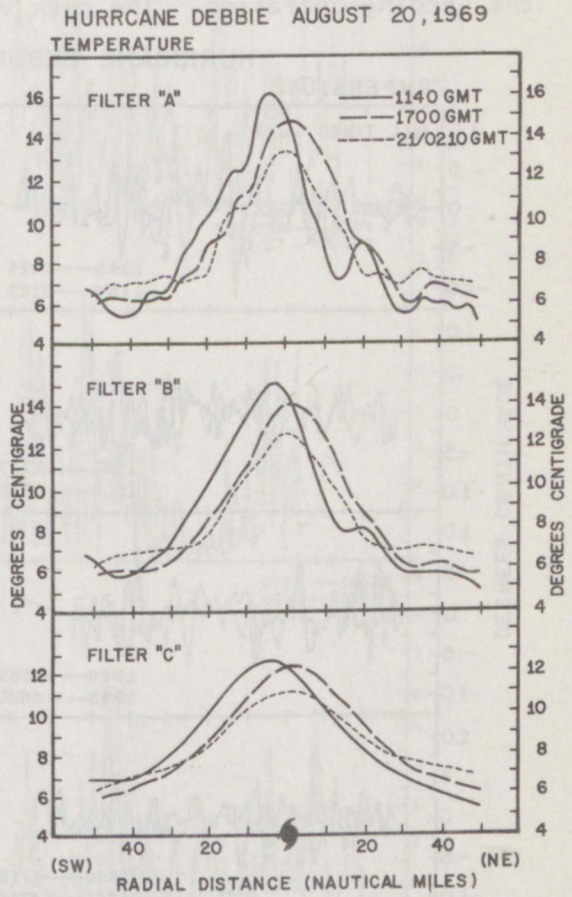

Figure 54. Temperature profiles for before, during, and after the seeding events.

storm. During this same time interval, the temperature increased in the outer regions of the storm covered by the monitoring pattern.

Cumulonimbus scale (band filter "D"). The time sequence of temperature profiles representing the cumulonimbus scale indicates that the maximum value reduced considerably during the monitoring period (fig. 55). In fact, the maximum amplitude of the curves for the temperatures recorded at the end of the monitoring period is less than one-half of that observed before the first seeding. The largest portion of this reduction appears to have occurred during the early portion of the monitoring period. The northeast and southwest sides of the storm were apparently about equally active for this scale of motion during most of the monitoring period; however, the general trend of maximum values decreased through most of the experiment.

The cumulonimbus scale temperature variability profiles (VARIB T1) for the left and right sides of the storm (SW-NE) are shown in figure 56. The maximum magnitudes of this parameter fluctuated considerably during the seeding operation. The peak values on the southwest side of the

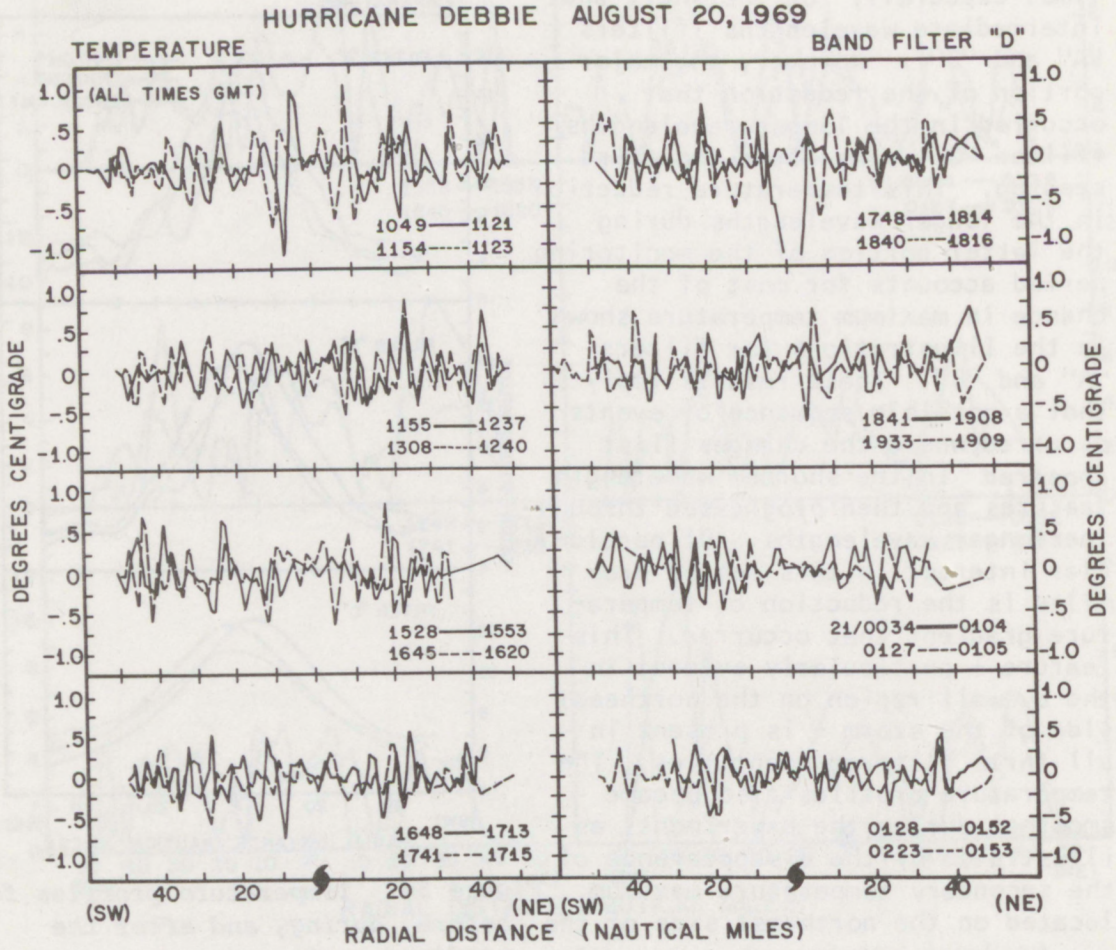

Figure 55. Temperature profiles (~cumulonimbus scale) for the observed data.

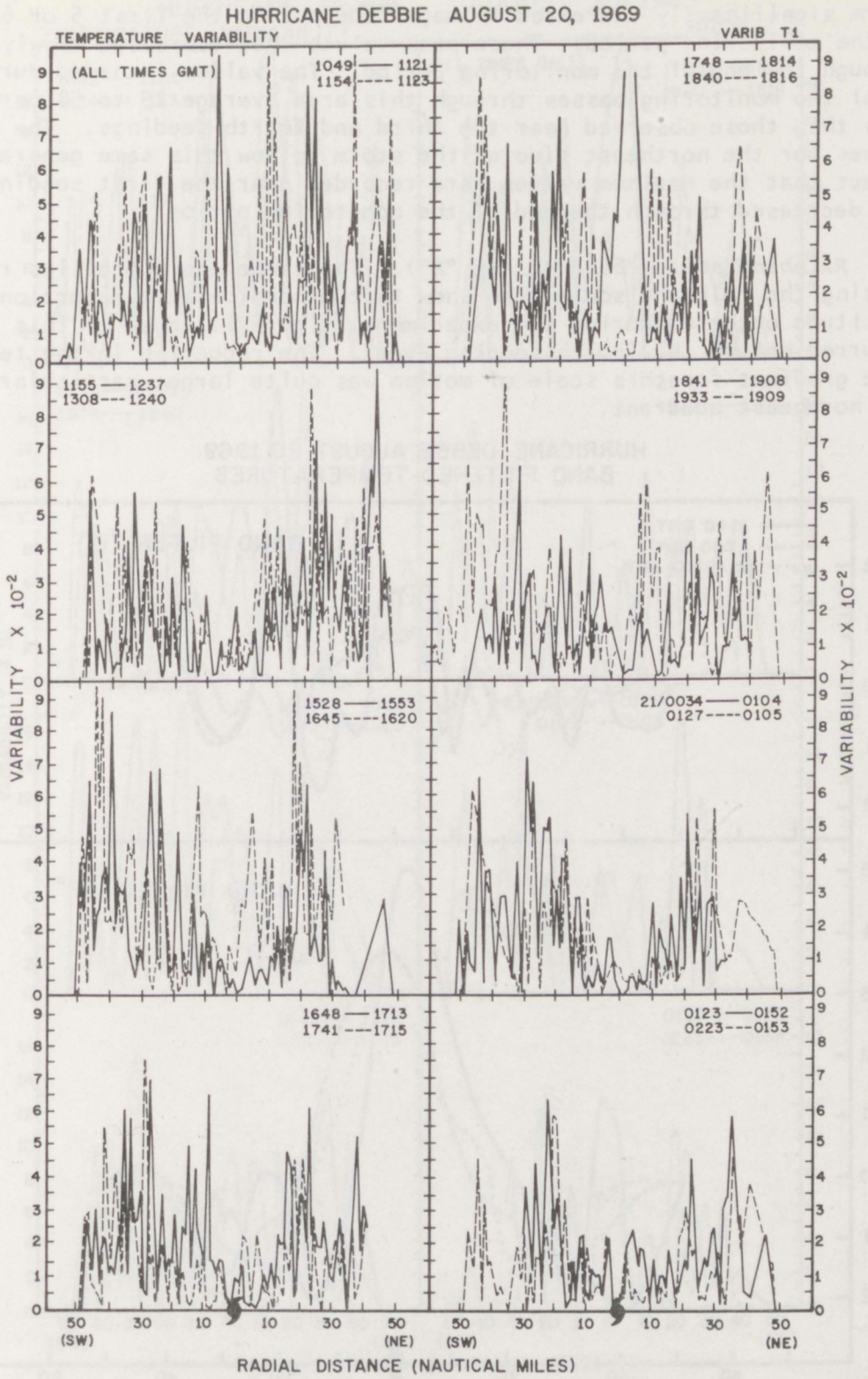

Figure 56. Temperature variability profiles for approximate cumulonimbus scale motion.

storm significantly increased in magnitude during the first 5 or 6 hours of the monitoring period. These peak values then decreased slowly through the end of the monitoring period. The values recorded during the final two monitoring passes through this area average 25 to 50 percent less than those observed near the third and fourth seedings. The peak values for the northeast side of the storm follow this same general trend, except that the maximum values were recorded near the first seeding run and decreased through the end of the monitoring period.

Rainband scale (band filter "E"). The temperature profiles representing the rainband scale also show that a considerable reduction in amplitude occurred during the experiment (fig. 57). Most of this change occurred before the fourth seeding event. The reduction in the temperature gradient for this scale of motion was quite large, particularly in the northeast quadrant.

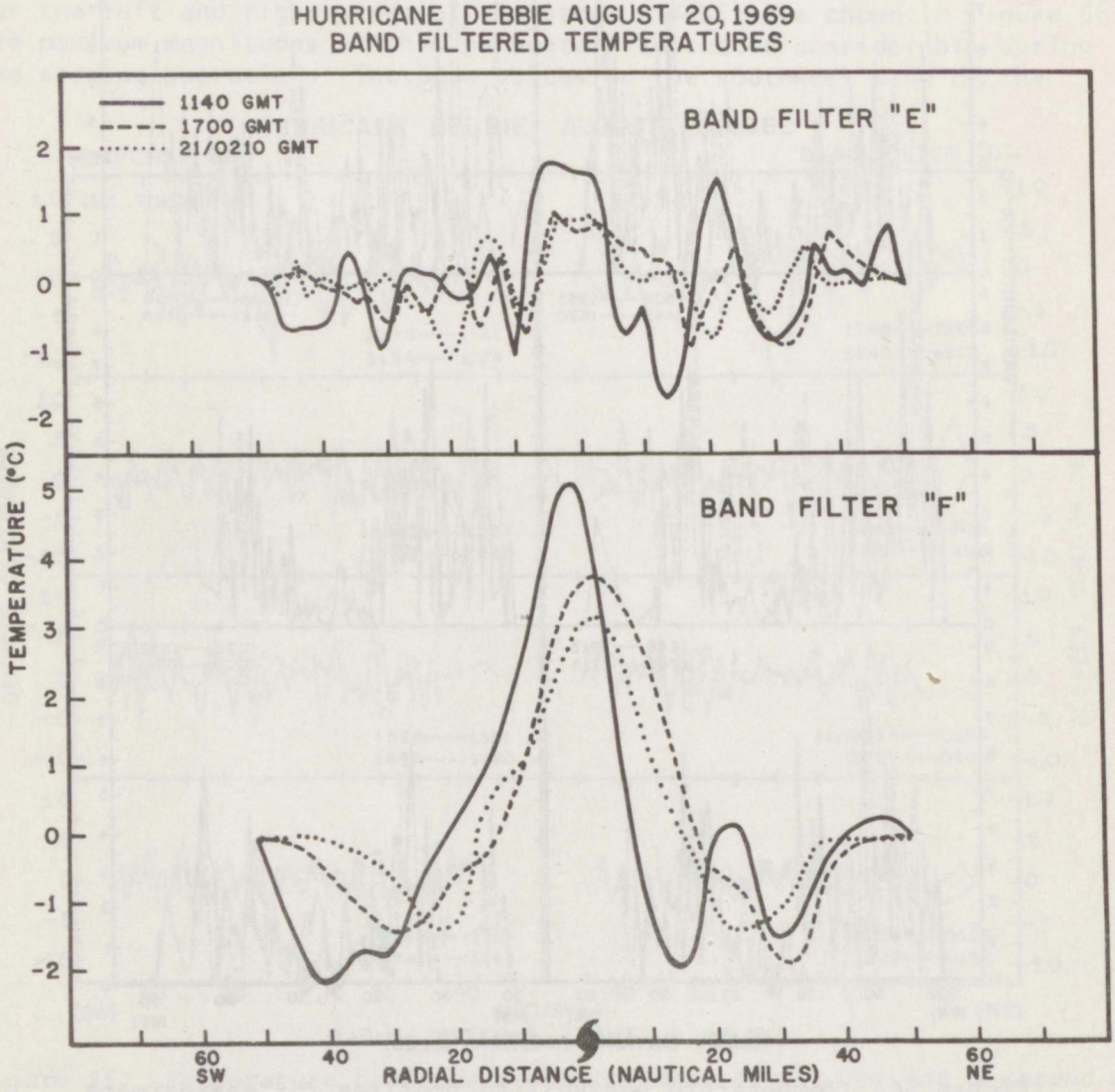

Figure 57. Temperature profiles (~rainband and eyewall scales) for the observed data.

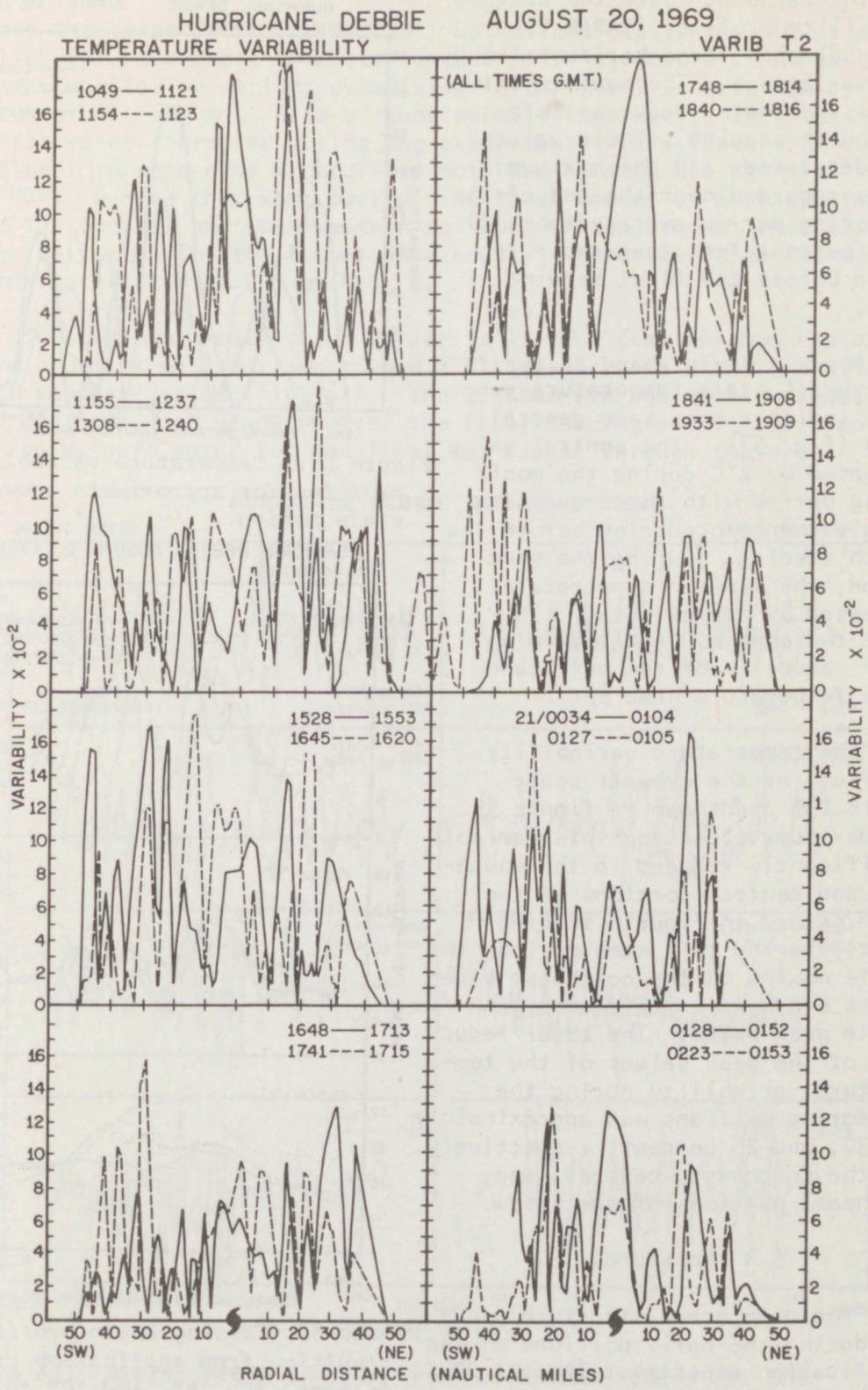

Figure 58. Temperature variability profiles for approximate rainband scale motion.

The rainband scale temperature variability profiles (VARIB T2) (fig. 58) show large horizontal and time variations. The maximum values of this parameter occurred before the fourth seeding. These values then decreased, and the maximum values recorded near the end of the monitoring period averaged some 20 to 50 percent less than those recorded before the first seeding event.

Eyewall scale (band filter "F"). The eyewall scale temperature profiles indicate this same general trend (fig. 57). The central value decreased by 2°C during the monitoring period with three-quarters of this change occurring before the fourth seeding. During the same period, the minimum temperatures increased by approximately 1°C. These two changes resulted in a major reduction of the hurricane scale temperature gradient.

The temperature variability profiles for the eyewall scale (VARIB T3) are shown in figure 59. The maximum values for this variable significantly reduced in the southwest and central portions of the storm before the fourth seeding event. During this same period, the double maxima on the northeast side of the storm were replaced by a single peak value. The total reduction of the peak values of the temperature variability during the monitoring missions was approximately 41, 30, and 25 percent, respectively, for the southwest, central, and northeast portions of the storm.

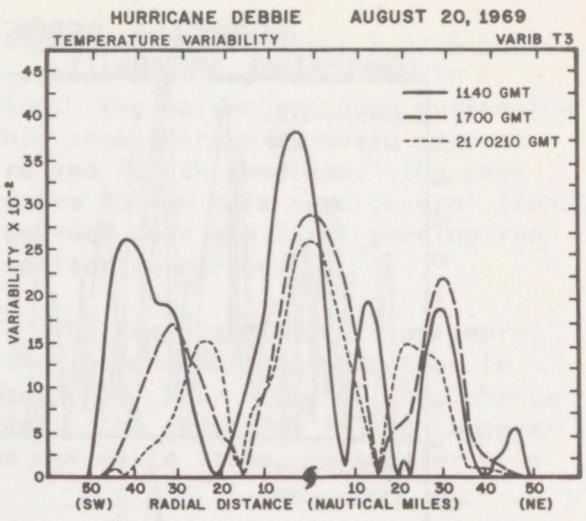

Figure 59. Temperature variability profiles for approximate eyewall scale motion.

5.4 Moisture

The double eye structure present during the early portions of the modification experiment (August 20, 1969), is quite evident in the moisture field analysis for this time (fig. 60). This feature was present

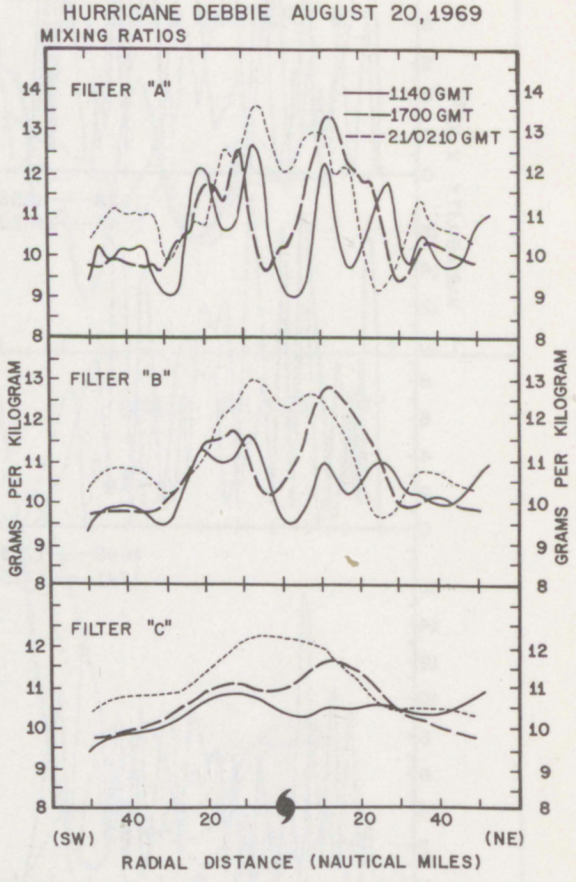

Figure 60. Mixing ratio profiles resulting from application of filters "A", "B", and "C" for before, during, and after the seeding events.

before the first seeding (1140 GMT) but became considerably less distinct by 1700 GMT. However, some semblance of this structure remained throughout the monitoring period, especially in the profiles obtained by application of filter "A". Also of considerable interest is that the minimum central value increased during the experiment. This feature is quite prominent in both sets of profiles obtained through use of filters "A" and "B". During this same period, the total amount of moisture increased over the central and southwestern portions of the storm. This was especially true for the longer wavelengths, where the value increased by approximately 1.0 to 1.5 gm/kg.

Cumulonimbus scale (band fitler "D"). The cumulonimbus scale mixing ratio profiles show a trend toward a slight decrease with time after the first seeding period (fig. 61). The minimum average amplitude was recorded some 4 to 5 hours after the final seeding event, and then larger amplitudes were noted for the final two passes through the area.

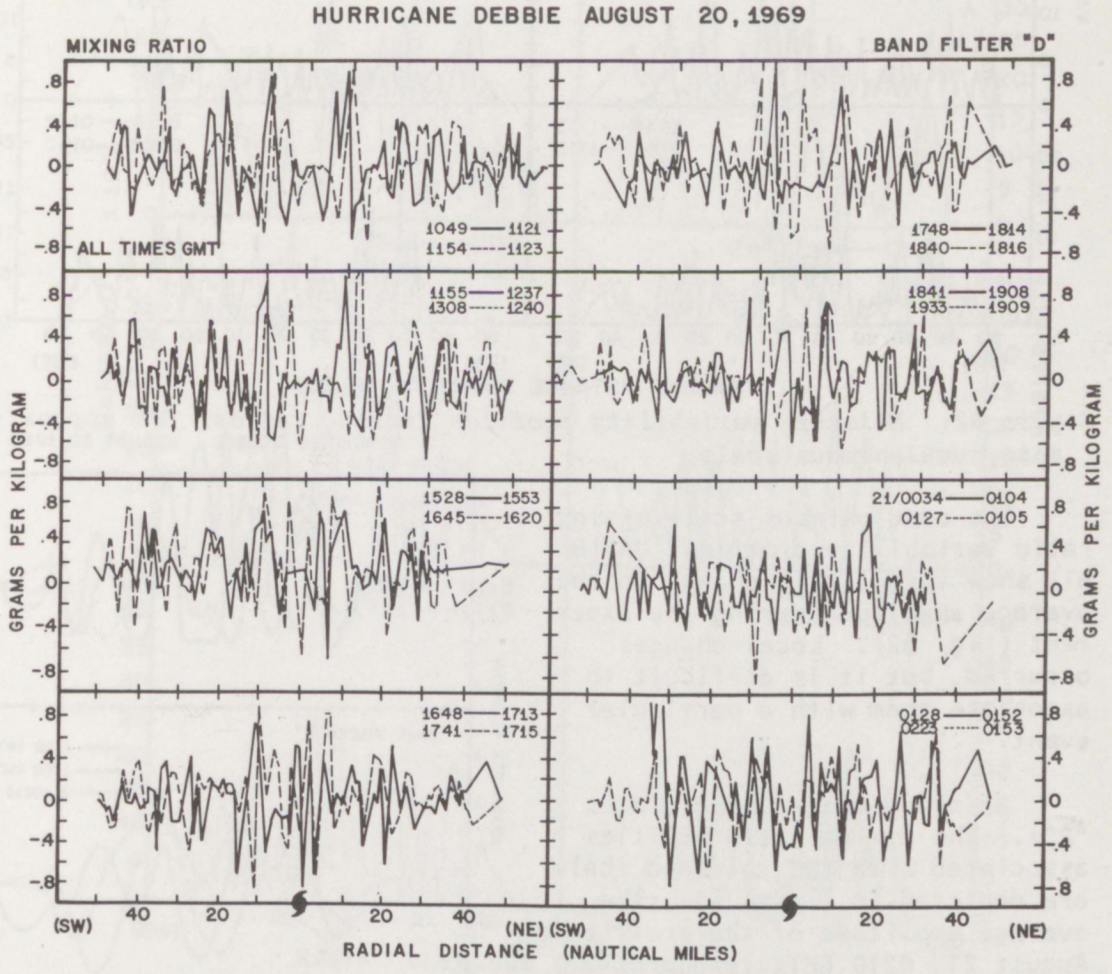

Figure 61. Mixing ratio profiles (~cumulonimbus scale) for the observed data.

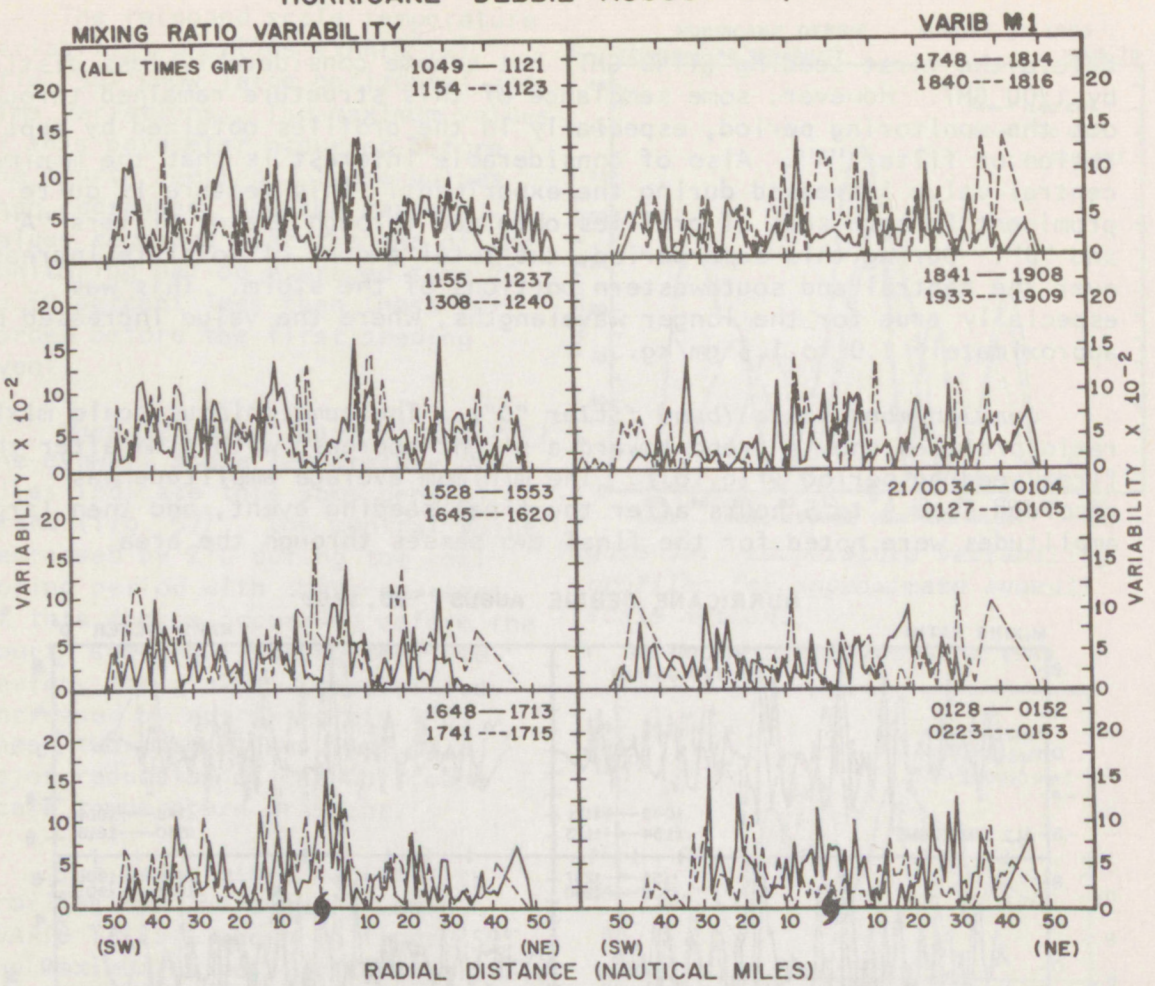

Figure 62. Moisture variability profiles (mixing ratios) for approximate cumulonimbus scale.

The cumulonimbus scale mixing ratio variability profiles (VARIB M1) show very little change in the average amplitude during the experiment (fig. 62). Local changes occurred, but it is difficult to associate them with a particular event.

Rainband scale (band filter "E"). The mixing ratio profiles associated with the rainband scale are depicted in figure 63. The average amplitude of the profile for August 21, 0210 GMT, is approximately one-half that recorded before the first seeding event.

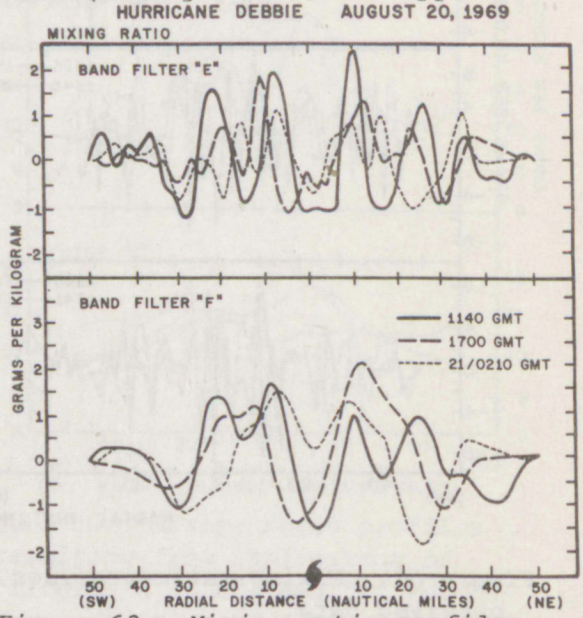

Figure 63. Mixing ratio profiles (~rainband and eyewall scales) for the observed data.

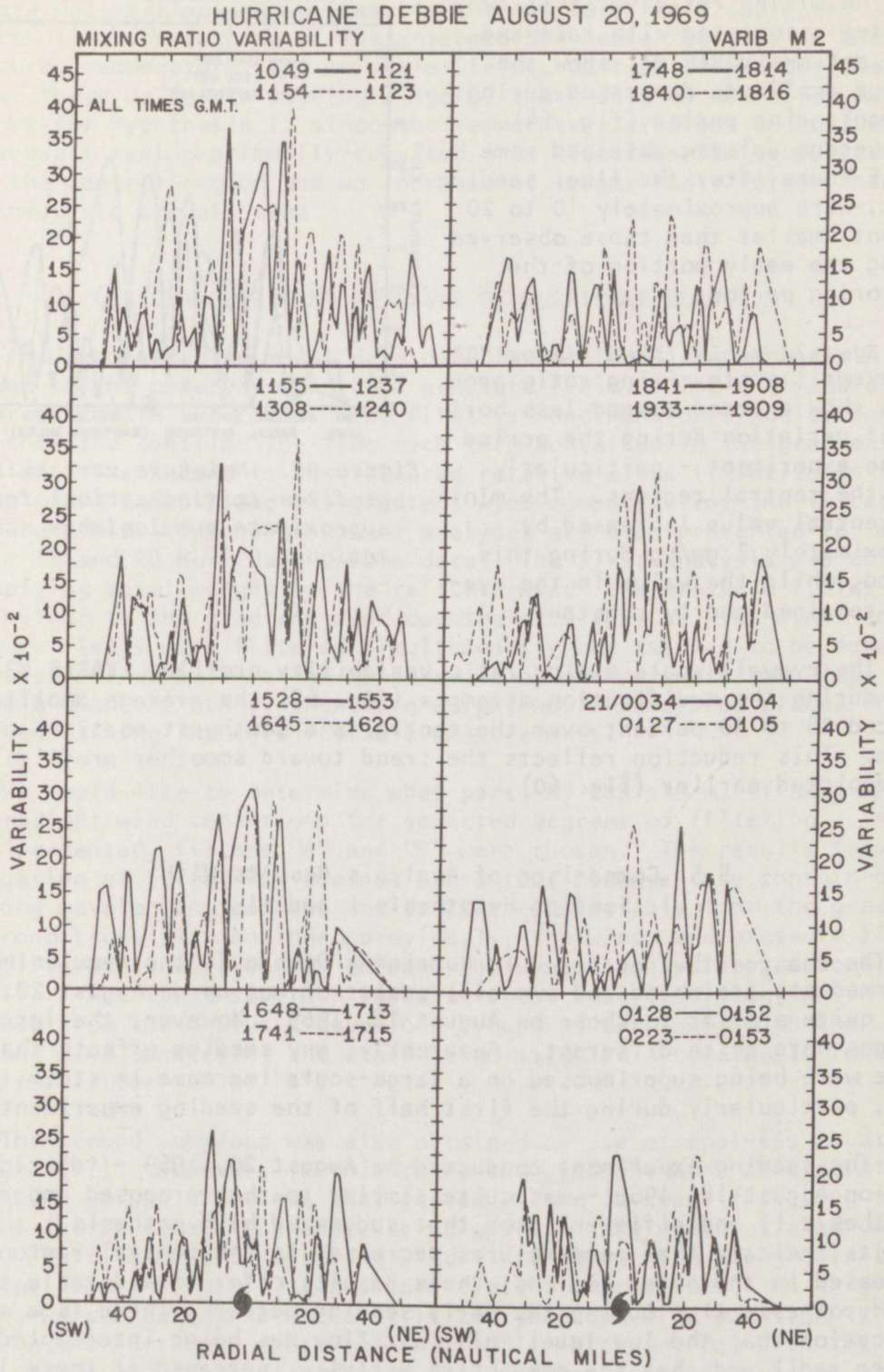

Figure 64. Moisture variability profiles (mixing ratios) for approximate rainband scale motion.

The mixing ratio variability profiles associated with rainband scale motion (VARIB M2) show the average amplitude decreased during the monitoring period (fig. 64). The average values, obtained some 3 to 5 hours after the final seeding event, were approximately 10 to 20 percent smaller than those observed during the early portion of the monitoring period.

Eyewall scale (band filter "F"). The eyewall scale mixing ratio profiles show a trend toward less horizontal variation during the period of the experiment - particularly over the central regions. The minimum central value increased by approximately 2 gm/kg during this period, while the value in the eyewall remained nearly constant.

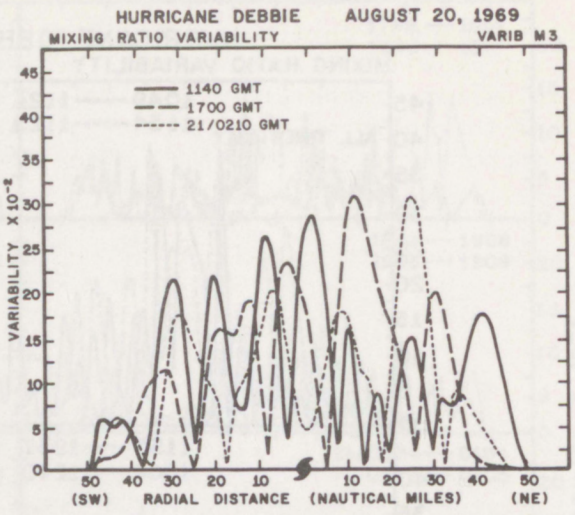

Figure 65. Moisture variability profiles (mixing ratios) for approximate cumulonimbus scale motion.

The eyewall scale mixing ratio variability profiles (VARIB M3) show that during the modification attempts (fig. 65) the average amplitude reduced 20 to 30 percent over the central and southwest portions of the storm. This reduction reflects the trend toward smoother profiles as was depicted earlier (fig. 60).

5.5 Comparison of Analysis Results With Seeding Hypothesis I and II

The changes that occurred in Hurricane Debbie in the cumulonimbus and intermediate (rainband and eyewall) scales of motion on August 20, 1969, were quite similar to those on August 18, 1969. However, the large-scale changes were quite different. Apparently, any seeding effects that took place were being superimposed on a large-scale increase in storm intensity, particularly during the first half of the seeding experiment period.

The seeding experiment conducted on August 20, 1969 - identical to that on August 18, 1969 - was quite similar to that proposed under Hypothesis II and different from that suggested by Hypothesis I. The net results indicate that temperatures decreased in the central region and increased in the outer regions; these results offer considerable support for Hypothesis II. During the early seeding periods, there is a strong indication that the low-level moist air flow was being intercepted at larger radii and that the convective activity increased at these locations and competed with the eyewall region for the low-level flow. The prominence of the eyewall structure decreased during the experiment. This

feature was particularly evident in the moisture field analyses. The net result was smoothing of the intermediate scale features in the pressure, temperature, and moisture fields, particularly after the time of the third or fourth seeding. Again, these data do not offer much support for Hypothesis I, since the temperature gradient reduction in the eyewall region primarily resulted from a decrease in temperature over the central region and an increase at larger radii rather than in the immediate eyewall area.

6. GRADIENT WIND ANALYSIS OF HURRICANE DEBBIE

The gradient wind model developed in section 3 and appendix A was applied to the observed wind- and pressure fields. The analyzed data are presented in two forms. The first is nondimensional scaled components that show the contribution from each term contained in the gradient wind equation. The second is the filtered relative winds (relative to the moving storm center) and the gradient wind computed from the filtered pressure field. Two subgroups of analyses are also presented for the August 18 and 20 Hurricane Debbie data. The first analysis was obtained by applying equal weight to the relative wind- and pressure fields and zero weight to the gradient wind constraint. That is, the wind- and pressure fields were filtered simultaneously and assumed to be equally accurate. If we believe the measurement of one parameter was less reliable than the other, then more weight would have been placed on the terms containing the more reliable measurements.

We would like to determine what parts of the storm, if any, meet the gradient wind conditions for selected degrees of filtering. In the cases presented, filters "A" and "B" were chosen. The results from application of filter "C" are not presented, because they contain only the long wavelength features and deviate considerably from the gradient wind condition. As mentioned previously, the wind- and pressure fields were filtered simultaneously through the use of analysis equations (16) and (17). The first subgroup represents the base condition, which was obtained from the analysis equations by use of zero weight on the gradient wind constraint and other terms weighted according to requirements for filter "A" or "B".

The second subgroup was also obtained by use of analysis equations (16) and (17). However, in this case, the gradient wind constraint was assigned a weight 100 times that placed on the low-pass filtering terms. This of course causes the analysis to approach the gradient wind condition. Profiles of the resulting wind field along with the gradient wind computed from the resulting pressure field are presented. In this manner, we can determine where or if the gradient wind equation is applicable in the hurricane where information is obtained from both the observed D values and the observed wind field. This knowledge of the wind-pressure relationship becomes very useful when developing simple hurricane models or when attempting to fill in missing data for analysis when either the pressure or the wind measurements are missing.

6.1 Hurricane Debbie - August 18, 1969

The profiles shown in figure 66 are for the periods before the first seeding, after the third seeding, and approximately 4 hours after the final seeding. Filter "A" has removed most of the high frequency components and some cumulus scale motion. However, some relatively large horizontal pressure gradient variations continued to be present. These variations were much greater when only the components with wavelengths less than 2 n miles were removed (not illustrated). The response profiles for the centrifugal and Coriolis terms are much smoother, reflecting the effect of the radial distance factor in the centrifugal term and the constant Coriolis parameter. The contribution from the Coriolis term is an order of magnitude smaller than the other two terms over the high energy portion of the storm. The primary effect that the gradient wind constraint had on the response of these three components was to smooth the pressure gradient profile. The other two profiles underwent only minor changes.

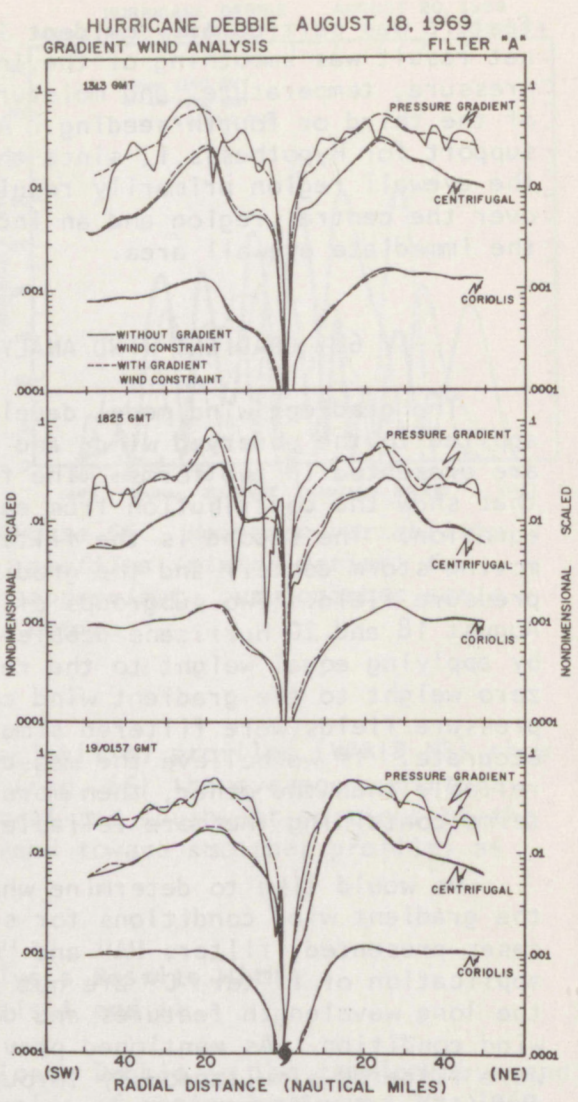

Figure 66. Gradient wind component analysis (August 18, 1969) resulting from application of filter "A" with and without the gradient wind constraint, to the observed pressure and wind fields.

The pressure gradient, particularly on the southwest side of the storm, underwent a major change during the monitoring period. This quantity had its largest horizontal variations during the actual seeding period (≈1825 GMT) and the least some 4 hours after the final seeding event. That is, the analysis that included the gradient wind constraint deviated most from that without the gradient wind constraint, during the seeding period and deviated least at the end of the monitoring period.

The wind profiles in figure 67 correspond to the analyses in figure 66. The profiles shown in panels A through C and D through F of figure 67 were obtained from the analysis represented by the solid and dashed lines respectively in figure 66. The relative wind profiles (relative

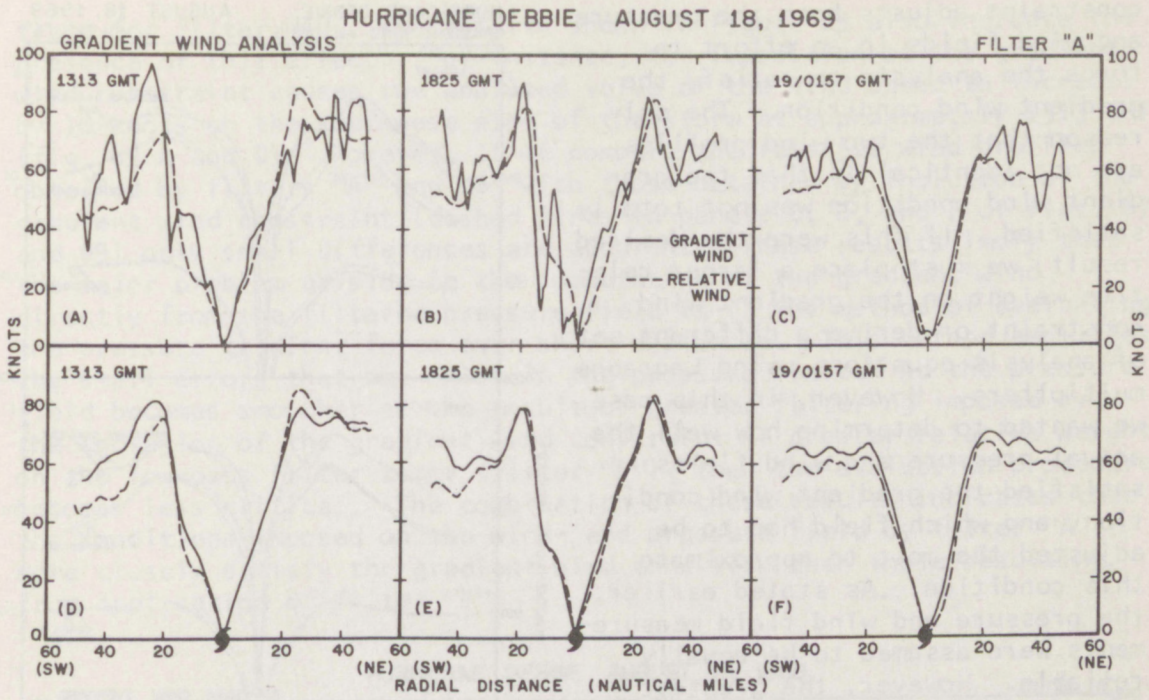

Figure 67. Wind speed profiles (August 18, 1969) resulting from application of filter "A" with (D, E, and F) and without (A, B, and C) the gradient wind constraint.

to the moving storm center) resulted directly from application of the analysis equations while the gradient wind was computed from the pressure profiles obtained from these same analysis equations. By comparing these sets of profiles, we can determine how well the analyzed pressure and wind fields approximate the gradient wind condition.

Panels A, B, and C of figure 67 illustrate the analysis results that exclude the gradient wind constraint. It is rather obvious that, in general, the gradient wind condition was not satisfied by the results obtained by application of filter "A" to the observed wind- and pressure fields. Also of considerable interest is that the pressure field showed a distinct trend toward satisfying the gradient wind condition during the monitoring period. That is, the gradient wind computed from the pressure field obtained by application of the analysis equations at 19/0157 GMT (panel C) is a much closer approximation of the corresponding relative wind profile for that time and location than is that obtained for the same two parameters at 1313 GMT (panel A).

The wind speed analyses obtained by the simultaneous applications of the gradient wind constraint and filter "A" for the same observed data described above are illustrated in D, E, and F, of figure 67. The best agreement between the relative wind and the computed gradient wind was obtained in the eyewall region at 1825 GMT. The gradient wind

constraint adjusts both the pressure and wind fields in an effort to force the analysis to satisfy the gradient wind condition. The only reason that the two wind profiles are not identical is that the gradient wind condition was not totally satisfied. If this were the desired result, we must place a larger relative weight on the gradient wind constraint or derive a different set of analysis equations using Lagrange multipliers. However, in this case, we wanted to determine how well the actual pressure and wind fields satisfied the gradient wind condition, and which field had to be adjusted the most to approximate this condition. As stated earlier, the pressure and wind field measurements were assumed to be equally reliable. However, the greatest effect of including the gradient wind constraint, was apparently to adjust the pressure field beyond that imposed by filter "A". This condition is illustrated by the gradient wind profiles in the upper panels of figure 67 differing considerably from their corresponding profiles in the lower panels. At the same time, the relative wind speed profiles for the two analyses differ only slightly for the same periods.

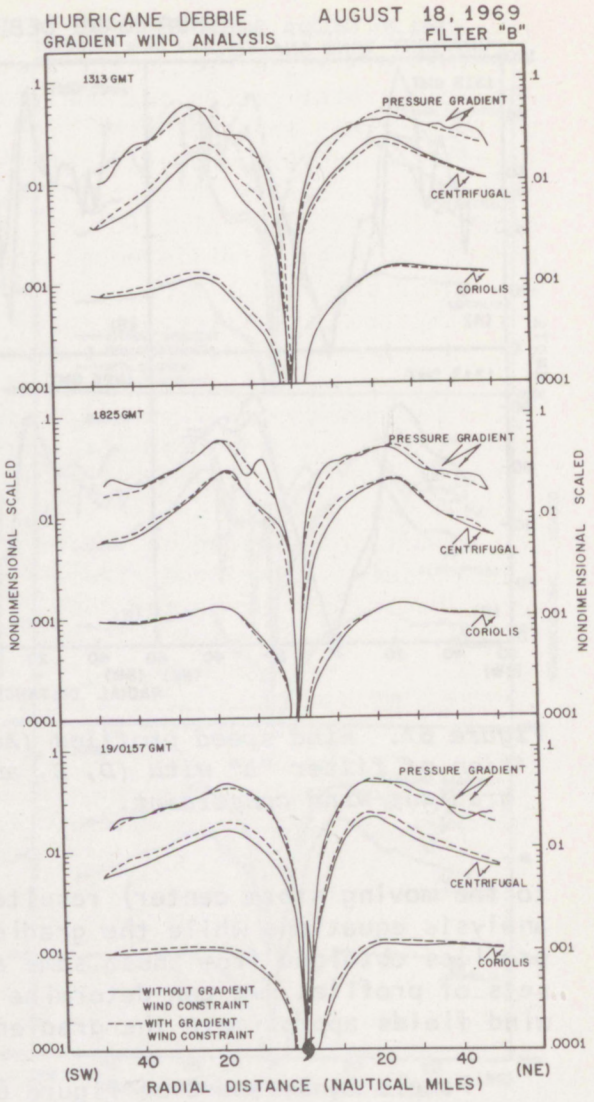

Figure 68. Gradient wind component analysis (August 18, 1969) resulting from application of filter "B" with and without the gradient wind constraint to the observed pressure and wind fields.

Figure 68 illustrates the gradient wind speed component analysis resulting from application of filter "B" with and without the gradient wind constraint. The general effect of filter "B" was to remove the cumulonimbus and smaller scale motions. The effect of this additional filtering is quite evident when comparing the results shown in figure 68 with those in figure 66. Another major difference between these two sets of data is that the difference between the profiles for the centrifugal and Coriolis terms, with and without the gradient wind constraint, is generally larger for filter "B" than for filter "A". This implies that the major effect of inclusion of the gradient wind constraint was to adjust the wind speed for filter "B" and to adjust the pressure

field for filter "A". The results shown in figure 69 also indicate the presence of this effect. For instance, the imposition of the gradient wind constraint causes the analyzed value of the wind speed to increase by 10 knots on the southwest side of the storm at approximately 1313 GMT (fig. 69 A and D). However, if we compare the relative wind profiles obtained by filters "A" and "B" with those obtained by inclusion of the gradient wind constraint (dashed lines in panels D, E, and F of figs. 67 and 69) only small differences are apparent. These results imply that the major problem arising in the computation of the gradient wind directly from the filtered pressure field is in the method of evaluating the pressure gradient force over short distances. This method amplifies the small errors that may exist in the pressure field. As the pressure field becomes smoother as the result of greater filtering imposed by the inclusion of the gradient wind constraint or greater relative weights on the low-pass filter terms (filter "B"), then the evaluation procedure becomes less critical. The combination of these results indicates that the conditions imposed on the wind- and pressure field by filter "A" more closely satisfy the gradient wind condition than those resulting from application of filter "B".

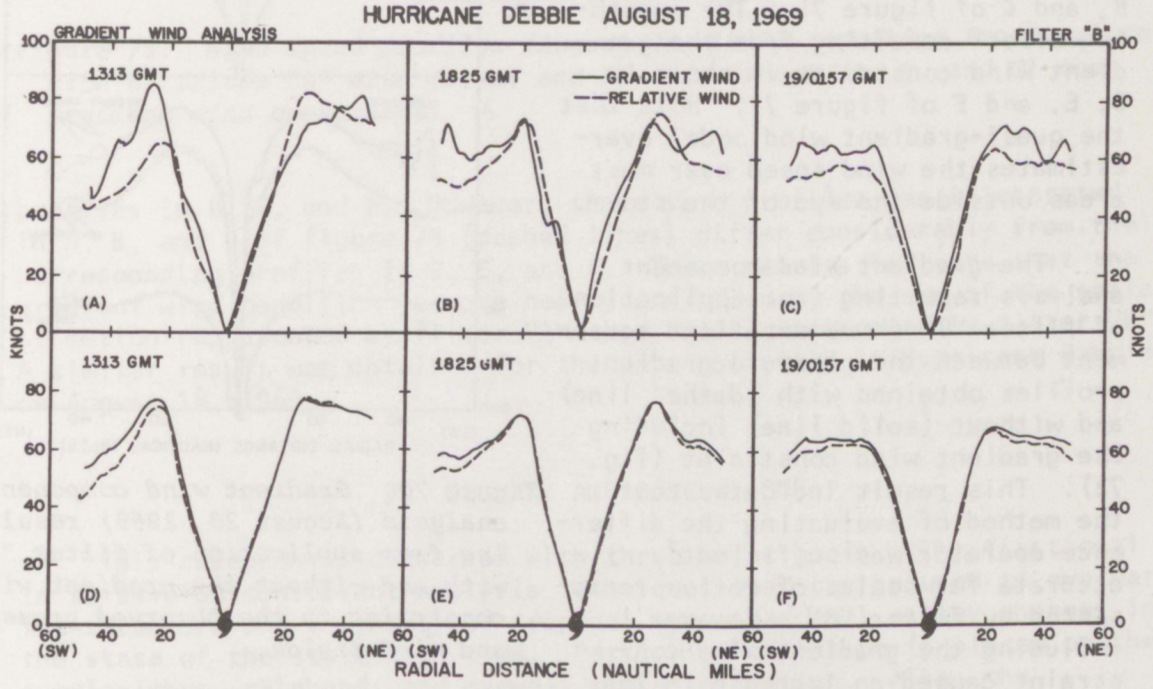

Figure 69. Wind speed profiles (August 18, 1969) resulting from application of filter "B" with (D, E, and F) and without (A, B, and C) the gradient wind constraint.

6.2 Hurricane Debbie - August 20, 1969

The components of the gradient wind (fig. 70) indicate a relatively good agreement between the profiles obtained with and those obtained without the gradient wind constraint for the three sets of profiles shown. Again, the profile of the pressure gradient term shows the largest fluctuations, and the general effect of the inclusion of the pressure gradient constraint was to smooth out these horizontal variations. These horizontal variations were amplified by the method of finite differencing over short space intervals that was used to obtain the gradient wind profiles shown in A, B, and C of figure 71. The smoothing effect resulting from the gradient wind constraint is shown in D, E, and F of figure 71. Note that the quasi-gradient wind model overestimates the wind speed over most areas outside the eye of the storm.

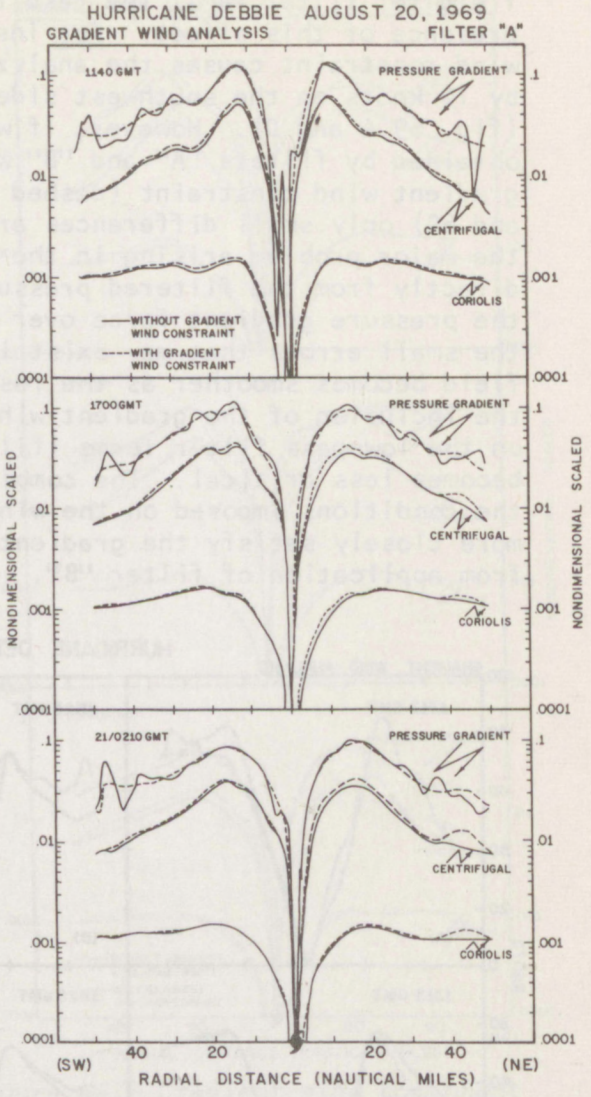

Figure 70. Gradient wind component analysis (August 20, 1969) resulting from application of filter "A" with and without the gradient wind constraint to the observed pressure and wind fields.

The gradient wind component analysis resulting from application of filter "B" shows excellent agreement between the pressure gradient profiles obtained with (dashed line) and without (solid line) including the gradient wind constraint (fig. 72). This result indicates that the method of evaluating the difference operator was sufficiently accurate for scales of motion represented by filter "B". However, including the gradient wind constraint caused an increase in the analyzed wind speed, which was reflected by the increased values for the Coriolis and centrifugal terms. This effect is further illustrated in figure 73. Here again, the gradient wind model tended to overestimate the actual wind speed for nearly all of the high energy portion of the storm. The results obtained by including the gradient wind constraint with filter "B" indicated a larger increase in the wind speed than obtained by use of filter "A". That is, the dashed-line profiles for A, B, and C of figure 71 differ only slightly from the corresponding

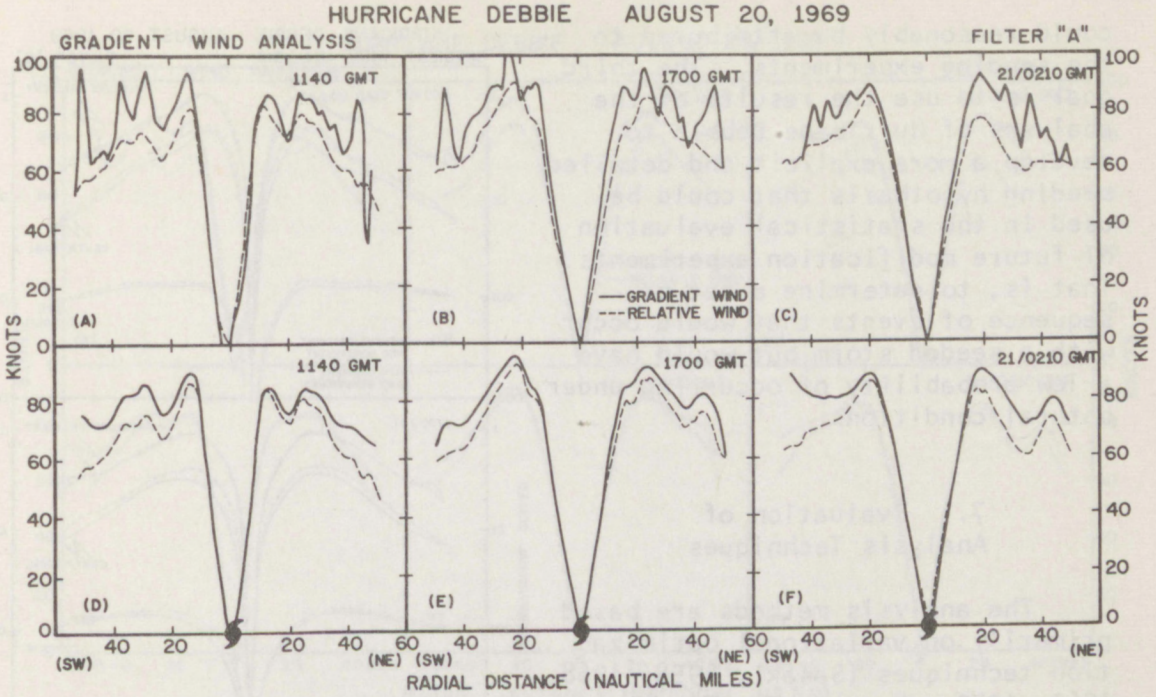

Figure 71. Wind speed profiles (August 20, 1969) resulting from application of filter "A" with (D, E, and F) and without (A, B, and C) the gradient wind constraint.

profiles in D, E, and F. However, these same profiles, as illustrated in A, B, and C of figure 73 (dashed lines) differ considerably from their corresponding profiles in D, E, and F. These results indicate that the gradient wind condition is more nearly satisfied by the sum of the scales of motion represented by filter "A" than those represented by filter "B". A similar result was obtained for the data collected in Hurricane Debbie on August 18, 1969.

7. SUMMARY AND CONCLUSIONS

This research is concerned with three basic goals. The first goal is to develop consistent analysis techniques that can be used to evaluate the structure and intensity of tropical storms as well as any changes in the state of the storm with time. Particular attention is placed on the cumulonimbus, rainband, and eyewall scales of motion. Also, the techniques should provide an objective means of comparing the analyzed results from one time to those of another time, as well as from one storm to another, where particular interest is placed on the high energy portion of the storm. The second goal is to apply these techniques to the data collected during modification experiments conducted on Hurricane Debbie (August 18 and 20, 1969) and evaluate changes that occurred in the storm structure. Also, we wish to determine what portion of these changes

could reasonably be attributed to the seeding experiments. The third goal is to use the results of the analyses of Hurricane Debbie to develop a more explicit and detailed seeding hypothesis that could be used in the statistical evaluation of future modification experiments. That is, to determine a set or sequence of events that would occur with a seeded storm but would have a low probability of occurring under natural conditions.

7.1 Evaluation of Analysis Techniques

The analysis methods are based primarily on variational optimization techniques (Sasaki, 1958, 1968, 1969, 1970a, b, c). The first series of analyses is based on analysis equation (5) derived in section 3 and appendix A. This analysis equation contains an observational constraint and two low-pass filter terms. By varying the relative weights on these terms, we attempt to selectively filter the recorded signal or input data observed from the airborne platform. Filtering of the data seems necessary to study in detail the small-scale motions which are often masked by the large-scale features in a hurricane. Likewise, small changes in the large-scale motions are often masked by the small-scale features. The changes in the large scale occurring during the early portions of the seeding experiment monitoring period are generally believed to be caused by features other than the seedings. Therefore, these contributions must be separated to determine the immediate and short range effects of the seeding operation.

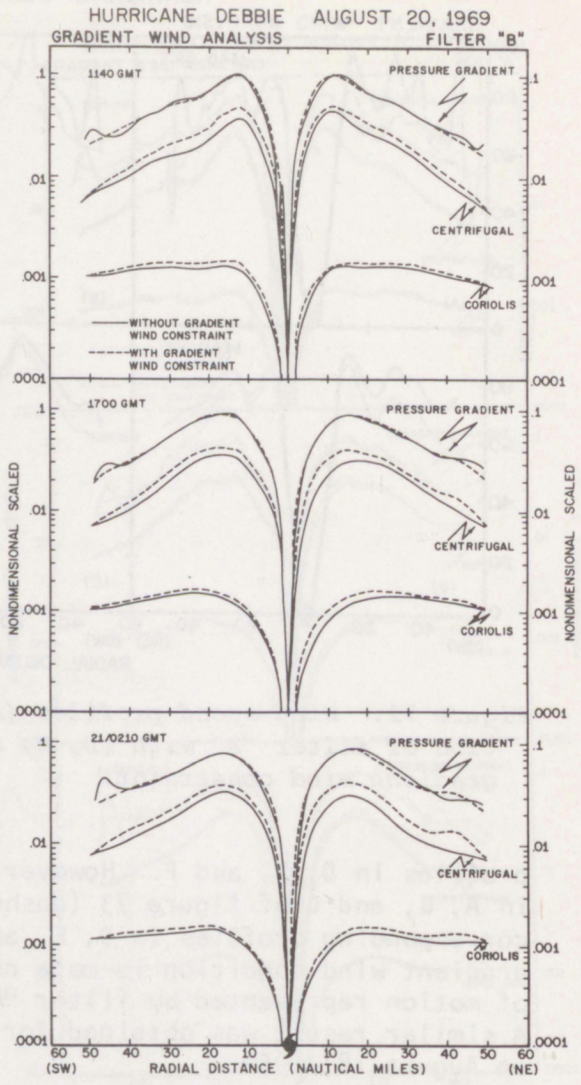

Figure 72. Gradient wind component analysis (August 20, 1969) with filter "B" with and without the gradient wind constraint to the observed pressure and wind field.

This separation of scales of motion is accomplished through use of low-pass and band-pass filters based on equation (5). The problems that often arise in standard filtering techniques seems to be minimal in these analyses. The degree to which we are successful in effectively separating small-scale features from the large-scale system is amply illustrated in the figures.

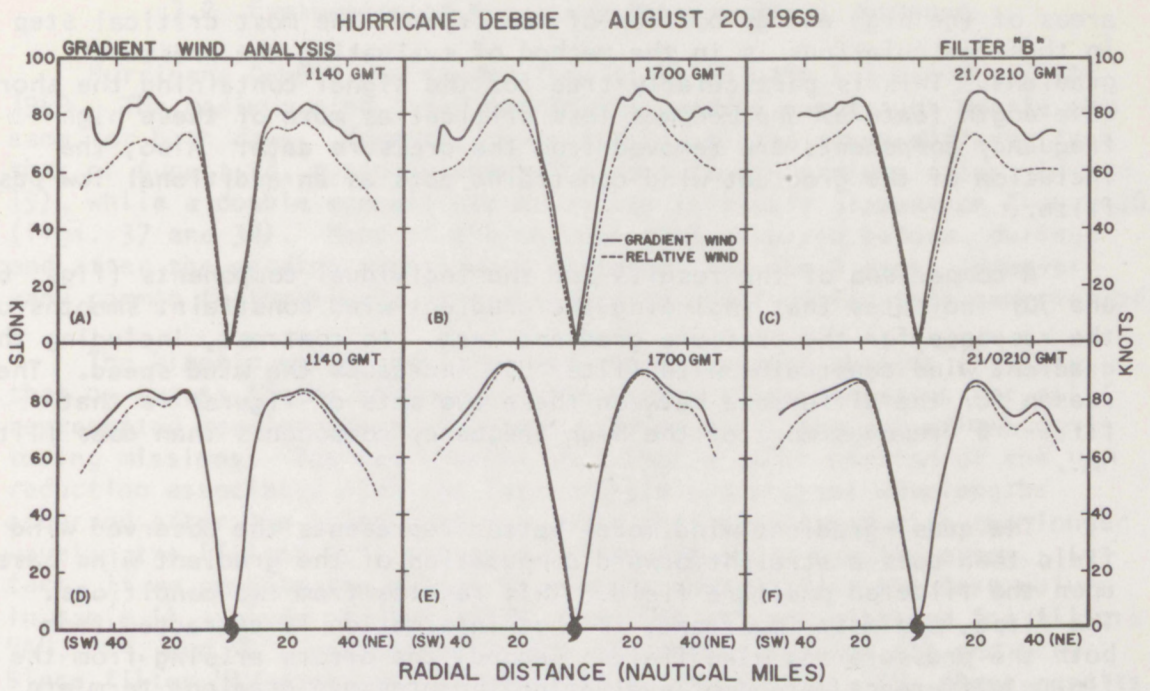

Figure 73. Wind speed profiles (August 20, 1969) resulting from application of filter "B" with (D, E, and F) and without (A, B, and C) the gradient wind constraint.

The variability factors are based on the filtered and band filtered data and some base condition, such as the mean tropical atmosphere. These factors are defined for selected scales of motion and the standard meteorological parameters. The information extracted by this technique generally compliments that obtained by the band filters. In addition, the signal is normalized by being a function of the magnitude of the parameter being investigated. This feature allows us to directly compare the variability factor for storms of various intensities. Also, these comparisons can be made in time and space for a particular storm. This feature is particularly important, if the character and/or magnitude of the computed factor for a particular scale is expected to change because of some natural or artificial phenomenon. The effectiveness of this analysis scheme varies, depending on the variable and scale being investigated.

The analysis equations containing the gradient wind constraint are designed to simultaneously extract information from the observed pressure and wind fields. In this manner, we can determine where, when, and for what scales of motion the gradient wind condition is most nearly satisfied. To accomplish this, we compute and display the scaled values for each of the contributing terms contained in the gradient wind equation. We find that, in general, the gradient wind computed from the pressure field overestimates the wind speed for most

areas of the high energy portion of the storm. The most critical step in these calculations is in the method of evaluating the pressure gradient. This is particularly true for the signal containing the shorter wavelength features and becomes less critical as more of these high frequency components are removed from the pressure data. Also, the inclusion of the gradient wind constraint acts as an additional low-pass filter.

A comparison of the results for the individual components (figs. 66 and 70) indicates that including the gradient wind constraint smooths out the response for the pressure gradient term. In contrast, including the gradient wind constraint with filter "B" increases the wind speed. The reason for the difference between these two sets of figures is that filter "B" removes more of the high frequency components than does filter "A".

The quasi-gradient wind model better represents the observed wind field than does a straightforward computation of the gradient wind based upon the filtered pressure field. This results from two conditions. The first, and most important, is that information is extracted from both the pressure and wind fields; second, the errors arising from the finite difference method of evaluating the pressure gradient term are decreased by the increased filtering imposed by the gradient wind constraint. That is, the wind analysis resulting from the quasi-gradient wind model provides a better representation of the filtered wind than does the gradient wind computed from the pressure field undergoing the same degree of filtering.

The results from the quasi-gradient wind model, of course, are not forced to identically satisfy the gradient wind condition. However, the analysis is forced to approach this condition since we place a relatively large weight on the gradient wind constraint. The analysis could be forced even more toward the gradient wind condition by placing a larger relative weight on the appropriate constraint, but the resulting analysis would deviate even more from the corresponding relative wind profiles.

The result of this analysis is that the quasi-gradient wind model does a relatively good job of simulating the wind speed profiles over the high energy portion of the storm. This is especially true for those scales of motion retained with the application of filter "A". This model can then be used in areas where wind speed data are missing, which sometimes happens in very heavy precipitation areas. The results for the missing data areas would be even better than those obtained from analysis equation (5), which can be viewed as somewhat of a least-strain curve fitting technique since the model simultaneously extracts information from the wind- and pressure fields.

7.2 Evaluation of Hurricane Debbie (1969) Analyses

Hurricane Debbie was seeded five times on both August 18 and 20, 1969. The maximum wind speed before the seeding events was nearly the same for both days. However, the structure of the storm differed in that on August 18, a single eyewall structure was present (figs. 18 and 19), while a double eyewall structure was initially present on August 20 (figs. 37 and 38). Many of the changes that occurred before, during, and after the seeding events were different for the 2 days. However, many common features were also observed to occur during this same period.

The kinetic energy profiles and the percentage changes indicate that on August 18 the maximum kinetic energy value decreases for all represented wavelengths from before seeding until the end of the monitoring missions. The net changes show that a major portion of the reduction associated with the intermediate and shorter wavelengths occurred after the third seeding, while that associated with the longer wavelengths (filter "C") occurred before the third seeding event. In fact, if we compute the change in kinetic energy (from the last column in table 1), values of -341, -479, and -640 kt^2 are obtained for filters "A", "B", and "C", respectively, for the change between (1) and (2). Since filter "A" contains "B" and filter "B" contains "C", these results indicate that a major reduction occurred in the longer wavelengths, and that the intermediate and shorter wavelengths were actually enhanced during this period. However, if these same quantities are computed for the time period from (2) to (3) (after the third seeding until near the end of the monitoring period), values of -1368, -942, and -280 kt^2 are obtained for filters "A", "B", and "C" respectively. These values indicate that the long wave feature continued to decrease in intensity during this period, but at a much slower rate than before. Also, the intermediate and shorter wavelength features that were enhanced before the third seeding reduced dramatically during this period.

The resulting changes of kinetic energy obtained for August 20, 1969, showed some different characteristics. The changes in kinetic energy (for the last column in table 2) are 138, 233, and 21 kt^2 for filters "A", "B", and "C", respectively, for the period of (1) to (2) (before the first seeding until after the third seeding event). These results indicate an increase in kinetic energy for the sum of all the wavelengths represented. However, most of this increase was confined to features of eyewall scale or larger for this period. The same quantities for the period of after the third seeding until the end of the monitoring period are -167, -90 and -60 kt^2 for filters "A", "B", and "C", respectively. These results imply a reduction at all wavelengths represented, since the value for filter "A" is a larger negative number than for "C".

A summary of the kinetic energy analyses for these two seeding experiments indicates that on August 18 a large-scale decrease, which cannot reasonably be attributed to the seeding operation, occurred before

and during most of the monitoring period. Likewise, a large-scale increase in kinetic energy occurred on August 20 during the early portion of the seeding operation. A major portion of this increase was apparently associated with the change from a double to a single eyewall structure and, also, could not reasonably be attributed to the seeding operation. However, a significant decrease occurred in these longer wavelength features after the third or fourth seeding. In general, the smaller and intermediate scale features showed some enhancement during the early portion of the seeding operations on both days, and then a distinct decrease through the end of the monitoring periods.

The analyses of the pressure fields for August 18 show a general decrease in the pressure gradient associated with the large-scale feature (fig. 19) occurring during the seeding experiment. Most of this change took place before the third seeding, a condition also observed in the kinetic energy analyses. However, the minimum central pressure showed little change between the times of the first and last passes. The pressure profiles associated with cumulonimbus (fig. 20), rainband, and eyewall (fig. 22) scales also exhibited characteristics similar to those of the kinetic energy analyses. That is, these scales show a general decrease in the magnitudes of their extreme values, with most of the change occurring after the third seeding.

The analyses of pressure for August 20 also show a general decrease in the pressure gradient for the long wave features after the third seeding event. The cumulonimbus scale pressure profiles (fig. 49) show the magnitudes of the extreme values reduced near the end of the seeding operation. Note that the variability associated with this parameter for August 20 (fig. 50) initially is considerably smaller than that for August 18. However, the results at the end of the monitoring periods are quite similar for both days. The rainband and eyewall scales on August 20 also show distinct pressure gradient decreases occurring during the seeding operation.

The temperature analyses for these same periods exhibit characteristics almost identical to those of the pressure analyses. That is, a general reduction in the temperature gradients for nearly all scales represented occurred during the modification experiment. In addition, temperature decreases and increases occurred over the central and outer regions of the storm, respectively.

The moisture analyses also exhibit the same general characteristics as the pressure and temperature fields. However, in addition to these characteristics, the moisture level showed a distinct and significant increase on both days over most of the high energy portion of the storm during the modification experiments (figs. 31 and 60). Most of this increase was associated with the longer wavelength feature. Also, the distinct dry region over the central portions of the storm, present during the early passes, became almost nonexistent by the end of the monitoring period. The eyewall regions, quite distinct in the moisture analyses for the early passes, were also nearly eliminated (figs. 34 and 63).

The following general observations can be made about the overall changes in structure that occurred during the seeding experiments discussed. First, during the experiments, a general reduction in the amplitudes and gradients of most of the parameters analyzed occurred on both days for scales of motion of eyewall scale or smaller. This reduction generally occurred after the third or fourth seeding, i.e., some 4 to 6 hours after the first seeding run. There appeared to be a temporary enhancement of the smaller scale features during the early portions of the seeding operation, but the evidence for this condition was generally not as strong as for the decrease for these same scales during the latter portions of the experiment periods. Also of particular interest is the moisture level rose over most of the high energy portion of the storm, and in general the structure of the storm became more symmetrical for nearly all parameters during the modification experiments. These similarities in changes for the two seeding cases (August 18 and 20) occurred despite the fact that the long wave features were acting in opposite directions for August 18 as compared with those for August 20. These results offer strong evidence supporting the basic seeding hypothesis discussed in section 2. They are the basis for the more explicit hypothesis proposed in the next section.

7.3 Proposed Seeding Hypothesis

This proposed hypothesis is basically an elaboration of Hypothesis II discussed in section 2. The details are based on the interpretation of the results described here and results of other seeding experiments conducted on cloudlines, individual clouds, and cloud groups. The intent is to help explain events that may occur in a hurricane seeding operation and to propose a sequence of events that hopefully are likely to occur with a particular seeding experiment and is highly unlikely to occur naturally. If successful, this hypothesis would be of considerable aid in the statistical evaluation of hurricane seeding experiments.

Hypothesis II calls for seeding from the exterior edge of the band of maximum winds radially outward for approximately 20 n miles. The basic idea is to enhance convection at radii greater than the eyewall. The analysis indicates that this effect probably took place during the early portions of the seeding operations on both August 18 and 20. The sequence of events that could reasonably be expected to occur is that first the individual towers or cells containing supercooled water would grow; and this, along with the fact that the seeding occurs in a somewhat continuous manner over a 20 n mile interval, would cause the systems to merge over this region. Simultaneously, the strong horizontal wind components would spread the seeding agent, and thus its effect, around the high energy portion of the storm. The widespread enhanced convection would raise the moisture levels throughout the high energy portion of the storm. At the same time, the increased convection at radii larger than the eyewall would decrease the prominence of the eyewall by competing with it for the low-level inflowing moisture-laden

air. The merging of the cloud systems would also decrease the prominence of the individual cumulonimbus clouds and hurricane rainbands. Each of these features can be interpreted to have occurred in Hurricane Debbie (1969) on both August 18 and 20. The periods over which these changes took place was sometimes difficult to determine, primarily because of the inability to monitor seeded areas continuously. Some regions near the seeded areas were monitored shortly after seeding; apparently there was a nearly instantaneous reaction to the seeding. Of course, the number of such cases is few, so it is difficult to state with a large degree of confidence that this short term change was directly related to the seeding event. However, an almost instantaneous reaction to seeding agents has been observed in STORMFURY cloudline seeding experiments (fig. 1) and in numerous individual cumulus seeding experiments, such as those conducted by Simpson and Woodley (1971). It is reasonable to assume that this same reaction could be expected in the hurricane environment when we consider the computations previously made by the author (Sheets, 1969c).

We will now innumerate the sequence of events that should occur in a hurricane seeded similar to that done in Hurricane Debbie (1969) - one having a distinct eyewall structure with an associated maximum wind speed band. This same sequence actually occurred on both days that Hurricane Debbie (1969) was seeded, or at least we can imply this occurred from the interpretation of the analyzed data.

The sequence of events and results are:

1. Enhancement of small-scale features as depicted in the wind, temperature, and pressure field (cumulus and cumulonimbus scales) in the immediate vicinity of the seeded area particularly beyond the eyewall region - within minutes of the actual seeding event. This reaction should occur with the first three or four seeding events (4 to 6 hours after first seeding run).

2. Intermediate scale features, as depicted in the wind, temperature, pressure, and moisture fields (rainband and eyewall scales), remain prominent or slightly enhanced during the first three or four seeding events.

3. By the third or fourth seeding, the seeding agent and its effects are dispersed over the high energy portion of the storm with the following results occurring and persisting through the next 6 to 8 hours (from 6 to 14 hours after the commencement of the seeding operation):

    a. A general reduction in the temperature, pressure, and moisture gradients, particularly for rainband and eyewall scale motions, and with the resulting reduction in the prominence of these features.

b. A reduction in the maximum temperature values over the central regions and an increase in temperature at radii beyond the eyewall region.

c. A general increase in the moisture levels for the large-scale features covering the high energy portion of the hurricane.

The conclusions drawn above are based upon and applied to data collected in the mid- and lower troposphere. However, with the vertical continuity known to exist in a hurricane, these results should apply to most of the tropospheric portion of the hurricane.

8. ACKNOWLEDGMENTS

Professor Sasaki deserves considerable credit for his scientific advice, without which the research reported in this paper would not have been completed. Considerable time on the University of Oklahoma IBM 360 and 1130 systems as well as the CDC 6600 and 7600 at the National Center for Atmospheric Research was also provided through the efforts of Professor Sasaki.

The basis for the work presented in this paper has evolved from more than 6 years of research by the author at the NOAA National Hurricane Research Laboratory and during a year at the University of Oklahoma under a NOAA scholarship. Scientific direction and advice were received from Dr. R. Cecil Gentry, Dr. Harry F. Hawkins, Dr. Stanley L. Rosenthal, and Dr. Banner I. Miller during this period. Almost the entire staff of NHRL has contributed to some phase of the research effort and to preparing this paper for publication. Special thanks is also due to the crews of the NOAA Research Flight Facility aircraft who collected the majority of the data.

9. REFERENCES

Black, P. G., H. V. Senn, and C. L. Courtright (1970): Eye-size changes in Hurricane Debbie on 18 and 20 August 1969. Project STORMFURY Annual Report 1969, Appendix E, (National Hurricane Research Laboratory, Miami, Florida).

Colon, J. A. and Staff (1961): On the structure of Hurricane Daisy (1958). National Hurricane Research Project Report No. 48, (U.S. Department of Commerce, Washington, D. C.), 102 pp.

Colon, J. A. (1964): On the structure of Hurricane Helene (1958). National Hurricane Research Project Report No. 72, (U.S. Department of Commerce, Washington, D. C.), 56 pp.

Friedman, H. A., F. S. Cicirelli, and W. S. Freedman (1969a): The ESSA Research Flight Facility: facilities for airborne atmospheric research. ESSA Technical Report ERL 126-RFF 1, (U.S. Government Printing Office, Washington, D. C.), 89 pp.

Friedman, H. A., M. R. Ahrens, and H. W. Davis (1969b): The ESSA Research Flight Facility: data processing procedures. ESSA Technical Report ERL 132-RFF 2, (U. S. Government Printing Office, Washington, D. C.), 67 pp.

Gentry, R. C. (1970): Hurricane Debbie modification experiments, August 1969. Science, 168, 473-475.

Hawkins, H. F. and D. T. Rubsam (1968): Hurricane Hilda, 1964 II. Structure and budgets of the hurricane on October 1, 1964. Monthly Weather Review, 96, No. 9, 617-636.

Jordan, C. L. (1958): Mean soundings for the West Indies area. J. Meteorology, 15, 91-97.

LaSeur, N.E. and H. F. Hawkins (1963): An analysis of Hurricane Cleo (1958) based on data from research reconnaissance aircraft. Monthly Weather Review, 91,(10 to 12), 694-709.

Rosenthal, S. L. (1971): Numerical experiments of relevance to Project STORMFURY. NOAA Technical Memorandum ERL NHRL-95, (U.S. Department of Commerce, National Hurricane Research Laboratory, Miami, Florida), 52 pp.

Sasaki, Y. (1958): An objective analysis based on the variational method. J. Meteor. Soc. Japan, 36, 77-88.

Sasaki, Y. (1968): Numerical Variational Method of Objective Analysis: Principle of Initialization. University of Oklahoma Research Institute, Report No. 10, 21 pp.

Sasaki, Y. (1969): Proposed inclusion of time vatiation terms, observational and theoretical, in numerical variational objective analysis. J. Meteor. Soc. Japan, 47, No. 2, 115-124.

Sasaki, Y. (1970a): Some basic formalisms in numerical variational analysis. Monthly Weather Review, 99, No. 12, 875-883.

Sasaki, Y. (1970b): Numerical variational analysis formulated under the constraints as determined by longwave equations and a low-pass filter. Monthly Weather Review, 99, No. 12, 884-899.

Sasaki, Y. (1970c): Numerical variational analysis with weak constraint and application to surface analysis of severe storm gust. Monthly Weather Review, 98, No. 12, 900-912.

Sheets, R. C. (1967a): On the structure of Hurricane Janice (1958). National Hurricane Research Laboratory Report No. 76, (U.S. Department of Commerce, National Hurricane Research Laboratory, Miami, Florida), 38 pp.

Sheets, R. C. (1967b): On the structure of Hurricane Ella (1962). National Hurricane Research Laboratory Report No. 77, (U.S. Department of Commerce, National Hurricane Research Laboratory, Miami, Florida), 33 pp.

Sheets, R. C. (1968): The structure of Hurricane Dora (1964). National Hurricane Research Laboratory Report No. 83, (U.S. Department of Commerce, National Hurricane Research Laboratory, Miami, Florida), 64 pp.

Sheets, R. C. (1969a): Some mean hurricane soundings. J. of Applied Meteorology, 8, No. 1, 134-146.

Sheets, R. C. (1969b): Preliminary analysis of cloud physics data collected in Hurricane Gladys (1968). Project STORMFURY Annual Report 1968, Appendix D, (National Hurricane Research Laboratory, Miami, Florida).

Sheets, R. C. (1969c): Computations of the seedability of clouds in the environment of a hurricane. Project STORMFURY Annual Report 1968, Appendix E, (National Hurricane Research Laboratory, Miami, Florida).

Sheets, R. C. (1970): Application of bayesian statistics for STORMFURY results. Project STORMFURY Annual Report 1969, Appendix H, (National Hurricane Research Laboratory, Miami, Florida).

Sheets, R. C. (1972a): Diurnal variation on hurricanes. Project STORMFURY Annual Report 1971, Appendix G, (National Hurricane Research Laboratory, Miami, Florida), 121-126.

Sheets, R. C. (1972b): Some statistical characteristics of the hurricane eye and the minimum sea-level pressure. Project STORMFURY Annual Report 1971, Appendix I, (National Hurricane Research Laboratory, Miami, Florida), 143-156.

Simpson, J. S. and W. L. Woodley (1971): Seeding cumulus in Florida: New 1970 results. Science, 172, 117-126.

Simpson, R. H. and J. S. Malkus (1964): Experiments in hurricane modification. Scientific American, 211, No. 6, 27-37.

Thompson, P. D. (1961): Numerical Weather Analysis and Prediction. The Macmillan Company, New York.

Wagner, K. K. (1971): Variational analysis using observational and low-pass filtering constraints. Department of Meteorology, University of Oklahoma, Norman, Oklahoma, 39 pp.

Woodley, W. L. (1970): Rainfall enhancement by dynamic cloud modification. Science, 170, 127-132.

APPENDIX A

Mathematical Definitions and Derivations

A.1 Definitions

The definitions and approximations listed below are used in the derivations that follow. The units of the various quantities are given in knots (kts), nautical miles (n miles), degrees centigrade (C), and grams per kilogram (gm/kg), since these are the units normally associated with airborne meteorological observations.

The scale parameters are

$V = 100$ kt, $T = 10°C$, $M = 10$ gm/kg,

$L = 20$ n miles $D = 0.1$ n miles,

$g = 980$ cm/sec^2 $= 6.8515 \times 10^4$ n miles/hr^2,

$f = 4.98802 \times 10^{-5}$/sec $= 0.1795687$/hr at 20°N.

The nondimensional variables and operators are defined as

$$r = Lr', \quad c = Vc', \quad z = Dz',$$

$$v_\theta = Vv_\theta', \quad T = \bar{T}t', \quad \theta = \Theta_\theta',$$

$$V = VV', \quad v = Vv', \quad M = \bar{M}M',$$

$$z = Dz', \quad D = \bar{D}D', \quad \nabla_r = \frac{1}{L}\nabla_r',$$

where the primed quantities are the nondimensional form of the variables and operators. The variables v_θ and v_r are the tangential and radial components of the wind, respectively, T is temperature, M is mixing ratio, D is the height anomaly of a given pressure surface from the same surface in the U. S. Standard Atmosphere (D-value), V is the observed wind speed, z is the observed height of the pressure surface, and C is the gradient wind speed.

The finite difference operators used are centered differences, i.e.,

$$\nabla_r\theta = (\theta_{n+1} - \theta_{n-1})/2d,$$

$$\nabla_r^2\theta = \nabla_r\nabla_r\theta_n \quad , \text{ and}$$

$$\nabla_r^n\theta = \nabla_r\nabla_r\ldots\nabla\theta,$$

where θ is any variable and d is the interval Δr. The subscript n indicates the increment of Δr along the radial axis.

A.2 Scaling and Nondimensionalization of J_1

The first functional is defined in section 2 as

$$J_1 = \int_r \{\beta(\frac{\partial^2\theta}{\partial r^2})^2 + \gamma(\frac{\partial\theta}{\partial r})^2 + \alpha(\theta - \tilde{\theta})^2\}dr. \qquad (A.1)$$

The scale parameters and nondimensional variables defined above are used to derive a nondimensional finite difference analog for (A.1), i.e.,

$$J_1 = \sum_r \{\frac{\beta\Theta^2}{L^4}(\nabla'_r{}^2\theta')^2 + \gamma\frac{\Theta^2}{L^2}(\nabla'_r\theta')^2 + \alpha\Theta^2(\theta'-\tilde{\theta})^2\}\Delta r.$$

The terms $\beta\Theta^2/L^4$, $\gamma\Theta^2/L^2$, and $\alpha\Theta$ must also be nondimensionalized. To accomplish this task, we choose the nondimensional values for β, γ, and α and then determine the implied dimensional weight from the prior given definitions and scale parameters. For instance, one set of nondimensional weights used in the analyses performed in this paper is $\alpha = 1$, $\gamma = \beta = 100$. Letting θ be the tangential component of the wind, we obtain

$$\beta' = \frac{\beta\Theta^2}{L^4} = \frac{\beta V^2}{L^4} \text{ or } \beta = \frac{\beta' L^4}{V^2} = \frac{100 \times 100^2 \times 16 \text{ n mi}^4}{100^2 \text{n mi}^2 \text{hr}^{-2}}$$

$$= 1.6 \times 10^2 \text{ n mi}^2 \text{ hr}^2,$$

and

$$\gamma' = \frac{\gamma\Theta^2}{L^2} = \frac{\gamma V^2}{L^2} \text{ or } \gamma = \frac{\gamma' L^2}{V^2} = \frac{100 \times 100 \times 4 \text{ n mi}^2}{100^2 \text{n mi}^2 \text{hr}^{-2}} = 4 \text{ hr}^2,$$

$$\alpha' = \alpha\Theta = \alpha V \text{ or } \alpha = \frac{\alpha'}{V} = \frac{1}{100 \text{ n mi hr}^{-1}} = 10^{-2} \text{ hr n mi}^{-1}.$$

The nondimensional finite difference analog of (A.1) becomes

$$J_1 = \sum_r \{\beta' (\nabla'_r{}^2\theta')^2 + \gamma'(\nabla'_r\theta')^2 + \alpha'(\theta' - \tilde{\theta})^2\}\Delta r, \quad (A.2)$$

and for convenience we can drop the prime notation since all terms are now nondimensionalized.

A.3 Solution of Equation (5)

The analysis equation derived from (A.2) becomes

$$\beta\nabla_r{}^4\theta - \gamma\nabla_r{}^2\theta + \alpha(\theta - \tilde{\theta}) = 0. \quad (A.3)$$

The finite difference operators $\nabla_r{}^2\theta$ and $\nabla_r{}^4\theta$ are defined by

$$\nabla_r{}^2\theta = (\theta_{n+1} + \theta_{n-1} - 2\theta_n)/d^2$$

and

$$\nabla_r{}^4\theta = (\theta_{n+2} + \theta_{n-2} + 6\theta_n - 4\theta_{n+1} - 4\theta_{n-1})/d^4.$$

Equation (A.3) is readily solved by iterative techniques. The Liebmann method, used for this paper, requires that the corrected values for θ must satisfy the analysis equation. That is, if a residual exists at a point on the νth iteration, then a correction must be applied to that point such that there would be no residual on the $\nu+1$ iteration. However, this calculation uses values from surrounding points that also must be corrected. Therefore, the method "iterates" toward the correct solution. The form chosen for the finite difference approximations is used in order to minimize the number of fixed end points required. The residual on the νth scan at the n^{th} point is

$$R_n^\nu = \beta[\theta_{n+2}^\nu + \theta_{n-2}^{\nu+1} + 6\theta_n^\nu - 4\theta_{n+1}^\nu - 4\theta_{n-1}^{\nu+1}]/d^4$$

$$- \gamma[\theta_{n+1}^\nu + \theta_{n-1}^{\nu+1} - 2\theta_n^\nu]/d^2 + \alpha[\theta_n^\nu - \tilde{\theta}_n]. \quad (A.4)$$

The required condition for the $\nu+1$th iteration at the nth point is

$$0 = \beta[\theta^{\nu}_{n+2} + \theta^{\nu+1}_{n-2} + 6\theta^{\nu+1}_{n} - 4\theta^{\nu}_{n+1} - 4\theta^{\nu+1}_{n-1}]/d^4$$

$$- \gamma[\theta^{\nu}_{n+1} + \theta^{\nu+1}_{n-1} - 2\theta^{\nu+1}_{n}]/d^2 + \alpha[\theta^{\nu+1}_{n} - \tilde{\theta}_n], \quad (A.5)$$

where

$$\theta^{\nu+1}_{n} = \theta^{\nu}_{n} + \Delta\theta^{\nu}_{n} \text{ or } \Delta\theta_n = \theta^{\nu+1}_{n} - \theta^{\nu}_{n}. \quad (A.6)$$

The term $\Delta\theta^{\nu}_{n}$ is the correction factor to be applied to θ^{ν}_{n} and is obtained by subtracting (A.4) from (A.5), i.e.,

$$-R^{\nu}_{n} = 6\beta(\theta^{\nu+1}_{n} - \theta^{\nu}_{n})/d^4 + 2\gamma(\theta^{\nu+1}_{n} - \theta^{\nu}_{n})/d^2$$

$$+ \alpha(\theta^{\nu+1}_{n} - \tilde{\theta}_n),$$

or making use of (A.6),

$$\Delta\theta^{\nu}_{n} = - R^{\nu}_{n}/[6\beta/d^4 + 2\gamma/d^2 + \alpha]. \quad (A.7)$$

Appropriate values are chosen for the weights α, γ, and β. An initial field is specified based on the observed data, and along with the observed values is inserted in (A.4), (A.6), and (A.7). In actual practice, an over relaxation factor (Thompson, 1961) is used, i.e., (A.6) becomes

$$\theta^{\nu+1}_{n} = \theta^{\nu}_{n} + 1.9 \times \Delta\theta^{\nu}_{n}. \quad (A.8)$$

The rate of convergence to the solution using this technique is illustrated in figure 5 for a typical set of data.

A.4 Scaling and Nondimensionalization of J_2

The functional containing J_1 and the gradient wind constraint is defined in section 2 as

$$J_2 = \sum_{r} \{\alpha(c - \tilde{v})^2 + \gamma(z - \tilde{z})^2 + \beta\left(\frac{c^2}{r} + fc - g\frac{\partial z}{\partial r}\right)^2$$

$$+ \mu_1\left(\frac{\partial c}{\partial r}\right)^2 + \mu_2\left(\frac{\partial^2 c}{\partial r^2}\right)^2 + \mu_3\left(\frac{\partial z}{\partial r}\right)^2 + \mu_4\left(\frac{\partial^2 z}{\partial r^2}\right)^2\}dr. \quad (A.9)$$

The scale parameters and nondimensionalized variables defined previously are used to derive a nondimensionalized finite difference analog for (A.9), i.e.,

$$J_2 = \sum_r \{\alpha V^2(c' - \tilde{v}')^2 + \gamma D^2(z' - \tilde{z}')^2$$
$$+ \beta \left(\frac{V^2 c'^2}{Lr'} + fvc' - g\frac{D}{L}\nabla'_r z'\right)^2$$
$$+ \mu_1\left(\frac{V}{L}\nabla'_r c'\right)^2 + \mu_2\left(\frac{V}{L^2}\nabla'_r{}^2 c'\right)^2$$
$$+ \mu_3\left(\frac{D}{L}\nabla'_r z'\right)^2 + \mu_4\left(\frac{D}{L^2}\nabla'_r{}^2 z'\right)^2\}\Delta r$$

or

$$J_2 = \sum_r \{\alpha V^2(c' - \tilde{v}')^2 + \gamma D(z' - \tilde{z}')^2$$
$$+ \beta \frac{V^4}{L^2}\left(\frac{c'^2}{r'} + \frac{fL}{V}c' - \frac{gD}{V^2}\nabla'_r z'\right)^2$$
$$+ \mu_1 \frac{V^2}{L^2}(\nabla'_r c')^2 + \mu_2 \frac{V^2}{L^4}(\nabla'_r{}^2 c')^2$$
$$+ \mu_3 \frac{D^2}{L^2}(\nabla'_r z')^2 + \mu_4 \frac{D^2}{L^4}(\nabla'_r{}^2 z')^2\}\Delta r, \qquad (A.10)$$

where the primes indicate nondimensional quantities. Recognizing that the Rossby number $R_0 = V/fL$ and that the Froude number $F = V/\sqrt{gd}$, and defining the nondimensional weights as follows

$$\alpha' = \alpha V^2, \qquad \gamma' = \gamma D^2, \qquad \beta' = \beta V^4/L^2,$$
$$\mu_1' = \mu_1 V^2/L^2, \quad \mu_2' = \mu_2 V^2/L^4, \quad \mu_3' = \mu_3 D^2/L^2, \text{ and}$$
$$\mu_4' = \mu_4 D^2/L^4,$$

we can write (A.10) as

$$J_2 = \sum_r \{\alpha'(c' - \tilde{v}')^2 + \gamma(z' - \tilde{z}')^2 + \beta'\left(\frac{c'^2}{r'} + \frac{c'}{R_0} - \frac{1}{F^2}\nabla'_r z'\right)^2$$
$$+ \mu_1'(\nabla'_r c')^2 + \mu_2'(\nabla'_r{}^2 c')^2 + \mu_3'(\nabla'_r z')^2$$
$$+ \mu_4'(\nabla'_r{}^2 z')^2\}\Delta r, \qquad (A.11)$$

where all terms are nondimensional. The prime notation can now be dropped for convenience.

A.5 Solutions of Equations (16) and (17)

The analysis equations derived from (A.11) result in a set of two nonlinear difference equations that must be solved simultaneously. The resulting equations are

$$\beta\left[-\frac{1}{F^2}\left(\frac{2c}{r}+\frac{1}{R_0}\right)\nabla_r z+\frac{2c^3}{r^2}+\frac{3c^2}{rR_0}+\frac{c}{R_0^2}\right]$$

$$+\mu_2\nabla_r{}^4 c-\mu_1\nabla_r{}^2 c+\alpha(c-\tilde{v})=0 \qquad \text{(A.12)}$$

and

$$\frac{\beta}{F^2}\left[-\frac{1}{F^2}\nabla_r{}^2 z+\frac{1}{R_0}\nabla_r c+\frac{1}{r}\nabla_r c^2-\frac{c^2}{r^2}\right]$$

$$+\mu_4\nabla_r{}^4 z-\mu_3\nabla_r{}^2 z+\alpha(z-\tilde{z})=0. \qquad \text{(A.13)}$$

These equations are solved by use of the sequential relaxation, or Liebmann method. The residual on the νth scan at the nth point for (A.12) is

$$R_n^{\nu}=-\frac{2\beta c_n^{\nu}}{2F^2 dr_n}\left(z_{n+1}^{\nu}-z_{n-1}^{\nu+1}\right)-\frac{\beta}{2dF^2R_0}\left(z_{n+1}^{\nu}-z_{n-1}^{\nu+1}\right)$$

$$+\frac{2\beta}{r_n{}^2}\left(c_n^{\nu}\right)^3+\frac{3\beta}{R_0 r_n}\left(c_n^{\nu}\right)^2+\frac{\beta}{R_0{}^2}c_n^{\nu}$$

$$+\mu_2\left[c_{n+2}^{\nu}+c_{n-2}^{\nu+1}+6c_n^{\nu}-4c_{n+1}^{\nu}-4c_{n-1}^{\nu+1}\right]/d^4$$

$$-\mu_1\left[c_{n+1}^{\nu}+c_{n-1}^{\nu+1}-2c_n^{\nu}\right]/d^2+\alpha\left[c_n^{\nu}-\tilde{v}_n\right]. \qquad \text{(A.14)}$$

The required condition for the $\nu+1$ iteration at the nth point is

$$0=-\frac{2\beta}{2F^2 d}\frac{c_n^{\nu+1}}{r_n}\left(z_{n+1}^{\nu}-z_{n-1}^{\nu+1}\right)-\frac{\beta}{2dF^2R_0}\left(z_{n+1}^{\nu}-z_{n-1}^{\nu+1}\right)$$

$$+\frac{2\beta}{r_n{}^2}\left(c_n^{\nu+1}\right)^3+\frac{3\beta}{R_0 r_n}\left(c_n^{\nu+1}\right)^2+\frac{\beta}{R_0{}^2}c_n^{\nu+1}$$

$$+ \mu_2 [c_{n+2}^{\nu} + c_{n-2}^{\nu+1} + 6c_n^{\nu+1} - 4c_{n+1}^{\nu} - 4c_{n-1}^{\nu+1}]d^4$$

$$- \mu_1 [c_{n+1}^{\nu} + c_{n-1}^{\nu+1} + 2c_n^{\nu+1}]/d^2 + \alpha[c_n^{\nu+1} - \tilde{v}_n], \quad (A.15)$$

where

$$c_n^{\nu+1} = c_n^{\nu} + \Delta c_n^{\nu}, \quad \text{or} \quad \Delta c_n^{\nu} = c_n^{\nu+1} - c_n^{\nu},$$

and

$$z_n^{\nu+1} = z_n^{\nu} + \Delta z_n^{\nu}, \quad \text{or} \quad \Delta z_n^{\nu} = z_n^{\nu+1} - z_n^{\nu}. \quad (A.16)$$

The terms Δc_n^{ν} and Δz_n^{ν} are the correction factors to be applied to c_n^{ν} and z_n^{ν}. The term Δc_n can be obtained by subtracting (A.14) from (A.15), i.e.,

$$-R_n^{\nu} = -\frac{\beta}{dF^2 r_n}(z_{n+1} - z_{n-1}^{\nu+1})(c_n^{\nu+1} - c_n^{\nu})$$

$$+ \frac{2\beta}{R_0^2}[(c_n^{\nu+1})^3 - (c_n^{\nu})^3] + \frac{3\beta}{R_0 r_n}[(c_n^{\nu+1})^2 - (c_n^{\nu})^2]$$

$$+ \frac{\beta}{R_0^2}(c_n^{\nu+1} - c_n^{\nu}) + 6\mu_2 L^4 (c_n^{\nu+1} - c_n^{\nu})/d^4$$

$$+ 2\mu_1 (c_n^{\nu+1} - c_n^{\nu})/d^2 + \alpha(c_n^{\nu+1} - \tilde{c}_n). \quad (A.17)$$

Making use of (A.16), we obtain

$$(c_n^{\nu+1})^2 = (c_n^{\nu} + \Delta c_n^{\nu})^2 = (c_n^{\nu})^2 + 2c_n^{\nu}\Delta c_n^{\nu} + (\Delta c_n^{\nu})^2$$

and

$$(c_n^{\nu+1})^3 = (c_n^{\nu} + \Delta c_n^{\nu})^3 = (c_n^{\nu})^3 + 3(c_n^{\nu})^2 \Delta c_n^{\nu}$$

$$+ 3c_n^{\nu}(\Delta c_n^{\nu})^2 + (\Delta c_n^{\nu})^3. \quad (A.18)$$

Substituting (A.16)and (A.18) into (A.17), we obtain

$$R_n^{\nu} = -\frac{\beta}{dF^2 r_n}(z_{n+1}^{\nu+1} - z_{n-1}^{\nu}) \Delta c_n^{\nu}$$

$$+\frac{2\beta}{r_n^2}\left[(c_n^\nu)^3+3(c_n^\nu)^2\Delta c_n^\nu+3c_n^\nu(\Delta c_n^\nu)^2+(\Delta c_n^\nu)^3-(c_n^\nu)^3\right]$$

$$+\frac{3\beta}{R_0 r_n}\left[(c_n^\nu)^2+2c_n^\nu\Delta c_n^\nu+(\Delta c_n^\nu)^2-(c_n^\nu)^2\right]$$

$$+\frac{\beta}{R_0^2}\Delta c_n^\nu+\frac{6\mu_2}{d^4}L^4\Delta c_n^\nu+\frac{2\mu_1}{d^2}\Delta c_n^\nu+\alpha\Delta c_n^\nu,$$

or

$$-R_n^\nu=\frac{2\beta}{r_n^2}(\Delta c_n^\nu)^3+\left[\frac{6\beta}{r_n^2}c_n^\nu+\frac{3\beta}{R_0 r_n}\right](\Delta c_n^\nu)^2$$

$$+\left[-\frac{\beta}{dF^2 r_n}(z_{n+1}^\nu-z_{n-1}^{\nu+1})+\frac{6\beta}{r_n^2}(c_n^\nu)^2+\frac{6\beta}{R_0 r_n}c_n^\nu\right.$$

$$\left.+\frac{\beta}{R_0^2}+\frac{6\mu_2}{d^4}+\frac{2\mu_1}{d^2}+\alpha\right]\Delta c_n^\nu. \qquad (A.19)$$

If we assume Δc_n is small, we can ignore the higher order of terms in Δc_n, and (A.19) becomes

$$\Delta c_n^\nu\approx -R_n^\nu/\left[-\frac{\beta}{dF^2 r_n}(z_{n+1}^\nu-z_{n-1}^{\nu+1})+\frac{6\beta}{r_n^2}(c_n^\nu)^2\right.$$

$$\left.+\frac{6\beta}{R_0 r_n}c_n^\nu+\frac{\beta}{R_0^2}+\frac{6\mu_2}{d^4}+\frac{2\mu_1}{d^2}+\alpha\right]. \qquad (A.20)$$

Following a similar process, the residual on the νth scan at the nth point for (A.13) is

$$R_n^\nu=\frac{\beta}{F^2}\left\{-\frac{1}{F^2}(z_{n+1}^\nu+z_{n-1}^{\nu+1}-2z_n^\nu)/d^2+\frac{1}{R_0}(c_{n+1}-c_{n-1}^{\nu+1})/2d\right.$$

$$+\frac{1}{r_n}\left[(c_{n+1}^\nu)^2-(c_{n-1}^{\nu+1})^2\right]/2d-\frac{1}{r_n^2}(c_n^\nu)^2\}$$

$$+\mu_4\left[z_{n+2}^\nu+z_{n-2}^\nu+6z_n^\nu-4z_{n+1}^\nu-4z_{n-1}^{\nu+1}\right]/d^4$$

$$-\mu_3\left[z_{n+1}^\nu+z_{n-1}^{\nu+1}-2z_n^\nu\right]/d^2+\gamma(z_n^\nu-\tilde{z}_n). \qquad (A.21)$$

The required condition for the $\nu+1$ iteration at the nth point is

$$0 = \frac{\beta}{F^2}\{-\frac{1}{F^2}(z_{n+1}^{\nu} + z_{n-1}^{\nu} - 2z_n^{\nu+1})/d^2$$

$$+ \frac{1}{R_0}(c_{n+1}^{\nu} - c_{n-1}^{\nu+1})/2d - \frac{1}{r_n^2}(c_n^{\nu+1})^2$$

$$+ \frac{1}{r_n}[(c_{n+1}^{\nu})^2 - (c_{n-1}^{\nu+1})^2]/2d\}$$

$$+ \mu_4 [z_{n+2}^{\nu+1} + z_{n-2}^{\nu+1} + 6z_n^{\nu+1} - 4z_{n+1}^{\nu} - 4z_{n-1}^{\nu}]/d^4$$

$$- \mu_3 [z_{n+1}^{\nu} + z_{n-1}^{\nu+1} - 2z_n^{\nu+1}]/d^2 + \gamma(z_n^{\nu+1} - \tilde{z}_n). \quad (A.22)$$

Subtracting (A.21) from (A.22), we obtain

$$-R_n^{\nu} = \frac{\beta}{F^2}\{\frac{2}{F^2 d^2}(z_n^{\nu+1} - z_n^{\nu}) - \frac{1}{r_n^2}[(c_n^{\nu+1})^2 - (c_n^{\nu})^2]\}$$

$$+ \frac{6\mu_4}{d^4}(z_n^{\nu+1} - z_n^{\nu}) + \frac{2\mu_3}{d^2}(z_n^{\nu+1} - z_n^{\nu}) + \gamma(z_n^{\nu+1} - \tilde{z}_n). \quad (A.23)$$

Substituting (A.16) and (A.18) into (A.23), we obtain

$$-R_n^{\nu} = \frac{\beta}{F^2}\{\frac{2}{F^2 d^2}\Delta z_n^{\nu} - \frac{1}{r_n^2}[(c_n^{\nu})^2 + 2c_n^{\nu}\Delta c_n^{\nu} + (\Delta c_n^{\nu})^2 - (c_n^{\nu})^2]\}$$

$$+ \frac{6\mu_4}{d^4}\Delta z_n^{\nu} + \frac{2\mu_3}{d^2}\Delta z_n^{\nu} + \gamma\Delta z_n^{\nu},$$

or

$$\Delta z_n^{\nu} = [-R_n^{\nu} - \frac{\beta}{F^2 r_n^2}(\Delta c_n^{\nu})^2 - \frac{2\beta}{F^2 r_n^2} c_n^{\nu}\Delta c_n^{\nu}]/$$

$$[\frac{2\beta}{F^4 d^2} + \frac{6\mu_4}{d^4} + \frac{2\mu_3}{d^2} + \gamma]. \quad (A.24)$$

Appropriate values are chosen for the weights α, β, γ, μ_1, μ_2, μ_3, and μ_4. An initial, or first guess, field is specified by obtaining values at each grid point by a simple extrapolation of the nearest observed values to point. This initial field, along with the observed values, is used in (A.14), (A.16), (A.20), (A.21), and (A.24) to obtain the analyzed field. Again, in actual practice, an overrelaxation factor is used, i.e., (A.16) becomes

$$c_n^{\nu+1} = c_n^{\nu} + 1.9\Delta c_n^{\nu} \quad \text{and} \quad z_n^{\nu+1} = z_n^{\nu} + 1.9\Delta z_n^{\nu}. \qquad (A.25)$$

An illustration of the rate of convergence to the solution for this set of equations and technique is shown in figure 7 for a typical set of data.